博士学位論文

氏名（本籍）	Anmar Hassan Shukor（イラク）
学位の種類	博士（工学）
学位記番号	甲　第176号
学位授与年月日	令和5年1月23日
学位授与の要件	学位規則第４条第１項
学位論文題目	Electrical and optical properties of copper oxides thin films on plastic substrates fabricated by helicon plasma sputtering

論文審査委員	主査	鷹野　一朗
	副査	尾沼　猛儀
	〃	於保　英作
	〃	馬場　則男
	〃	湯本　敦史
	〃	
	〃	

工学院大学大学院

Electrical and optical properties of copper oxides thin films on plastic substrates fabricated by helicon plasma sputtering

Department of Electrical Engineering and Electronics
Anmar Hassan Shukur

CONTENTS

CONTENTS

CONTENTS

CONTENTS

Chapter 1 Introduction

1.1 Copper oxide thin films

There are many types from copper oxide semiconductors, in this paper will study a copper (I) oxide and copper (II) oxide. Firstly, copper (I) oxide or cuprous oxide is the inorganic compound with the formula Cu_2O and polarity of p-type. It is one of the principal oxides of copper. The compound can appear either yellow or red, depending on the size of the particles. This red-colored solid is a component of some antifouling paints. Copper (I) oxide is found as the reddish mineral cuprite (1). Copper (I) oxide dissolves in concentrated ammonia solution to form the colorless complex $[Cu\ (NH_3)_2]^+$, which is easily oxidized in air to the blue $[Cu\ (NH_3)_4(H_2O)_2]^{2+}$. It dissolves in hydrochloric acid to give solutions of $CuCl_2^-$. Dilute sulfuric acid and nitric acid produce copper (II) sulfate and copper (II) nitrate, respectively (2). Copper (I) oxide may be produced by several methods (3). Most straightforwardly, it arises via the oxidation of copper metal:

$$4\ Cu + O_2 \rightarrow 2\ Cu_2O$$

Additives such as water and acids affect the rate of this process as well as the further oxidation to copper (II) oxides. It is also produced commercially by reduction of copper (II) solutions with sulfur dioxide. Aqueous cuprous chloride solutions react with base to give the same material. In all cases, the color is highly sensitive to the procedural details. In terms of their coordination spheres, copper centers are 2-coordinated and the oxides are tetrahedral (4). The structure thus resembles in some sense the main polymorphs of SiO_2, and both structures feature interpenetrated lattices. Copper (I) oxide crystallizes in a cubic structure with a lattice constant a_l = 4.2696 Å. The copper atoms arrange in fcc sub lattice, the oxygen atoms in a bcc sub lattice. One sub lattice is shifted by a quarter of the body diagonal (5). Copper (I) oxide is commonly used as a pigment, a fungicide, and an antifouling agent for marine paints. Rectifier diodes based on this material have been used industrially as early as 1924, long before silicon became the standard. Copper (I) oxide is also responsible for the pink color in a positive Benedict's test (6). Secondly, Copper (II) oxide or cupric oxide is the inorganic compound with the formula CuO. A black solid, it is one of the two stables oxides of copper, the other being Cu_2O. As a mineral, it is known as tenorite (7). It is a product of copper mining and the precursor to many other copper-containing products and chemical compounds. It is produced on a large scale by pyrometallurgy, as one stage in extracting copper from its ores (8). The ores are treated with an aqueous mixture of ammonium carbonate, ammonia, and oxygen to give copper (I) and copper (II) ammine complexes, which are extracted from the solids.

These complexes are decomposed with steam to give CuO (9). Copper (II) oxide belongs to the monoclinic crystal system. The copper atom is coordinated by 4 oxygen atoms in an approximately square planar configuration (10). The work function of bulk CuO is 5.3 eV (11) . As a significant product of copper mining, copper (II) oxide is the starting point for the production of other copper salts. For example, many wood preservatives are produced from copper oxide (12). Cupric oxide is used as a pigment in ceramics to produce blue, red, and green, and sometimes gray, pink, or black glazes. It is also incorrectly used as a dietary supplement in animal feed (13). Due to low bioactivity, negligible copper is absorbed (14). It is also used when welding with copper alloys (15). A copper oxide electrode formed part of the early battery type known as the Edison–Lalande cell. Copper oxide was also used in a lithium battery (16). In other hand, both the type of copper oxides has high electrical and optical properties, therefore it uses in the solar cells, light sensors and many others optical applications (17).

1.1.1 Application history of copper oxides

Copper oxides have long history in the materials that use in the electrical devices for the engineering fields, and also in the optical devices for the medical fields. In this study will mention some of them as shown below.

- In the 1920s, it was reported that copper oxide (Cu_2O) could be used as a rectifier diode, but it was soon replaced by selenium and silicon rectifier diodes.
- In the late 1970s, the research on the application of copper oxide (Cu_2O) to solar cells attracted attention, and the large-scale development was carried out in the United States, but stable solar cells with a photoelectric conversion efficiency of over 1 % could not be realized.
- In the 2017s, n-type ZnO-based transparent electrode/n-type Zn-Ge-O thin film/p-type Cu_2O sheet heterojunction solar cells were developed by Dr. Minami et al. in KIT and achieved a conversion efficiency of 8.23 %.
- In December 2021, Toshiba Corporation has announced that it has achieved the world 's highest power generation efficiency of 8.4 % by suppressing impurities in the power generation layer of transmissive copper oxide (Cu_2O) solar cells, which are expected to be used to realize low-cost, high-efficiency tandem solar cells.

Thus, the application of copper oxides in the field of electronics is still active, and the structure of the copper oxide itself greatly affects the properties of electronic devices using it.

In our research, we have also presented that Cu_2O (111) has a significant effect on the power generation efficiency of Cu_2O/TiO_2 thin-film solar cells.

https://www.global.toshiba/jp/technology/corporate/rdc/rd/topics/21/2112-03.html

Figure 1.1 Applications of copper oxide

1.1.2 Crystal structure

Copper oxides deliver interesting morphological architectures of plate-, needle-, and wire-shaped particles or nano cuboid, nanoplatelets, nanorods, and nanobelts with preferable crystal plane orientation (18). There are two essential steps of metal oxidation the oxygen adsorption and its reaction with metal atoms on the surface and a subsequent diffusion of oxygen into the bulk or the other way around, that of metal atoms to the surface. It is obvious from the similarity of Cu and Cu_2O crystal structures (see Figure 1.1) (19) that the oxidation of Cu to Cu_2O is facilitated by energetically favorable diffusion from one tetrahedral site to the other via the octahedral site without changing the structure topology. By contrast, CuO formation requires a more complex re-structuring, including the atomic displacement and symmetry lowering from cubic to monoclinic, and is thus associated with higher kinetic barriers. Nevertheless, in the initial stage of oxidation the surface oxidation is likely the kinetics determining process (20). The facet-dependent

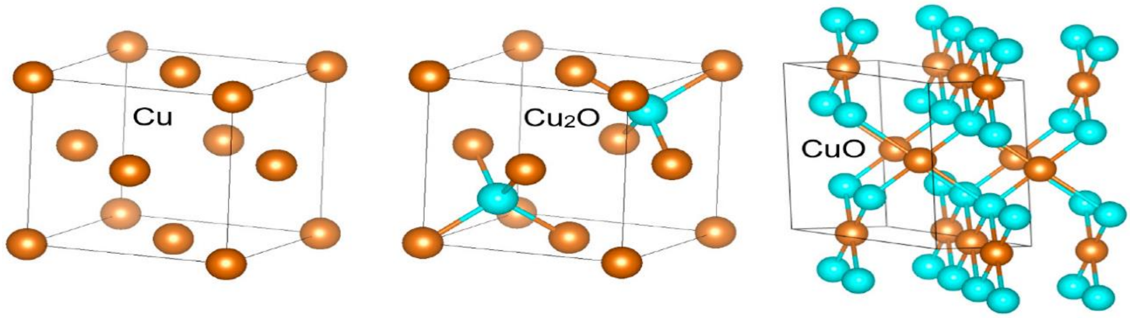

Figure 1.2 Comparation of Cu, Cu_2O and CuO crystal structure

properties of Cu_2O nanocrystals with cubic crystal structures and well-controlled polyhedral morphologies exposing (100), (111), and (110) surfaces. whenever, CuO structures with anisotropic crystal orientation showed morphological and geometric dependency on O_2 adsorption capabilities and their oxidation activity, i.e., as following in next orientations (200), (111), (011) and (001) (21).

1.1.3 Chemical properties (22)

Copper (I) oxide [1317-39-1], Mr 143.09, M_r 1235 °C, d_4^{25} 5,8 – 6,2, decomposes above 1800 °C. It occurs in nature as the red or reddish-brown mineral cuprite with a cubic or octahedral crystal morphology. Depending on the method of preparation and particle size, the synthetic material is yellow, orange, red, or purple. The yellow material has erroneously been referred to as Cu_2O hydroxide, but X-ray diffraction patterns indicate that there are no differences in the crystal structures of the colored forms. Their thermodynamic data are as follows: cp (298 K) 429.8 J kg^{-1} K^{-1} , cp (290 – 814 K) 519.2 J kg^{-1} K^{-1} , cp (290 – 1223 K) 565.2 J kg^{-1} K^{-1} , ΔH^o (25 °C) - 166.6 kJ/mol. Copper (II) oxide [1317-38-0], M_r 79.54, mp 1330 °C, d25 4 6:48, occurs in nature as the black mineral's tenorite (triclinic crystals) and paramelaconite (tetrahedral, cubic crystals). Commercially produced CuO is usually black, although a brown product (particle size < 10^{-6} m) can also be produced. Thermodynamic data: cp (298 K) 531.1 J kg^{-1} K^{-1}, cp (290 – 1253 K) 682.4 J kg^{-1} K^{-1} , ΔH^o (25 °C) -155.3 kJ/ mol. Copper (II) oxide is stable to air and moisture at room temperature. It is virtually insoluble in water or alcohols. Copper (II) oxide dissolves slowly in ammonia solution but quickly in ammonium carbonate solution; it is dissolved by alkali metal cyanides and by strong acid solutions. Hot formic acid and boiling acetic acid solutions readily dissolve the oxide. Copper (II) oxide is decomposed to copper (I) oxide and oxygen at 1030 C and atmospheric pressure; the reduction can proceed at lower temperature in a vacuum. Hydrogen and carbon monoxide reduce CuO to the metal at 250 °C and to copper (I) oxide at about 150 °C. Ammonia gas reduces CuO to copper metal and Cu_2O at 425 – 700 °C.

1.1.4 Semiconductor characteristics (23-27)

Copper oxides are a perfect insulator at room temperature, but when appropriate energy is applied from the outside such as heating or UV irradiation, it acts as an p-type Cu_2O and n-type CuO semiconductor. In addition, as shown in the energy diagram in fig. 1.2 (28), the polarity position of the conduction band, the higher the reducing power of electrons, and the higher the position of the valence band, the higher the oxidizing power of holes. Furthermore, copper oxides are semiconductors that have been studied for several reasons such as the natural abundance of starting material copper (Cu); the easiness of production by Cu oxidation; their non-toxic nature and the reasonably good electrical and optical properties by Cu_2O. Copper forms two well-known oxides: tenorite (CuO) and cuprite (Cu_2O). In general, both the tenorite and cuprite are p-type semiconductors, but depend of the fabrication methods there are two polarities of copper oxide, one is p-type of Cu_2O with band gap energy of 2.1 to 2.6 eV and the second is n-type CuO with band gap of 1.3 to 1.9 eV. CuO is attractive as a selective solar absorber since it has high solar absorbency and a low resistivity. Cu_2O is very promising candidate for solar cell applications as it is a suitable material for photovoltaic energy conversion.

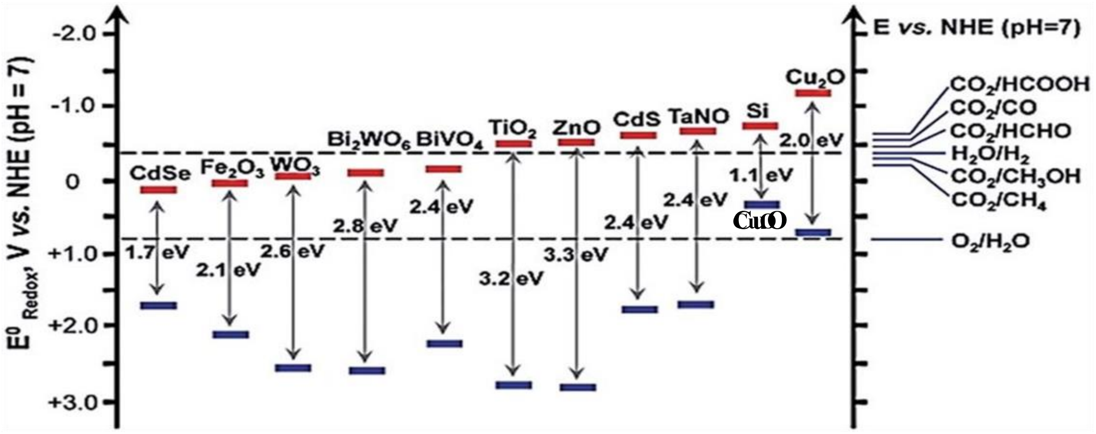

Figure 1.3 Typical semiconductor energy diagram

1.1 Thin Film (29, 30)

A thin film is a layer of material ranging from fractions of a nanometer (monolayer) to several micrometers in thickness. The controlled synthesis of materials as thin films (a process referred to as deposition) is a fundamental step in many applications. A familiar example is the household mirror, which typically has a thin metal coating on the back of a sheet of glass to form a reflective interface. The process of silvering was once commonly used to produce mirrors, while more recently the metal layer is deposited using techniques such as sputtering. Advances in thin film deposition techniques during the 20th century have enabled a wide range of technological breakthroughs in areas such as magnetic recording media, electronic semiconductor devices, integrated passive devices, LEDs, optical coatings (such as antireflective coatings), hard coatings on cutting tools, and for both energy generation (e.g. thin-film solar cells) and storage (thin-film batteries). It is also being applied to pharmaceuticals, via thin-film drug delivery. A stack of thin films is called a multilayer.

In addition to their applied interest, thin films play an important role in the development and study of materials with new and unique properties. Examples include multiferroic materials, and superlattices that allow the study of quantum phenomena.

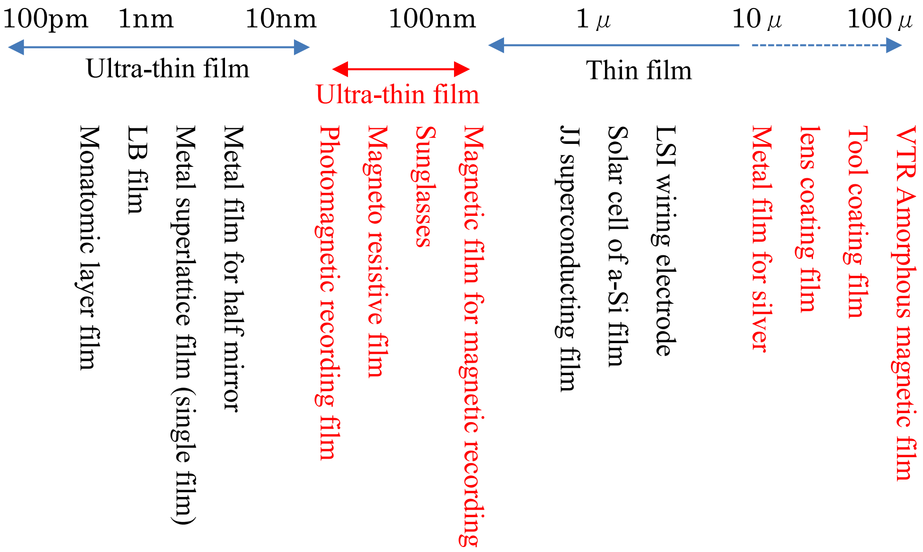

Figure 1.4 Thin film dimensions and application fields

1.2.1 Thin film formation method and general thin film features (31)

Thin film fabrication methods include vacuum vapor deposition, sputtering, chemical vapor deposition, liquid layer fabrication, plating, and coating, and there are methods based on these methods with various ingenuity. In vacuum deposition, all the formed atoms are in the vapor phase state, but in sputtering, they are ionized, albeit in a small amount. In the chemical vapor deposition method, the ionization rate is high, and in plating, all the condensed atoms are ionized in the solution. In addition, there are various substrates such as glass, ceramics, semiconductors, metals, and plastics. Glass is most often used in experiments, but most advanced devices are semiconductors and ceramic substrates. The structural characteristics of thin films often derive from the fabrication of thin films. Ordinary thin films are in a polycrystalline state (epitaxial grown ones are single crystals), and the size of crystal grains ranges from several nm to several μm, which is extremely small compared to bulk. In addition, crystal growth is mainly controlled by nucleation and atom diffusion on the substrate surface, but the condensation temperature (substrate temperature) is low, so the crystal grain size is small and the crystal shape is perpendicular to the substrate surface as described above. It tends to become elongated columnar crystals in any direction. Atomic diffusion is insufficient, and many crystal lattice defects are introduced during thin film formation. In addition, since it is a two-dimensional substance, the influence on the surface becomes remarkable, and since it is firmly bonded to the substrate, there is also an influence due to the elasticity of the substrate. Electrically, conduction electrons are often scattered due to grain boundaries and lattice defects, and the electrical resistance is generally higher than that of bulk. In addition, when the thin film is less than the mean free path of conduction electrons, the scattering on the surface becomes remarkable and the electric resistance becomes high, which causes a size effect, but the eddy current loss becomes low.

In terms of optical properties, the reflectance changes significantly depending on the surface condition of the thin film. A thin film with good surface smoothness has higher reflectance than the bulk polished surface. One of the optical features of metal and semiconductor thin films with a small bandgap is that light is transmitted when they are made into thin films. In the case of metal, visible light is transmitted considerably below 50 nm. In addition, since there are many lattice defects, the density is lower than that of bulk and the refractive index is also lower. The interference of light becomes stronger, and coloring due to the interference color is also seen.

In terms of thermal properties, a decrease in thermal conductivity is generally observed. This is because the scattering of electrons increases in heat conduction by electrons such as metal. However, the dissipation of Joule heat when energizing a metal or semiconductor thin film is higher than that of bulk because of the large heat conduction effect on the substrate. Therefore, a current about two orders of magnitude higher than that of the bulk can be passed. In terms of mechanical properties, the internal stress is high due to the high lattice defect density of the thin film and the small crystal grains, and the tensile strength and strength are higher than those of the bulk. In addition, since there is a difference in thermal expansion coefficient from the substrate, stress is also applied to this. If the adhesion to the substrate is low, it often peels off.

In terms of chemical properties, corrosion resistance may decrease due to many lattice defects, small crystal grains, and deviation from stoichiometry when it is a compound.

However, since there are no grain boundaries in the amorphous state, diffusion is suppressed and corrosion resistance is improved. In addition, since the electronic state of the surface is different from that of bulk, the catalytic action changes. In terms of magnetic properties, it is said that spontaneous magnetization does not change in thickness up to several nm. There is also the idea that when it becomes thinner, the spontaneous magnetization increases due to the effect of the surface. What is remarkable is magnetic anisotropy, and since the thin film is secondary, it tends to be magnetized parallel to the film surface. However, it is often used as a perpendicularly magnetized film because it is magnetized perpendicular to the film surface due to the stress from the substrate and the shape of the crystal grains (columnar crystals).

1.2.1.1 Drive process (32)

CVD (Chemical Vapor Deposition) and PVD (Physical Vapor Deposition) are one of the dry processes. The first is called the chemical vapor deposition method, and the second is called the physical vapor deposition method or the physical vapor deposition method. CVD mainly uses as a chemical method in which a compound / elemental gas consisting of one or more types containing the elements that make up a thin film is supplied onto the substrate, and the thin film is formed by a gas or a chemical reaction on the surface of the substrate. In recent years, CVD have used in the plasma and reactive ion plating that utilize the characteristics of both PVD and CVD. On the other hand, PVD forms a thin film using physical methods such as vacuum deposition of materials, sputtering using plasma and ion plating. There are various methods for CVD depending on the method of supplying activation energy in the reaction and the reaction type of gas. Normal pressure in a CVD is basic and highly versatile, but there are problems with the substrate due to uniformity and high temperature. In the field of LSI, it is changing to reduced pressure CVD, which has excellent uniformity and mass productivity. Another disadvantage of CVD is that it requires a high temperature for the reaction, which narrows the selection range of substrate materials in terms of distortion etc. Therefore, in order to reduce the temperature at CVD, new ones such as plasma CVD that enables generation at low temperature using electrical energy (discharge), optical CVD using photoexcitation, and laser CVD have been developed. However, the advantages of conventional thermal CVD are great, and it is still the mainstream. Considering the classification of gas reaction types, typical reaction types are substrate reaction method, thermal decomposition method, hydrogen reduction method, chemical transport method (disproportionation reaction method), reaction deposition method, etc.

The features of CVD can be summarized as follows: 1) Multi-layer filling is possible 2)

Equipment, raw materials, running costs are low and relatively easy 3) Adhesion and crystallinity are good 4) Diversity is large.

In general, PVD includes vacuum deposition, sputtering, and ion plating as three basic film formation methods. Based on these three basic methods, various methods are used to obtain film formation conditions that meet the purpose by improving and replenishing the features of each. At the same time, not only physical vapor deposition but also other things of this metal component, especially reactive PVD process in which a specific gas (reactive gas or metal gas) is introduced and reacted to deposit an alloy or compound as a reaction product, etc. Various processes have been developed and are called reactive vacuum deposition, reactive sputtering, reactive ion plating, etc. The two basic methods other than the vacuum deposition method actively utilize plasma. That is, ions and active particles are used to appropriately utilize this function for adhesion and the like, especially effective in reactive PVD processes. The basic process of PVD is thin film deposition and condensation, and the process of this technology has been devised. For example, sputtering, ionization (plasma), bias voltage application etc, to perform for the purpose of affecting the film properties. The main features of PVD are 1) it is possible to obtain a thin film with good adhesion at low temperatures 2) it is possible to determine a wide variety of substrate properties and thin film properties 3) it is possible to form thin films of alloys, compounds and complex compounds 4) easy consideration for the environment associated with exhaust gas.

Table 1.1 shows a comparison between CVD and PVD.

Table 1.1 Comparison between CVD and PVD

	CVD	PVD
Materials	Vapor of a compound consisting of product constituent elements	Vapor of target product and vapor of constituents
Activation methods	The main method is temperature rising, in addition to this, high density of energy such as plasma, light and laser is used for reduce the temperature.	Evaporation heat and evaporation energy are mainly used, and plasma, bias voltage, ionization energy, etc. are additionally used.
Substrate temperature	150~2000℃	25~500℃
Thin film formation	1~1500μm/h	0.5~250μm/h

rate		
Efficiency for forming good quality films	Low	Low
The Component of the thin film	Crystalline, amorphous (equilibrium)	Amorphous, crystalline (non-equilibrium)
Materials that can be formed	Metals, carbonaceous diamonds, carbides, nitrides, silicides, borides, oxides, sulfides, seleniums, tellurics, intermetallic compounds, alloys, etc.	In addition to the materials of CVD , the diamond-like carbon, superlattice, etc are use.

1.2.1.2 Vacuum deposition method and sputtering method (33)

Figure 1.4(a) shows the characteristics of the vacuum deposition method and sputtering. Figure 1.4(b) schematically shows both technologies. Generally, the source of particles that produce a thin film is called a source, and the plate which the thin film grows on it is called a substrate. As shown in figure 1.4(a), in the sputtering method the ions in the plasma are accelerated within the cathode drop, impacting on the target and causing sputtering. That is, the source is this planar target. The cathode drop is usually around 400V, and ions with energy close to this value are ejected from the target, and the sputtering atoms also have a value of about several eV. These atoms adhere to the substrate to form a thin film, which grows under the influence of ions and high-energy neutral gas molecules as shown in the figure 1.4(33).

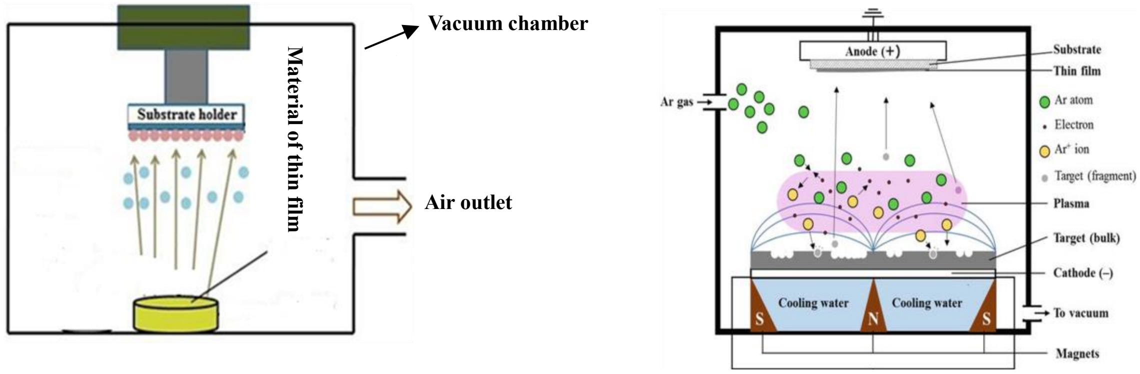

a-Vacuum deposition method **b-Sputtering method**

Figure 1.5 Principle diagram of sputtering and vacuum deposition

On the other hand, in vacuum vapor deposition, it is generally evaporated by electron beam heating. Therefore, as shown in figure 1.4(b), the source corresponds to the diameter of the focused electron beam and is point-shaped. Evaporated atoms have thermal energy only and are about 0.2 eV, depending on the type. In different word, when 1 volt is converted to temperature, it becomes 11600K. In the case of vacuum deposition, the effect of high-energy particles during film growth is not received. From the main reasons to use sputtering in this study, are as follows.

1) By appropriately controlling the amount and energy of high-energy particles that irradiate the substrate during film formation, the film quality can be improved as follows.

a- Thick and high-density thin film
b- Thin film with a crystal structure that is not in the bulk
c- Thin film with high adhesion on the substrate

2) In the production of compound thin films, it is difficult to make a constant ratio due to the difference in vapor pressure and in vapor deposition, but in sputtering, thin films with almost the same composition can be obtained by using a target with the desired composition.
3) The growth rate of the film is stable in proportion to the sputter power. Therefore, a thin film with high accuracy can be obtained only by controlling the time.
4) Since sputtering is performed in a planar manner, a uniform film can be easily obtained.
5) A compound thin film such as an oxide or a nitride can be obtained by reactive sputtering using a metal or a semiconductor target by adding an active gas such as oxygen or nitrogen to argon or the like.

6) The target has a relatively long life and is suitable for continuous operation.
7) Film formation speed increases when magnetron sputtering is used.
8) Dielectric thin films can be easily produced by RF sputtering using high frequencies.

References

1) N. N. Greenwood, A. Earnshaw. *Chemistry of the Elements, 2nd ed, Butterworth-Heinemann, Oxford, UK*, **(1997)**.
2) D. Nicholls. *Complexes and First-Row Transition Elements, Macmillan Press, London,* **(1973)**.
3) H. Wayne Richardson. *"Copper Compounds in Ullmann's Encyclopedia of Industrial Chemistry* **(2002)**, Wiley-VCH, Weinheim.
4) J. Brandt, D. Fröhlich, C. Sandfort, M. Bayer, H. Stolz, and N. Naka. *Phys. Rev. Lett*, 99**(2007)**, p. 217403.
5) G. Papadimitropoulos, N. Vourdas, V. Em. Vamvakas, and D. Davazoglou. *Thin Solid Films,* 515 **(2006)**, p. 2428.
6) B. K. Meyer, A. Polity, D. Reppin, M. Becker, P. Hering, P. J. Klar, Th Sander, C. Reindl, J. Benz, M. Eickhoff, C. Heiliger, M. Heinemann, J. Bläsing, A. Krost, S. Shokovets, C. Müller, and C. Ronning. *Phys. Status Solidi B*, 249 **(2012)**, p. 1487.
7) F. Lim, Choi, J. J., and Hanrath, T. *Journal of Nanomaterials*,87 **(2012)**, pp. 1 - 6.
8) R. Ranjbar-Karimi, Bazmandegan-Shamili, A., Aslani, A., and Kaviani, K. *Physica B: Condensed Matter*,405 **(2010)**. 15, pp. 3096 - 3100.
9) Chauhan, Satsangi, V. R., Dass, S, and Shrivastav, R. *Bulletin of Materials Science*, 29 **(2006)**, p. 709.
10) K. Hyun Yoon, Choi, W. Jin, and Kang, D. Heon. *Thin Solid Films*, 372 **(2000)**, pp. 250 - 256.
11) Paracchino, A., Laporte, V., Sivula, K., Grätzel. *M. & Thimsen*, 10 **(2011)**, pp.456–461.
12) Ogwu, A. A., Darma, T. T. and Bourquerel, E. *Journal of achievements in materials and manufacturing engineering,* 24 **(2007)** (1), p.172.
13) Gupta, N., Alapatt, G. F., Podila, R., Singh, R. and Poole, K.F. *International Journal of Photoenergy*, 10**(2009)**, p.1155.
14) A. Chen, G. Yang, H. Long, F. Li, Y. Li, and P. Lu. *Thin Solid Films,* 517 **(2009)**, p.4277.
15) S. B. Wanga, C. H. Hsiaoa, S. J. Changa, K. T. Lamb, K. H. Wenb, S. C. Hungc, S. J. Youngd, and B. R. Huange. *Sens. Actuators, A*, 171 **(2011)**, p.207.
16) S. Nandy, A. N. Banerjee, E. Fortunato, and R. Martins. *Rev. Adv. Sci. Eng*, 2 **(2013)**,

p.1.

17) Kumar, V., Masudy-Panah, S., Tan, C. C., Wong, T. K. S., Chi, D. Z., & Dalapati, G. K. *IEEE 5th International Nanoelectronics (INEC)*, 22 **(2013)**, pp.443-445.

18) Y. Chang, J. J. Teo, and H. C. Zeng. *Langmuir,* 21**(2005)**, p.1074.

19) Jindˇrich Leitner, David Sedmidubský, Michal Lojka and Ondˇrej Jankovský. *Materials,* 13 **(2020)**, p. 2878.

20) Ndolomingo, M.J.; Bingwa, N.; Meijboom, R. Review of supported metal nanoparticles: Synthesis methodologies, advantages and application as catalysts. *J. Mater. Sci*,55 **(2020)**, pp.6195–6241.

21) M. J. Siegfried and K.-S. Choi. *J. Am. Chem. Soc.* 128 **(2006)**, p. 10356.

22) Calumet and Hecla. *US (H. Day),* 3 **(1969)**, pp.466 143.

23) G. Papadimitropoulos, N. Vourdas, V. Vamvakas Em and D. Davazoglou. *Thin Solid Films*, 515 **(2006),** pp.2428–2432.

24) Anmar H. Shukor, Haider A. Alhattab, and Ichiro Takano. *Journal of Vacuum Science & Technology, B* 38 **(2020)**, p. 012803.

25) A.N. Banerjee and K. Chattopadhyay. *Progress in Crystal Growth and Characterization of Material*, 50 **(2005)**, pp. 52-105.

26) T. J. Richardson and M.D. Rubin, *Electrochim. Acta*, 46 **(2001)**, p. 2381.

27) N. D. Hoa, S. Y. An, N. Q. Dung, N. V. Quy and D. Kim D. *Sensors and Actuators B: Chemical*, 146 **(2010)**, pp.239-244.

28) Yang Yang, Saira Ajmal, Xiuzhen Zheng, Liwu Zhang. *Sustainable Energy & Fuelsm,* 1 **(2017)**, p. 8.

29) Microfluidic Cell Culture Systems (Second Edition), **(2019)**.

30) M. C. RAO, M. S. SHEKHAWAT. *World Scientific,*22 **(2013)**, pp.576–582.

31) J. L. Vossen, W. Kern, eds., *Thin Film Processes*, *Academic, New York* **(1978)**.

32) Handbook of Physical Vapor Deposition (PVD) Processing (Second Edition), **(2010)**.

33) Andresa Baptista, Francisco Silva, Jacobo Porteiro, José Míguez and Gustavo Pinto. *Coatings,* 8 **(2018)**, p. 402.

Chapter 2 Film deposition equipment

2.1 Multi-process coating devise

2.1.1 Summary

In this study, film formation was performed using a multi-process coating device (ULVAC, Inc.). Generally, the sputtering process pressure is about 1.3 Pa, but the multi-process coating device has an inductively coupled RF plasma-assisted magnetron sputtering source that can maintain the discharge to a low pressure of 7×10^{-2} Pa. In the past, it was important to use a substrate as an electrode in order to maintain stable discharge in a parallel plate type device, but in an inductively coupled RF plasma-assisted magnetron sputtering device, the substrate is electrically independent, so the cathode alone and it is possible to maintain the discharge. Therefore, it is possible to adopt a structure like MBE in which each cathode aims at the center of the substrate by separating the distance between the substrate and the target (long slow sputtering). Figure 2.1 shows a schematic diagram of this device.

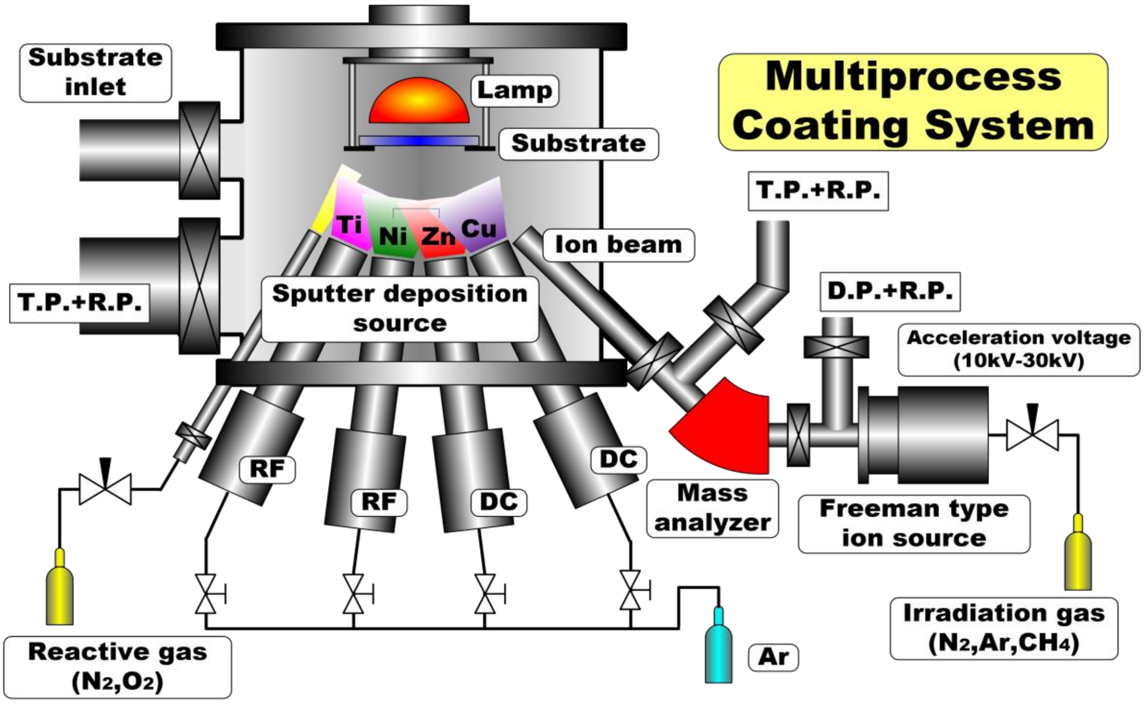

Figure 2.1 Conceptual diagram of multi-process coating equipment

This device is divided into a preparation room, an intermediate room, and a film formation room, each of which has an independent exhaust system. In the experiment, the sample substrate is introduced into the preparation chamber, transferred to the intermediate chamber, reverse sputtered for substrate cleaning, and the substrate is transferred to the film formation chamber again. In the film formation chamber, film formation can be performed by sputtering the target with Ar^+ ions. Ion implantation can introduce irradiation gas into the ion source and φ20 mm ion irradiation on the sample. Therefore, the greatest feature of this device is that it can perform processing that combines film formation by the sputtering method and ion beam irradiation. Hereinafter, each part of this device will be described (1,2).

2.1.2 Preparing room

The sample substrate is introduced from the preparation room as shown in fig 2.2. Five sample substrates (<φ100 mm) can be installed in the main room. Exhaust is performed by a rotary pump and a turbo molecular pump and exhausts up to around 1×10^{-5} Pa. Section 2.1.5 shows the outline and exhaust mechanism of the rotary pump and turbo molecular pump that exhaust the sample introduction chamber.

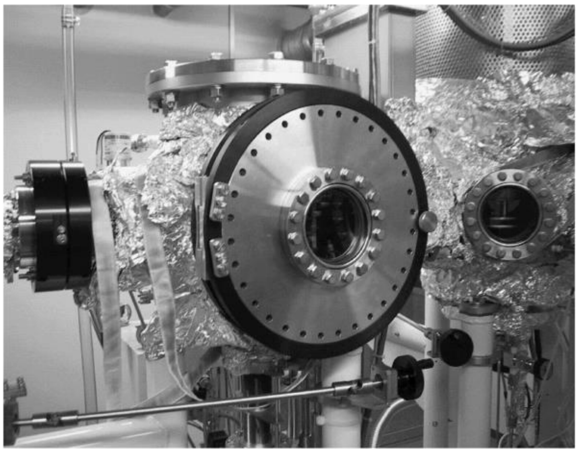

Figure 2.2 Exterior view of multi-process coating equipment preparation

2.1.3 Plasma room

Move the sample substrate to the holder in the intermediate chamber as shown in fig 2.3 and reverse sputter with Ar + plasma. Reverse sputtering is a process in which Ar + ions collide with the sample surface to perform sputter cleaning of the surface. The main room is also exhausted by a rotary pump and turbo molecular pump, and is exhausted to around 1 x 10^{-5} Pa.

2.1.4 Film formation room

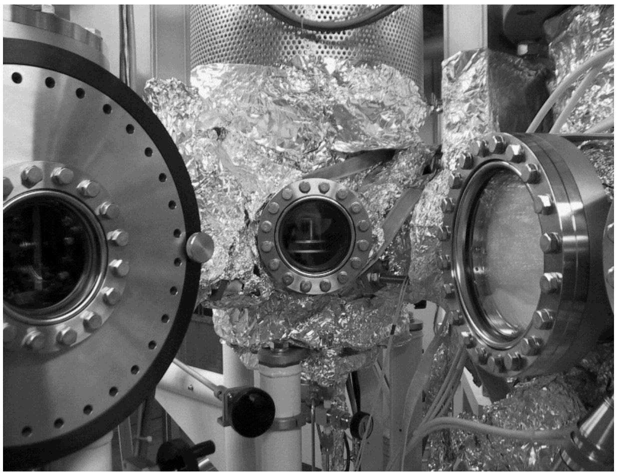

Figure 2.3 Exterior of multi-process coating equipment intermediate room

Figure 2.4 shows the fabrication room, to perform film formation the sample substrate is moved to the sample holder in the film formation chamber. As shown in table 2.1, the main room has three sputtering sources and can deposit Cu, Zn, Ni and Ti. Of course, this is not the case if the target metal is replaced. An inductively coupled RF plasma-assisted magnetron sputtering device is used as the sputtering source of this device, and it is possible to maintain plasma discharge up to 7 × 10^{-2} Pa after introducing Ar. For Cu, Zn and Ni sputtering, the DC method is used, and for Ti the RF method is used for film formation. The inductively coupled RF plasma-assisted magnetron sputtering device used in this study is called helicon sputtering, and unlike the counter electrode type sputtering device, the plasma does not come into contact with the substrate, so it is easy to control the substrate temperature.

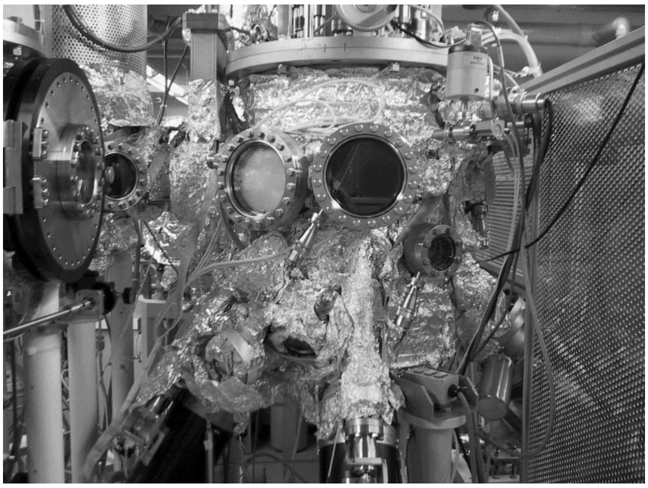

Figure 2.4 Multi-process coating device film formation room

Table 2.1 Specifications of each sputter source

Target	Type	Power
Cu	DC magnetron sputter	500W
	(Inductively coupled RF plasma assisted magnetron sputtering equipment)	
Zn	DC magnetron sputter	500W
	(Inductively coupled RF plasma assisted magnetron sputtering equipment)	
Ni	RF Magnetron Sputter	200W
	(Inductively coupled RF plasma assisted magnetron sputtering equipment)	
Ti	RF Magnetron Sputter	200W
	(Inductively coupled RF plasma assisted magnetron sputtering equipment)	

2.1.4.1 Sputtering technique (3,4)

Among the thin film forming methods, the sputtering method using non-thermal equilibrium evaporation is currently the most widely used and industrially used method. The sputtering method as a thin film fabrication method puts its elementary process in the so-called sputtering phenomenon. In other words, the collision of high kinetic energy particles with a solid target causes the transfer of kinetic energy between the two, and sputtering means that the constituent atoms of the target obtain kinetic energy that exceeds the binding energy of the atoms and then jump out of the target. In the sputtering film formation method, the target constituent atoms protruding in this way are deposited on the substrate to form a thin film. The discovery of the sputtering phenomenon is very old as shown in fig 2.5 (5), but it was Sigmund who theoretically explained the mechanism. Today, the sputtering phenomenon is that "high kinetic energy particles (ions or atoms neutralized by electrons near the target surface) incident on the target surface give their momentum to the target constituent atoms by elastic collision, and then this primary rebound atom repeats collisions with neighboring atoms one after another (collision cascade), resulting in the release of the target surface.

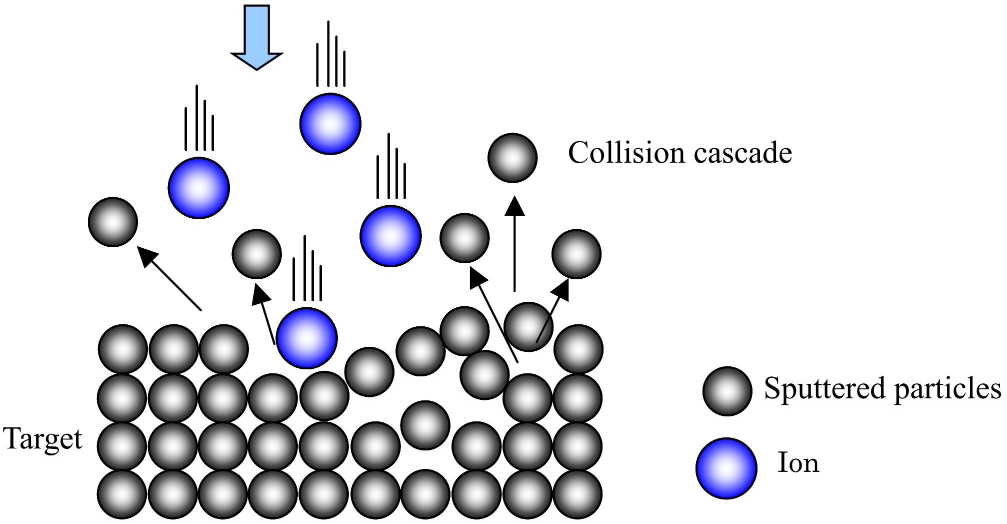

Figure 2.5 Sputtering conceptual diagram

2.1.4.2 Magnetron sputtering method (6,7)

Magnetron sputtering was used in this study to prepare copper oxides (Cu_2O, CuO). Magnetron sputtering places a permanent magnet under the target and superimposes a magnetic field perpendicular to the electric field between both electrodes. With this method, low pressure, low applied voltage and large ion current density can be obtained, so not only the deposition rate of the thin film be increased, but also electrons are constrained near the target, so the effect of plasma on the substrate can be reduced. On the other hand, although there is disadvantage such as partial erosion of the target due to the non-uniform magnetic field, ionization of sputtered atoms, and difficulty in discharging with a magnetic target, it has been improved and is now the mainstream. In cold cathode glow discharge, secondary electrons emitted from the cathode due to ionic impact are accelerated by the electric field of the cathode drop and perform linear motion, and the discharge is maintained by ionizing collision with gas molecules. usually, 2-pole DC sputtering device using to prepare a film in a pressure range of about 2 to 10 Pa. This is because the discharge is not maintained below 2 Pa, but when there is a magnetic field perpendicular to the electric field in the cathode drop region, the electrons drift while drawing a cycloid curve in the direction perpendicular to the electric field and magnetic field, so they are ionized. The frequency of collisions increases and discharge can be maintained even at relatively low applied voltages. The name of the magnetron electrode is derived from its structure similar to that of an ultra-high frequency magnetron. However, the magnetron electrode in a broad sense is not bound by the external shape, and the electrons drift in the direction of E × B in the orthogonal electromagnetic field space near the cathode surface, and one of the drift motions is an unterminated closed trajectory, it is characterized in that the discharge is maintained by forming. Figure 2.6 (8) shows the configuration of a classical coaxial cylindrical magnetron electrode and various magnetron electrodes that can be regarded as variants thereof (3). (a), (b) and (g) use a uniform magnetic field parallel to the axial direction, and the electrons do not receive the convergence force in the axial direction, so they escape from both ends of the cathode. On the other hand, in other electrode structures curved magnetic field lines are used, and in a space where the electromagnetic fields are not orthogonal, a force that pushes rotating electrons back to the orthogonal electromagnetic field space side works. Therefore, the electrons are converged extremely efficiently, the frequency of ionization collisions becomes extremely high and a very large target impact ion current density can be easily obtained. Sputtering equipment using these electrodes is often called a high-speed magnetron electrode because a large film formation rate can be obtained.

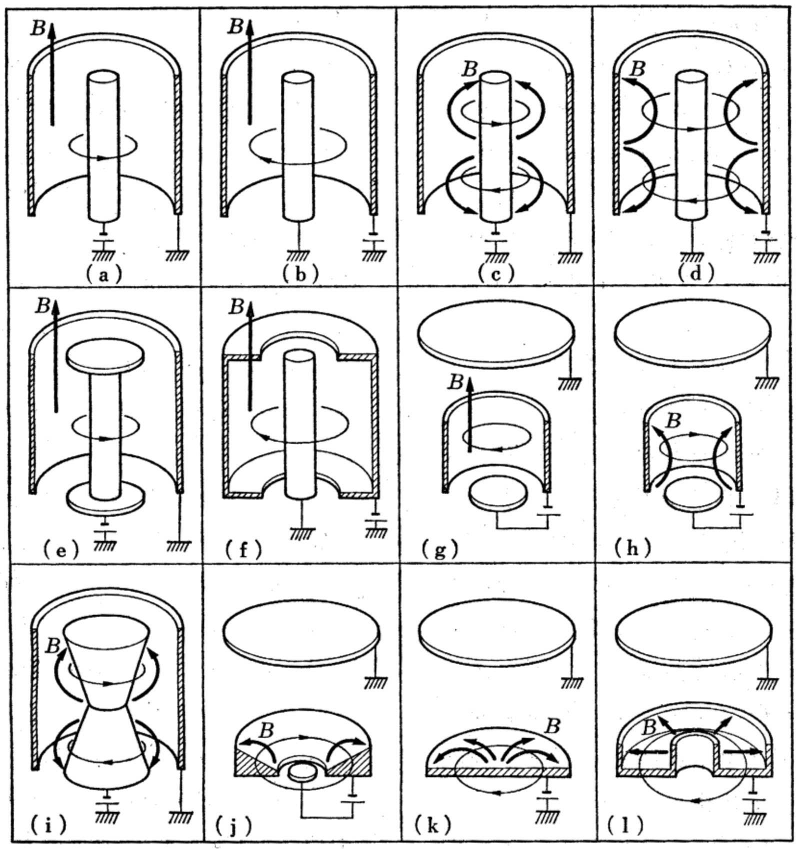

Configuration of various magnetron electrodes. The thick arrow B indicates to the line of magnetic force, and the thin arrow indicates the trajectory of the electron and the direction of motion. (a) Classic coaxial cylindrical magnetron, (b) Classic coaxial cylindrical reverse magnetron, (c) High-speed coaxial magnetron (built-in magnet), (d) High-speed coaxial reverse magnetron (built-in magnet), (e) High-speed coaxial magnetron (both ends cathode plate type), (f) High-speed coaxial magnetron (both ends cathode plate type), (g) Hollow circular cathode (h) High-speed hollow circular cathode (i) High-speed type pan magnetron (j) High-speed inverted magnetron (k) High-speed flat plate magnetron (built-in magnet) (l) High-speed flat plate magnetron (both ends cathode plate type)

Figure 2.6 Configuration of various magnetron electrodes

2.1.4.3 Bipolar sputtering technique and RF sputtering technique (9)

Figure 2.7 shows a schematic diagram and potential distribution of DC bipolar discharge. In the gas pressure range (several hundred mTorr or more) where normal glow discharge plasma is formed, highly conductive sunlight column plasma extends from the anode to the vicinity of the cathode, and most of the applied voltage is the cathode drop part in front of the cathode (target), it depends on the ion sheath part called (Cathode Fall). Ions in the plasma are accelerated by this cathode descent part, that is lead to gain energy and enter the target surface perpendicularly, which is the cathode, causing the emission of γ electrons and the emission of sputtered particles. However, in DC bipolar discharge the ionization efficiency is low so the current density cannot be high and high gas pressure operation occurs. Due to the high gas pressure, the mean free path of the sputtered particles is also shortened so the energy of the sputtered particles is also reduced in many collision processes. In addition, since the self-shadowing effect is also remarkable, the obtained film tends to be a low-density film, so it is not often used.

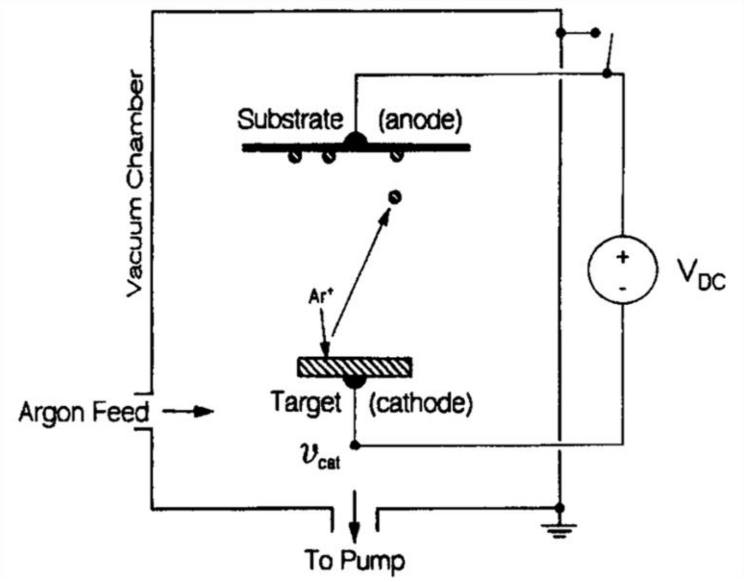

Figure 2.7 DC bipolar sputtering equipment

On the other hand, as shown in fig 2.8, the RF sputtering method can be realized by using a radio frequency (RF) power supply for bipolar discharge. However, if the target is conductive so that a negative potential self-bias is induced on the target surface, insert a blocking capacitor in the matching circuit to insulate it in a direct current manner. Since the discharge is maintained even in the state of being insulated by direct current, the RF sputtering method has a great feature that the insulator material can also be sputtered. In the RF sputtering method, the area of the target corresponding to the cathode is usually extremely smaller than the area of the anode (anode: usually corresponding to the inner wall surface of the chamber). In this method, due to the large difference in mobility of ions and electrons in the plasma due to the high-frequency electric field, the potential in the steady state on the target surface become larger than the bias on the anode surface and biased to the negative side (Vc) as shown in fig 2.9.

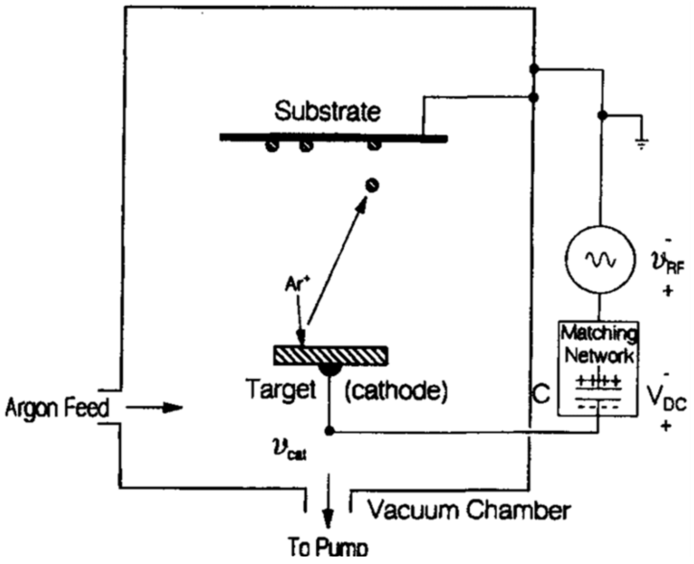

Figure 2.8 RF bipolar sputtering device and potential distribution

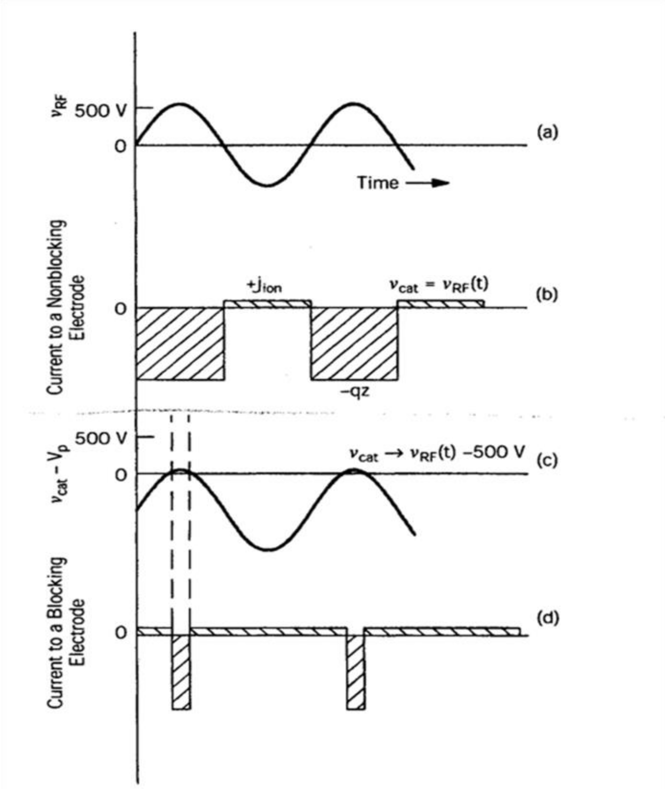

Figure 2.9 Principle of cathode self-bias of RF sputtering equipment

This state is called self-bias. This bias voltage is used to cause atoms to collide with the target and cause a sputtering phenomenon. This bias voltage is used to make the ions to collide with the target and cause a sputtering phenomenon. The anode surface is also relatively negatively biased when viewed from the plasma potential, but the bias voltage Va is low, and the ratio of Vc to Va (Vc / Va) is 4 of the area ratios of cathode to anode (Sa / Sc) and estimated to be proportional to the power or cube. In any case, if the area ratio (Sa / Sc) of the electrodes is increased, a large negative bias is applied to the target, and the sputtering process is efficiently performed. The frequency in the industrially assign, is often used 13.56MHz. The average negative potential of the target is about the peak value of the applied high frequency voltage. It is important to configure the matching circuit so that the high frequency power from the power supply is efficiently transmitted to the discharge plasma. In addition, since high voltage is also applied, it is necessary to use parts with high resist voltage, including water cooling piping and cooling water. In RF discharge, the electrons in the discharge space reciprocate so the impact ionization probability due to the electrons increases and the discharge can be maintained even at a low gas pressure of several mTorr. Therefore, it is possible to fabricate a film without losing the energy of sputtered particles and it is widely used mainly for insulator films. It is also widely used as RF magnetron sputtering combined with magnetron discharge. As shown in fig 2.10, one of the major factors behind the dramatic increase in demand for thin films made by the sputtering method is that the reactive sputtering method has made it easier to make thin films of compounds (mostly insulators).

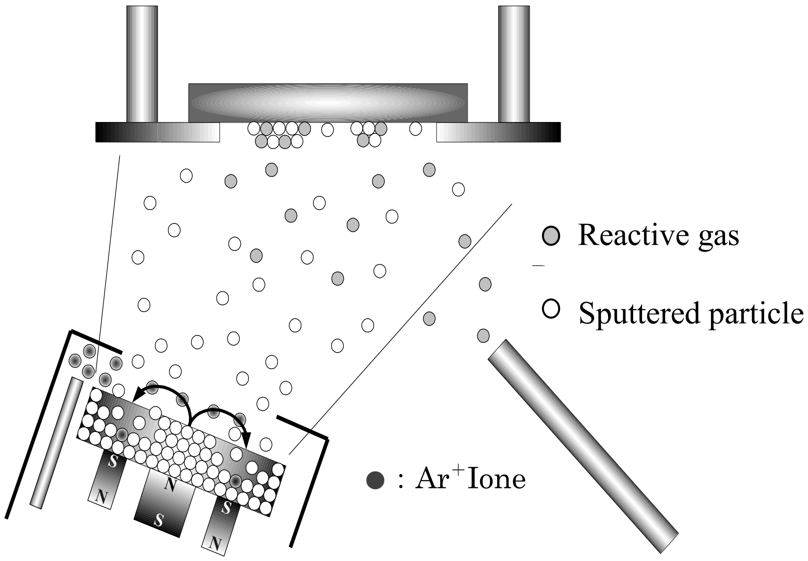

Figure 2.10 Conceptual diagram of reactive sputtering

Sputtering thin films of compounds can also be made by high frequency sputtering using the target of the compound of interest, but in that case many problems will arise. The first is the issue of target workability and price. The target requires a considerable area and thickness, and must be properly shaped. Since many compounds have a high melting point and brittle, so it is difficult to process, it is not always easy to create a target that meets the purpose with the high price. The second is the change in composition due to sputtering. Compounds are often decomposed into atoms and molecules during the sputtering process, and at that time all molecules with high volatility or vapor pressure are not incorporated into the thin film, resulting in a deficiency of a certain composition. The reactive sputtering method is a method for overcoming these disadvantages and appropriately controlling in the composition of the compound to bring out preferable physical properties. Specifically, the device is not a conventional sputtering method, but a method in which a reactive gas is simply mixed into the substrate. A prerequisite for the formation of a compound is that the atoms forming the compound collide with each other. Under normal sputtering conditions, collisions occur on the target surface, discharge space or substrate surface. However, collisions and combinations in the discharge space do not really matter much. Because the collision in the discharge space is a collision in the three-dimensional space, the collision with the target in the two-dimensional space such as the collision of migration atoms on the substrate surface and the collision of ions etc, will be low frequency compared to the above, and even if the plasma temperature is high and a two-body collision occurs, there is no escape for the thermal energy generated by the combination and it will eventually will analysis again soon. Therefore, the compounding or reaction will occur on the target and on the substrate, and both the compounding and sputtering will proceed simultaneously on the target.

The advantages of reactive sputtering equipment,

1) Ability to use metal targets.
2) It is possible to produce a thin film with a composition that is inclined in the thickness direction.

In general, many compounds have many insulators and a small sputtering rate. In that respect, if a metal target can be used, workability is good, and a DC sputtering device can be used, therefore the thin film formation speed can be increased. Moreover, during sputtering, when the pressure of the mixed gas is changed, a great advantage can be obtained to change the composition and physical properties of the thin film. In addition, the term reactive sputtering reaction is attached to the compounding on the substrate, and does not mean that the sputtering phenomenon on the target surface includes any reactive element. This is the difference from chemical sputtering. Here, if reactive sputtering is defined again, it can be said that "reactive sputtering is sputtering performed in a state where at least one composition of the compound thin film produced thereby is in a gas phase".

2.1.4.4 Helicon plasma sputtering system (10)

Among a variety of methods, a magnetron sputtering technique is most efficiently used to fabricate multilayers because of its high stability in deposition rate. Since the sputtered target particles have higher kinetic energies than thermal (up to few hundreds eV), thicker and tighter layers can be obtained using this technique than one using thermal or e-beam depositions, if the particles do not suffer the energy loss owing to collisions with ambient gases. In addition, higher reflectivity has been observed under lower gas pressure in the instance of W/C multilayers. The relation between the mean-free path of the particle, λ (cm) and the ambient gas pressure, p (Torr) is approximately expressed as

$$\lambda\text{-}10^{-2}/p$$

Under the conditions that the gas pressure is 1×10^{-2} Torr and that the distance between the target and the substrate (T-S) is 10 cm, the sputtered particle collides with the gases ten times in average before reaching the substrate, and easily loses most of its initial kinetic energy. On the other hand, long T-S distance is required for fabrication of a spatially uniform film with the magnetron sputtering technique because the target is not homogeneously sputtered by the plasma, depending on the detailed structure of the magnetic field. A helicon plasma magnetron cathode which consists of a conventional dc magnetron cathode and a spiral coil has been developed recently. Since the helicon wave provides electromagnetic power to the plasma in addition to the magnetron power, the discharge plasma can be maintained under a lower gas pressure than the instance with the conventional cathode. This feature can solve the contradictory problem in forming multilayers with the magnetron sputtering technique. Thus, we have developed the sputtering system which utilizes a pair of helicon plasma cathodes. A schematic drawing of the system is shown in fig 2.11. The chamber is evacuated with a turbomolecular pump (280 ι /s) and the base pressure of the chamber is lower than $1 \times 10\mathrm{m}^{-7}$ Torr. The target size is 50 mm in diameter. A pair of dc magnetron cathodes are arranged at the angle of 30° to the substrate normal. The substrate can be rotated up to 100 rpm during deposition for improving the uniformity of the deposited layer. Alternate deposition of the two materials is performed with a computer which controls an open-close mechanism of the shutters in front of the targets. Each of the three-turn coils placed between the target and the shutter is excited by the radio frequency of 13.56 MHz.

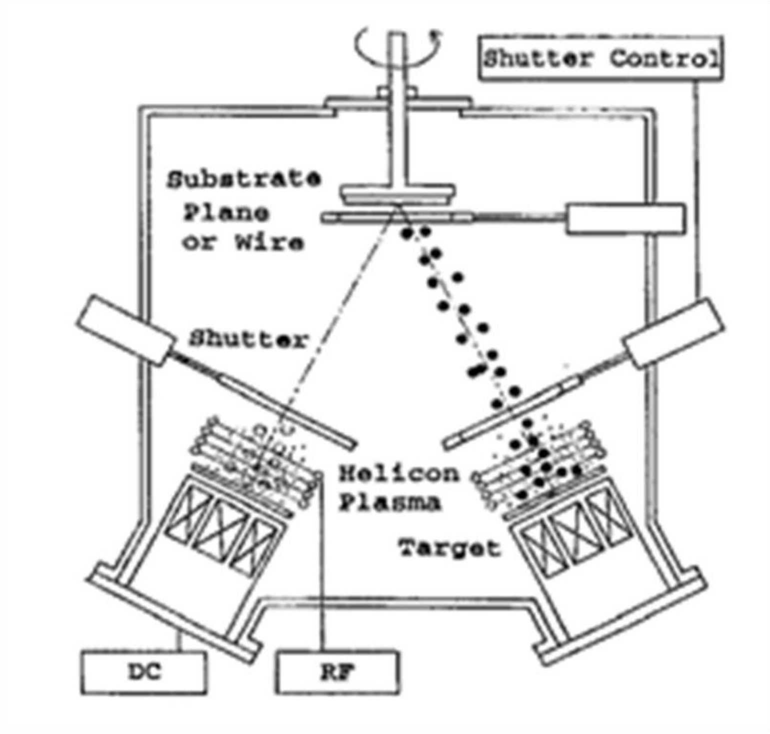

Figure 2.11 schematic drawing of helicon plasma sputtering system

2.1.5 Exhaust system specifications (9)

Table 2.2 below shows the specifications of each exhaust system of the multi-process coating system used in this study.

Table 2.2 Specifications of each exhaust system

Exhaust device name	Model name	Vacuum pressure	Rotation speed (50Hz)	Exhaust speed
Rotary pump	ULVAC D-330DK	$6.7x10^{-2}$Pa	950 rpm	253L/s
Turbo molecular pump	ULVAC UTM-1500M	$1.0x10^{-8}$Pa	26700 rpm	1600L/s
Oil diffusion pump	ULVAC ULK-10A	$2.6x10^{-6}$Pa	-	3400L/s

2.1.5.1 Exhaust principle of rotary pump (R.P) (9)

Rotary pumps (oil rotary pumps) are structurally classified into three types: rotary vane type, cam type and swing piston type. Figure 2.12 shows their principles structure and how to exhaust.

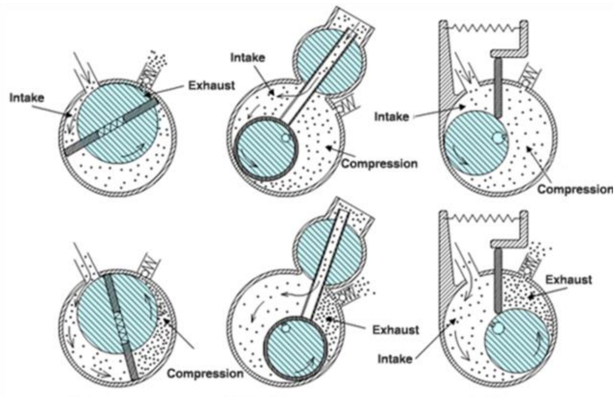

(a) Rotating vane type (b) Oscillating piston type (c) Cam type

Figure 2.12 Exhaust principle of rotary pump

The rotor pump of (a) is placed eccentrically so that the rotor touches the inner surface of the stator at a position intermediate between the intake port and the exhaust valve. Inside the rotor, there are two blades that slide in the machined groove, and they rotate while sticking to the inner surface of the stator by the force of the spring and the centrifugal force. One of the two spaces separated by the sliding blades serves as intake, and the other serves as compression and discharge. The swing piston of (B) type has a sleeve that slides in contact with the outer circumference of the rotor. The sliding blade is made integrally with the sleeve and is hollow. This one-piece structure is called a swing piston. The swing piston moves as a combination of swinging motion and vertical motion sliding in the hinge shaft as the rotor eccentricity rotates. When the swing piston comes to the top, the hollow part of the sliding blade gets inside the hinge shaft and the suction port is closed. In the cam type of (c), one sliding blade slides in the groove cut on the side of the stator. In addition to lubrication, the oil also serves to make moving parts of the pump airtight. Furthermore, when the suction pressure becomes low, the suction gas does not reach the pressure to lift the discharge valve even if it reaches the final process of compression. In such a state, the small volume of oil injected into the stage plays a role of pushing up the discharge valve. The rotary pump installed in the multi-process coating device has an oscillating piston type of film formation chamber and a rotary blade type for all others.

2.1.5.2 Exhaust principle of turbo molecule pump (T.M.P) (9)

A turbo molecular pump is a pump that mechanically knocks off gas molecules to obtain a vacuum. There are two types of turbines with blade rows are fixed blades and rotary blades, they are rotated at a very high speed of tens thousands of revolutions / minutes to make the speed of the blades comparable to the thermal speed of gas molecules and the gas that collides with the blades exhaust, by utilizing the fact that molecules gain momentum in a certain direction and generate a gas flow. Figure 2.13 qualitatively explains the principle of exhaust, the coordinates are based on the rotating blade that travels downward, so if the velocity of the blade is about the same as the velocity of the gas molecule, the gas molecule will have an upward relative velocity with respect to the blade, then the wing collisions are primarily at both ends of the upper wall of the opening.

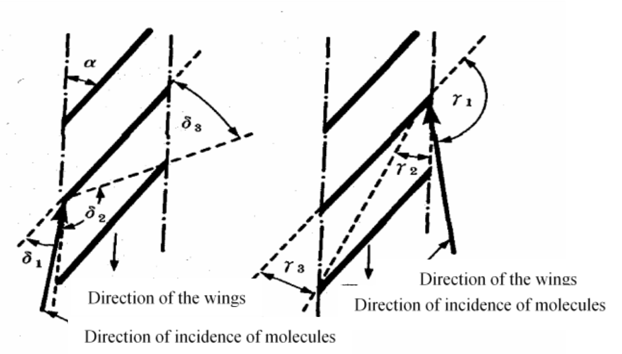

(a) Gas molecules enter from the intake port (b) Gas molecules enter from the exhaust port side

Figure 2.13 Exhaust principle of turbo molecular pump

Generally, it is assumed that molecules incident on the surface of the wing reflect according to the cosine law. In the case (a) where the gas molecules are incident from the intake port. Molecules reflected within the angle of δ1 return to the intake port, and those within the angle of δ2 enter from the side of exhaust port. Assuming that the transmission probability from the intake port side to the intake port side is Σ12, δ3> δ1 should be set in order to increase Σ12, and it is not difficult to design as such. On the other hand, (b) is the case where gas molecules are incident from the exhaust port side. Since γ1 >> γ3, the permeation probability Σ21 from the exhaust port side to the intake port side is small. The difference between the two permeation probabilities Σ12-Σ21 is proportional to the maximum exhaust rate, but since Σ12> Σ21 as described above, gas molecules can be exhausted from the intake port side to the exhaust port side. Therefore, in order to increase the exhaust speed, design a large absolute value of the difference between Σ12 and Σ21. However, since the maximum compression ratio is proportional to Σ12 / Σ21, it is necessary to design a large ratio of both transmittances in order to obtain a large compression ratio. To increase the exhaust speed, it is better to set the blade inclination angle α to 30 ° to 40 °, and to increase the compression ratio, it is effective to set α to 10 ° to 20 °. The actual turbo molecular pump has more than 10 rotary blades, and the several stages on the intake port side have a structure with a large exhaust speed even if the compression ratio is sacrificed, and the stage on the exhaust side has a compression ratio rather than the exhaust speed, and therefore increasing the values balance. An example of an actual turbo molecular pump is shown in figure 2.14. (a) is an example of using lubricating oil for the bearing of the drive shaft, and (b) can be freely mounted by using a magnetic levitation type bearing.

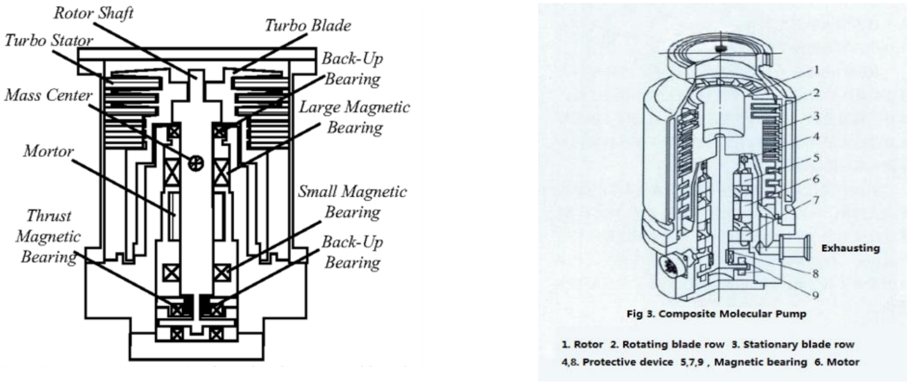

(a)

(b)

Figure 2.14 Turbo molecular pump

Figure 2.15 shows the relationship between the intake port pressure and the exhaust speed of a turbomolecular pump. Since the difference due to gas molecules is small and the decrease in exhaust speed is small even at a relatively high intake port pressure, it can be well matched with the auxiliary pump (in this study, a rotary pump was used). Compression ratio strongly depends on the mass of gas molecules. When the compression ratio is μ, the exhaust velocity is S and the mass of gas molecules is m, there is a relationship of $\log\mu \propto S \cdot m^{1/2}$ in the molecular flow region, therefore the more lighter molecule the compression ratio will smaller and the ultimate pressure will be lower. Therefore, when exhausting light elements such as hydrogen and helium, the compression ratio becomes extremely low, and it is necessary to be careful because it cannot be drawn to a high vacuum unless the pressure on the exhaust side is sufficiently low. Generally, auxiliary pumps and oil rotary pumps are used and the pressure obtained by these pump systems is about 10^{-8} Pa.

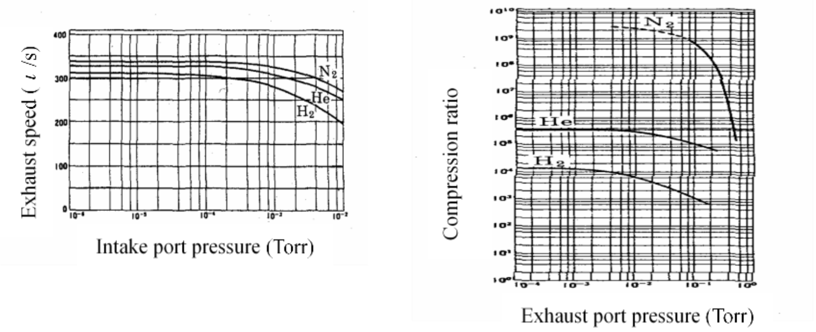

Figure 2.15 Compression ratio to exhaust port pressure of turbo molecular pump

Since the roughing of the vacuum device can be performed through a turbo molecular pump, this system does not require a roughing bypass circuit. In some cases, the main valve between the vacuum device and the turbo molecular pump can be omitted. In addition, since it does not require a cold trap or baffle, an oil-free ultra-high vacuum that does not contain hydrocarbons can be obtained. Therefore, there are few accessories that lower the exhaust conductance, and the exhaust speed of the pump becomes itself the effective exhaust speed, therefore a small and large exhaust speed can be obtained as a whole.

2.1.5.3 Exhaust principle of diffusion pump (D.P) (9)

Oil diffusion is a pump that exhausts by using a jet of oil or mercury, but currently does not use mercury. Fill the boiler with oil as shown in fig. 2.16 and roughen it with an auxiliary pump in advance. After that, when the boiler is heated, the oil evaporates in a vacuum and the steam is injected from the nozzle. When the injected oil hits the cooled diffuser, it condenses and collects in the return pipe and returns to the boiler and circulates in the pump. On the other hand, the steam diffused in the space without hitting the diffuser becomes a jet and moves in one direction. When gas molecules fly into the steam flow of this oil, the molecules that have been moving in the free direction collide with the heavy and fast oil molecules, so the momentum is given in the direction of the steam flow and flow in the direction of the exhaust side. In addition, gas coming from the opposite direction has a high oil density even if it tries to pass through the oil vapor layer, so it immediately collides with oil molecules and flows to the exhaust port as well, so it penetrates the oil layer, the number of molecules is reduced and the flow can flow to the exhaust side as a whole.

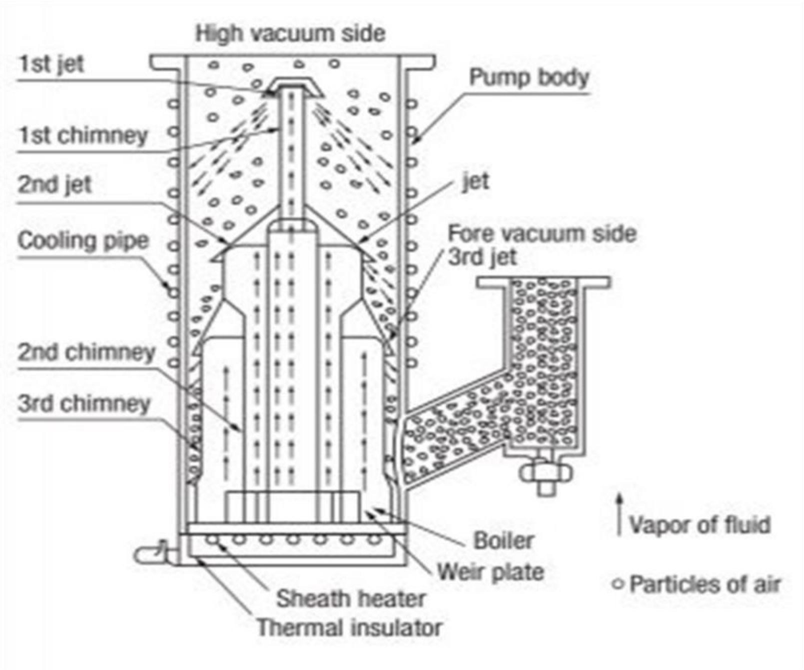

Figure 2.16 Oil diffusion pump principal diagram

References

1) ULVAC　Co. catalog

2) Masakazu Anpo, et al: *"High-performance titanium oxide photocatalyst" NTS Co., Ltd.*

3) Yasunori Taga, Fumiyoshi Saito: *"Practical Thin Film Process", NTS* **(2009)**.

4) Masakazu Anpo: "*High-performance Titanium Oxide Photocatalyst",* NTS **(2004)**.

5) Henry Windischmann. *Solid State und Materials Sciences*, 17 **(1992)** (6), pp.547-596.

6) J. T. Gudmundsson, *Plasma Sources Sci. Technol.* 29 **(2020)**, p113001.

7) Surmenev, R., Vladescu, A., Surmeneva, M., Ivanova, A., Braic, M., Grubova, I., & Cotrut, C. M. *Modern Technologies for Creating the Thin-Film Systems and Coating,* 8 **(2017)**, p12.

8) Yu.I.Belchenko, G.I.Dimov, V.G.Dudnikov, et.al. *Journal of applied Mechanics and Technical Physics,* 28 **(1987)** (4), pp568-76.

9) Harsha: *Principles of Physical Vapor Deposition of Thin Films Ch01*, 200 **(2007)**.

10) Verhoeven, E. Puik, and van der Wiel. *Vacuum,* 39**(1989)**, p.711.

11) H. Nagata and S. Seki, Jpn. J. *Appl. Phys*, 29 **(1990)**, p.569.

Chapter 3 Thin film evaluation methods

3.1 X-ray diffraction (XRD) (1)

The crystal structure and crystal grain size of the copper oxide (Cu_2O, CuO) thin film produced in this study were measured by X-ray diffraction. The outline of the X-ray diffraction method is shown below. Diffraction lines are observed when the atoms that make up an object are regularly arranged and the X-rays scattered by each atom are in phase and strengthen each other. The diffraction phenomenon is closely related to the arrangement of atoms, and the X-ray diffraction pattern is determined by the crystal structure of the substance.

3.1.1 X-ray properties (2)

X-rays are the same electromagnetic waves as visible light, and their wavelengths are approximately 0.01 to 10 nm. Figure 3.1 shows the classification of electromagnetic waves2).

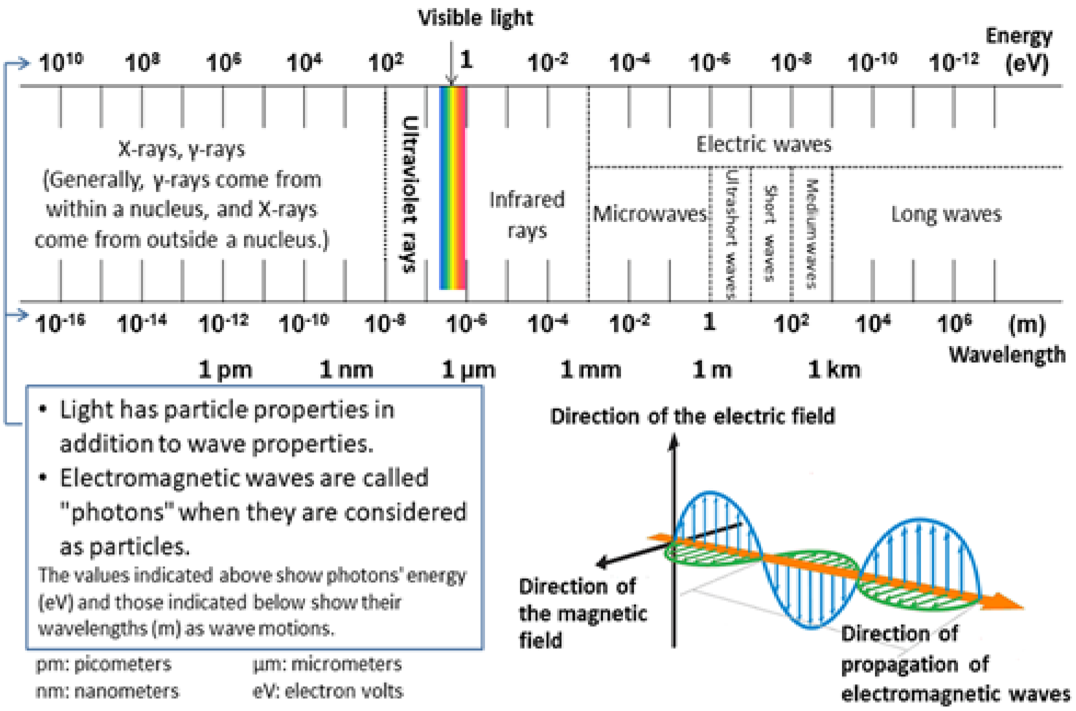

- Light has particle properties in addition to wave properties.
- Electromagnetic waves are called "photons" when they are considered as particles.

The values indicated above show photons' energy (eV) and those indicated below show their wavelengths (m) as wave motions.

pm: picometers
nm: nanometers
μm: micrometers
eV: electron volts

Figure 3.1 Types of electromagnetic waves

X-rays have similar properties due to their extremely short wavelength compared to light, but have several different properties. As a property similar to light, it travels in a vacuum at the same speed as light. Also, like light, it behaves as a wave at one time and as a particle at another time. Waves are characterized by wavelength λ and amplitude (magnitude of electromagnetic field vector) and show diffraction phenomenon. Particles are characterized by the property of being counted one by one. X-ray particles are called (X-ray) photons or photons, and one photon is inversely proportional to the wavelength λ and has a photon energy E.

$$E=hc/\lambda \Rightarrow E=1239.8/\lambda \text{………} \ (3.1)$$

In this way, waves and particles are linked by the relationship above λ and E. Furthermore, the amplitude in the wave is a quantity proportional to the number of X-ray photons, and is a quantity proportional to the intensity of X-rays. X-ray intensity, in the measurement with a counter the number of X-ray photons that are incident and counted through the window of the counter in a unit time, that is the counting rate is used as the X-ray intensity. The magnitude of X-rays is not the magnitude of the energy of photons but the number of photons per unit time. It is not the intensity but the quality of the radiation (transmission ability, etc.) that differs depending on the magnitude (wavelength) of the photon energy. X-ray analysis does not use X-ray intensity as a unit. One roentgen (R), which is the unit of exposure, the X-ray produces positive and negative ions with an elementary charge of 1 esu in 0.001293 g of air. Note that 1 mR / h is approximately 200 photons / cm^2 sec for X-rays with a wavelength of 0.154 nm (Cukα). Counting this with a counter with an effective window area of 2.5 cm2 gives about 500 cps (assuming a counting efficiency of 100%). As shown in fig 3.2, X-rays are generated by creating very high-velocity electrons in a vacuum and colliding them with the anti-cathode (target). In this case, the rate at which most of the kinetic energy of electrons is converted to heat (generation efficiency) is given by the following equation, and is usually a small value of about 0.1%.

$$\varepsilon=1.1\text{x}10^{-9}ZV\text{………} \ (3.2)$$

ε: Generation efficiency Z: Atomic number of target element V: Acceleration voltage (V)

Therefore, the maximum X-ray dose obtained from an X-ray tube depends on the melting point of the target element and the thermal conductivity. Normally, the target of

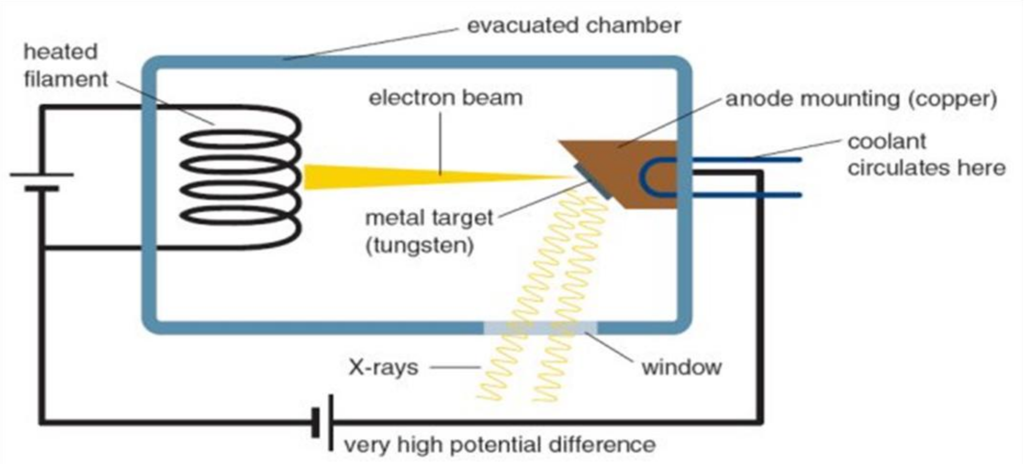

Figure 3.2 X-ray generation

an X-ray tube is Cr, Fe, Co, Cu, Mo, Ag, W, etc. Cu is used as a standard, and the heat of the target is dissipated by cooling water.

3.1.2 X-ray scattering (2)

When the X-rays are incident on a substance, the primary X-rays are absorbed or scattered as shown in fig 3.3. Scattered X-rays are called secondary X-rays,

(1) X-rays of the same wavelength as the next X-ray (elastic scattering, coherent scattering, Thomson scattering).

(2) X-rays with slightly longer wavelengths than primary X-rays (inelastic scattering, non-coherent scattering, Compton scattering).

(3) Fluorescent X-rays (characteristic X-rays due to the photoelectric effect) are emitted again. These scatterings are due to electrons, not nuclei. Caused by scattered X-rays of the same wavelength as primary X-rays (Thomson scattering). The wavelength change △ λ at this time is given by the following equation.

$$\Delta\lambda = \frac{h}{mc}(1-\cos\phi) = 0.0243(1-\cos\phi)\text{...........}(3.3)$$

However,

h: Planck's constant

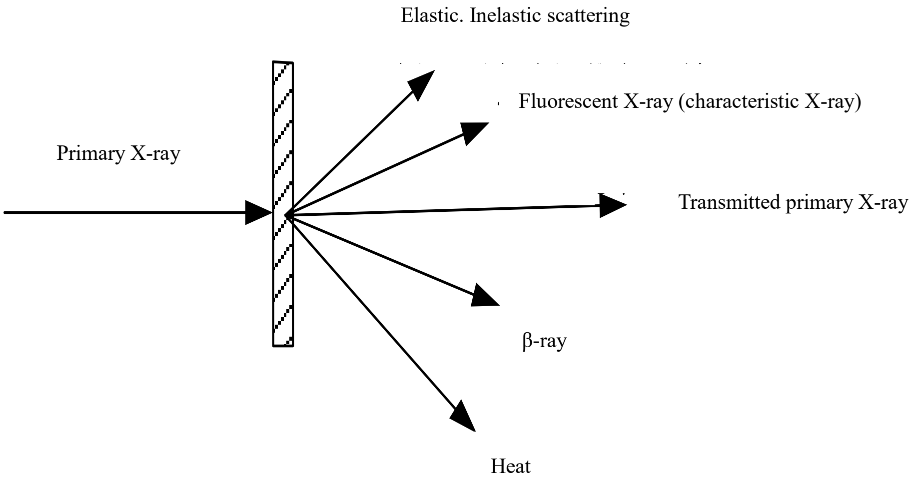

Figure 3.3 Conversion of X-ray energy

m: Electron mass
c: Speed of light
φ: Angle formed by incident X-rays and scattered X-rays

This is non-coherent scattering, does not show diffraction phenomena and is emitted in all directions, which contributes to the background of diffracted X-rays. Fluorescent X-rays are used for elemental analysis by utilizing the diffraction phenomenon of spectroscopic crystals.

3.1.3 X-ray diffraction by crystal (2)

When X-rays are applied to a crystal, scattered X-rays from each atom in the crystal are superimposed. This is non-coherent scattering, does not show diffraction phenomena and is emitted in all directions which contributes to the background of diffracted X-rays. Fluorescent X-rays are used for elemental analysis by utilizing the diffraction phenomenon of spectroscopic crystals. As shown in Fig 3.4, when X-rays are incident at an angle of α and scattered at an angle of β, the path becomes different of X-rays from two points x apart on the atomic network surface, and the path difference is an integral multiple of the wavelength n, Strengthen each other when equal to nλ.

$$x(\cos\alpha - \cos\beta)............(3.4)$$

Then now if the scattered X-rays from all points on the atomic network surface are in phase,

If $n\lambda=0$, and $\alpha=\beta$

Therefore, the interference phenomenon that gives the maximum intensity on one atomic network surface is when the incident angle and the scattering angle are equal. After that, consider the interference of scattered X-rays from a large number of lattice planes as shown in fig 3.5. For X-ray interference between the first surface and the second surface, only the path difference due to the distance between the first surface and the second surface becomes a problem. Similarly, in the case of interference between the first surface and the third surface and other parallel surfaces, only the path difference due to the surface spacing becomes a problem. From fig 3.5, the path difference between the first and second surfaces is 2ds in 2dsinθ, which strengthens when the wavelength is an integral multiple.

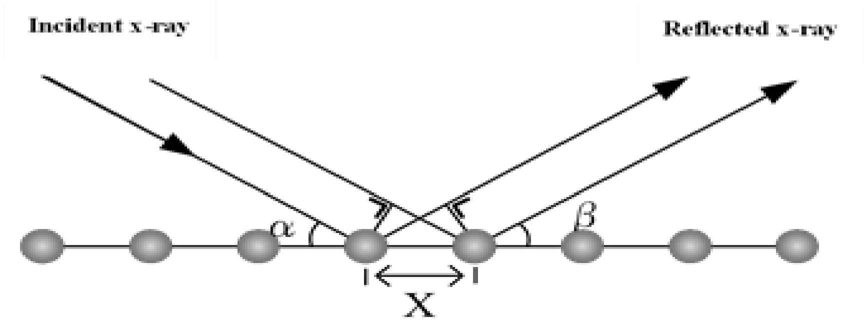

Figure 3.4 Scattering by crystals

$$2d\sin\theta = n\lambda................(3.5)$$

D: Atomic network spacing (lattice spacing)
θ: Bragg angle
Incident angle = Reflection angle = θ
λ: Wavelength of X-ray used
n: Reflection order
This is called Bragg's formula.

$$\sin\theta = \frac{n\lambda}{2d} \le 1 \text{.............}(3.6)$$

Therefore, diffraction does not occur unless $\lambda < 2d$ at least. Although n represents the reflection order, it is customary to think of it as the first-order reflection from a virtual surface (hkl) such that the surface spacing is d / n.

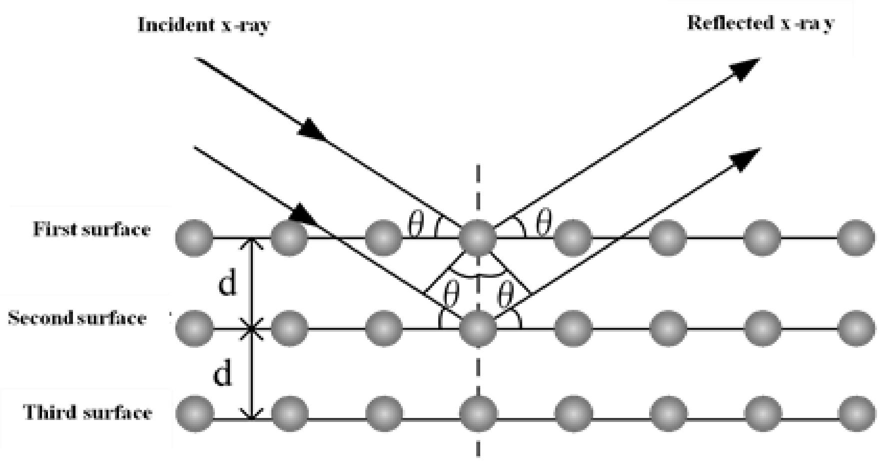

Figure 3.5 Bragg's diffraction conditions

3.1.4 Crystalline size (2)

Debye-Scherrer derived the following equation assuming that the crystal is not distorted, the crystallite size is uniform and the width of the diffraction line is based only on the crystallite size.

$$D_{hkl} = \frac{K\lambda}{\beta\cos\theta} \text{.............}(3.7)$$

Dhkl is the size of the crystallite in the direction perpendicular to the (hkl) plane (nm), λ is the wavelength of the X-ray (nm), β is the diffraction line width (rad), and θ is the diffraction angle (°). K is a constant, 0.9 when the half width β1 / 2 is used for β, and 1 when the integral width βi is used 1.84 for layered irregular grid. The full width at half maximum is the diffraction line width measured at half the height of the diffraction line. The integrated width means the width of a rectangle that is the same as the height of the diffraction line and has the same area. Since the spread of the diffraction line width includes the spread based on the optical system, it is necessary to correct the spread (b) based on the optical system from the actually observed diffraction line width B. As a standard sample for that purpose, it is ideal if a sample with large crystals (25 to 50 μ m) and no non-uniform strain can be obtained with the same substance as the measurement sample, if it is impossible, use annealed ones α-quartz powder at 800 ° C. When the crystallite size of the sample is smaller than 50 nm, the value obtained by subtracting the diffraction line width (b) of the standard sample from the measured diffraction line width B is defined as β.

$$\beta = B - b\text{..............}(3.8)$$

When the crystallite size of the sample is larger than 50 nm, the measured value B of the diffraction line width approaches the diffraction line width (b) of the standard sample. Measurement error increases in this area, so $K_{\alpha 1}K_{\alpha 2}$ require double line correction. Measurement is virtually impossible above 200 nm. In addition, in the region where the crystallite size is smaller than 2 nm, it is difficult to separate the peak and background, so it is virtually impossible to measure. Figure 3.6 shows full width and integration width at half maximum.

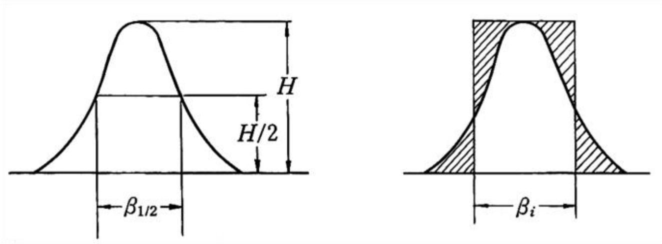

Figure 3.6 Full width at half maximum and integration width

3.2 X-ray photoelectron spectroscopy (XPS) (3,4)

In this study, the composition and chemical bond state of the formed thin film were measured using Mg (1242.6 eV) with an X-ray photoelectron spectrometer (Shimadzu Seisakusho Co., Ltd., ESCA-KIS). X-ray photoelectron spectroscopy is widely used for characterization of almost all solid materials such as metallic materials, inorganic materials, organic materials, and semiconductor materials. This is because the range of applicable substances is wider than that of Auger Electron Spectroscopy (AES), and the damage and charge-up of the sample are smaller in X-ray irradiation than in electron beam irradiation. XPS is often used for the purpose of state analysis, as can be seen from the fact that it is sometimes called ESCA (Electron Spectroscopy for Chemical Analysis), which is a feature of various electron spectroscopy methods. In addition, quantitative analysis of the surface is also performed on a daily basis, and in contrast to the depth direction analysis, which occupies the main part in Aussie electron spectroscopy, the vicinity of the surface is often targeted. XPS is a spectroscopy method that irradiates a solid sample with X-rays and measures the energy and intensity of the emitted electrons. Elements can be identified and quantitatively analyzed from the energy positions and intensities of electrons (photoelectrons) directly emitted by this X-ray irradiation. In addition, it is possible to know the difference in chemical state even for the same element from the minute difference in peak energy position, which enables state analysis. When a sample is irradiated with X-rays with constant energy (hv), photoelectrons are emitted from it as shown in (figs 3.7 and 3.8), and the kinetic energy of photoelectrons is expressed by the following equation.

$$E_k = hv - E_b \text{------}(3.9)$$

E_b is the binding energy of the electron of interest. E_k is required by measuring with a spectrometer. Since this electron emission process is actually affected by the work function φ of the device, Eq (3.9) becomes as follows.

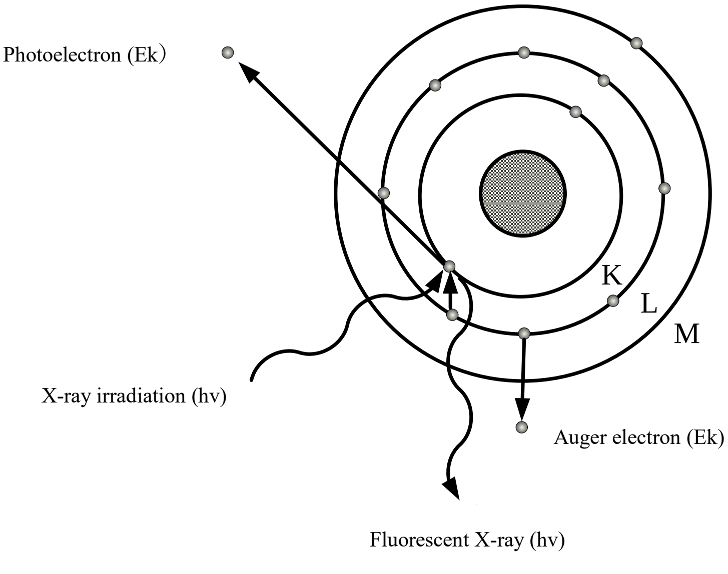

Figure 3.7 Photoelectron emission process

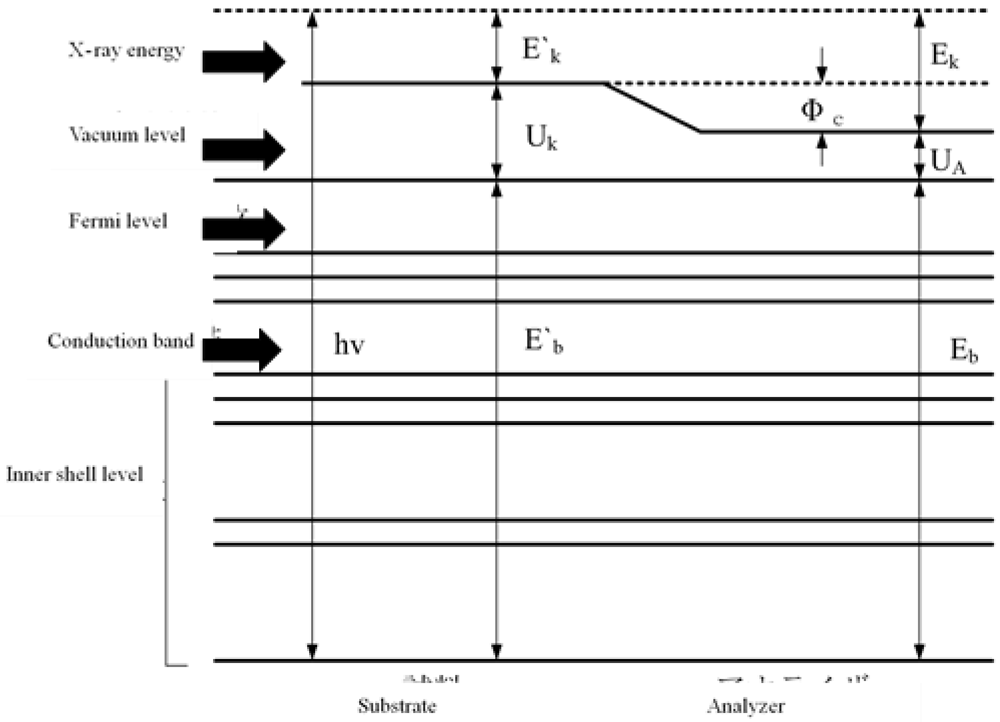

Figure 3.8 Relationship between X-ray energy, electron binding energy and kinetic energy

$$E_k = hv - E_b - \varphi \ldots \text{(3.10)}$$

In XPS measurements, in addition to photoelectron spectra, auger electron spectra of X-ray excitation are also observed and they are often used for elemental analysis and state analysis. However, unfortunately, the energy of X-ray sources such as normal AI and Mg cannot often excite the auger peak in the inner shell of the high energy region. The observed auger electron kinetic energy is expressed by Eq (3.11).

$$E'_k = E_k - E_L - E'_L \ldots\ldots\ldots\ldots\ldots \text{(3.11)}$$

(In the case of KLL auger electron, ,,, is the energy level of the orbit of each atom)

3.2.1 X radioactive source

The radiation source that is required for XPS is monochromatic X-rays with the same energy. As a monochromatic X-ray source, characteristic X-rays of inner-shell electrons generated by electron impact of a substance are used. Typical examples are (1486.6eV natural width: 0.83eV) and (1242.6eV natural width: 0.68eV). These are excellent sources but the X-rays that are actually emitted include satellite and bremsstrahlung X-rays. Therefore, in order to remove these, X-ray spectroscopy using crystals is performed and it is used as a monochrome X-ray source.

3.2.2 Composition and chemical state analysis

In this study, MGKα ray (1486.6 eV) have used for analyzing. Binding energy was calibrated at a value of 368.3 eV of AG3D5 / 2. The value of binding energy is unique to each element. This value has already been measured or calculated for each element. Therefore, element identification is possible by comparing the binding energy of the spectrum of an unknown sample with a known value. In an actual substance, the binding energy changes depending on the bonding state of the target atom. The most important feature of XPS is to measure this change and estimate the existence state of atoms. Qualitatively, if the binding energy of an element is considered based on a single element, it is sufficient to consider how the electron bias is generated by the bonding of atoms in the element. Outer-shell electrons are directly involved in bonding but inner-shell electrons are also slightly affected by this. In other words, if an element that strongly attracts electrons (large electronegativity) is bound, binding energy shifts to the higher side (chemical shift is positive). As an example, the electronegativity of oxygen is higher than that of ordinary metals, so various oxides correspond to this.

3.2.3 Depth direction analysis

The ion sputtering is usually used in combination; therefore, the depth direction analysis can be performed in the same way as AES and Ar is usually used for ions. Depth resolution is generally poorer than AES. This is partly because the measured area is larger than AES and the kinetic energy of the peak to be detected is large. When performing this analysis with XPS, it is necessary to pay close attention to the deterioration (reduction often occurs) of the material due to ion sputtering.

3.3 Surface morphology and cross-section measurement method

3.3.1 Measurement principle of atomic force microscope (AFM) (5)

Figure 3.9 shows the scanning probe microscope (SPM-9500, Shimadzu Corporation) that used in this study. First, a laser is applied to the back of a cantilever with a silicon nitride probe. A gold foil is attached to the back of the cantilever and it is reflected by shining a laser beam on it and a PSD (optical displacement detector, photocurrent generated by incident light) using a 4-split photodiode is placed in pairs. By detecting by (converting the position into a voltage by flowing it through an electrode), it is possible to detect how much the cantilever has flexed due to the interaction with the sample.

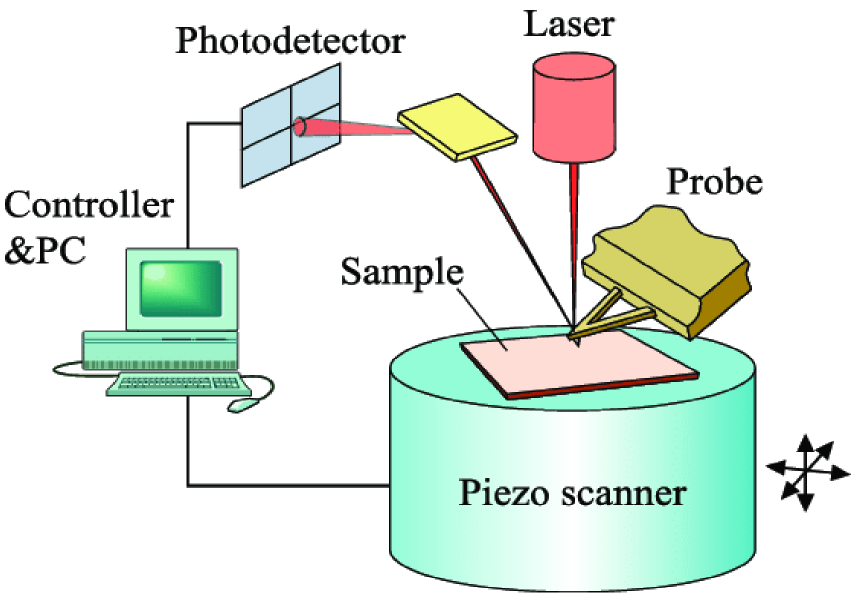

Figure 3.9 Atomic force microscope device

The major features of AFM are as follows.

1. Measurement can be performed without distinguishing between conductors, semiconductors, and insulators.
2. Since the measuring force is extremely small, it can be measured almost non-destructively. The measurement mode also includes a contact mode, a non-contact mode and a tapping mode.
3. It can be measured in various environments such as in the atmosphere and vacuum.
4. Three-dimensional shape information can be obtained with atomic resolution.

The surface roughness Ra calculated in this study is extracted from the roughness curve by the reference length ℓ in the direction of the average line as shown in fig 3.10, and the absolute value of the deviation from the average line of this extracted part to the measurement curve is totaled, and it is the average value as shown in Eq (3.12).

$$Ra = \frac{1}{\ell}\int_0^{\ell}|f(x)|dx \cdots\cdots\cdots\cdots. (3.12)$$

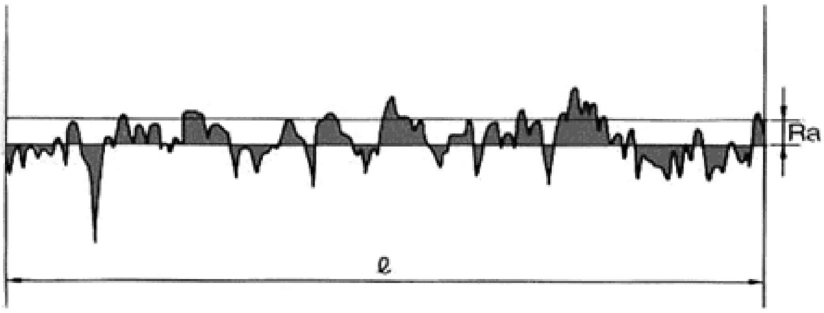

Figure 3.10 Surface roughness calculation method

3.3.2 Measurement principle of scanning electron microscope (SEM) (6)

An optical microscope shines light on a sample and observes the shape of the sample by the reflected light. On the other hand, an electron microscope observes the shape by using electrons generated when a thin electron beam (electron beam) is applied to a sample instead of light. However, since it is not possible to capture the sample shape by irradiating only one point of the sample with an electron beam, the secondary electrons or backscattered electrons are captured by a detector while scanning the irradiation position of the electron beam and the surface shape is captured on the monitor. The structure of the SEM is shown in fig 3.11.

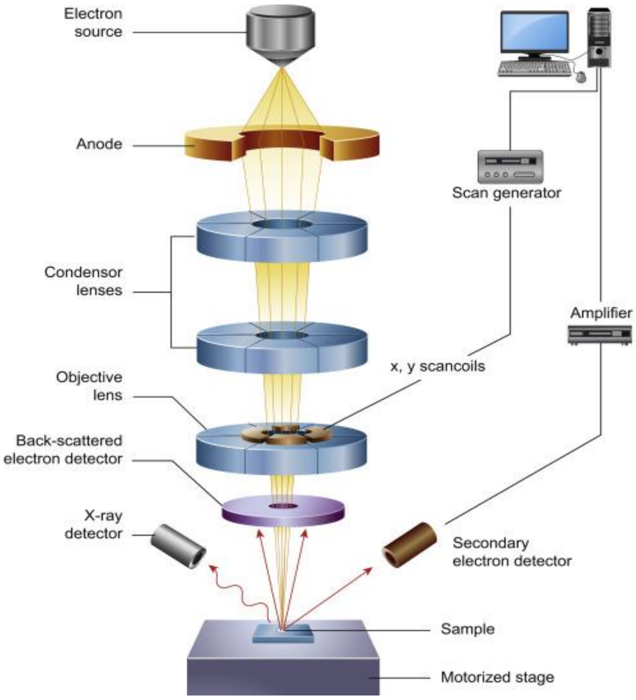

Figure 3.11 SEM structure

3.3.3 Laser Scanning Microscope (LSM) (7)

Figure 3.9 also shows the illustration figure of Laser Scanning Microscope (OLS4500, Olympus Corp.) that employed to observe the surface morphology. The planar resolution of an optical microscope depends largely on the wavelength of light used. Laser microscopes that use short-wavelength laser light have better planar resolution than conventional microscopes that use visible light. The OLS4500 uses a 405nm short wavelength semiconductor laser, and achieves a maximum planar resolution of 0.12μm by combining a dedicated objective lens with a high numerical aperture (N.A.) and a confocal optical system. In addition, XY scanning with Olympus' original 2D scanner enables high-resolution scanning of up to 4096 pixels x 4096 pixels.

3.4 Hall Effect measurement (7)

3.4.1 Summary

When a magnetic field is applied perpendicular to the direction of the conductor through which the current is flowing, an electromotive force is generated in the direction perpendicular to both the current and the magnetic field. This phenomenon is called the Hall effect and was discovered by E.H. Hall in 1879 in metal thin film samples. In an electric conductor placed in a magnetic field, many conduction phenomena different from those in the absence of a magnetic field can be seen. This is called the current magnetic effect. The electrical resistance shall be measured with a constant current flowing through a sample with electrodes arranged as shown in fig 3.12.

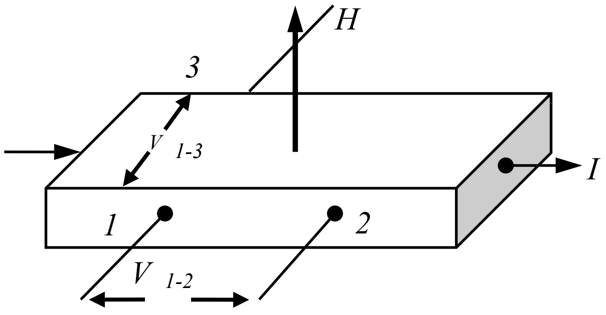

Figure 3.12 Hall effect measurement

When a magnetic field is applied,

(1) The voltage between electrodes arranged in the direction parallel to the current changes as a function of the magnetic field, which is called the magneto resistive effect.
(2) On the other hand, when there is no magnetic field, the potential difference between the electrodes 1-3 arranged in the direction perpendicular to the current is normal, but when a magnetic field is applied, a voltage is generated, this is called the Hall effect.

Hall effect measurement is one of the effective means to know the electrical characteristics. This section describes the principle of the Hall effect and the actual measurement.

3.4.2 Principle

Magnetic fields affect electrons in two ways. One is the effect that the orbital state of electrons is directly affected by the magnetic field. In classical theory, this effect is taken in as the Lorentz force acting on electrons with velocities in a magnetic field. The other is the effect on the spin of electrons, since spins placed in a magnetic field have different energies depending on their direction, the spin distribution changes, which affects the motion of electrons. When the carrier is one type of electron or hole when an electric field is applied in the direction as shown in fig 3.13, the electron works in the direction and the hole works in the direction. Furthermore, when a magnetic field is applied in the direction, both electrons and holes receive Lorentz force in the direction and have a velocity component in the direction. This current causes an electric charge to accumulate in the sample, and an electric field Ey appears in the y direction. This is called a hall electric field. Here, the equation of motion for electrons is,

$$m(\frac{d}{dt}+\frac{1}{\tau})v=-e(E+v\times H)\text{................}(3.13)$$

It is expressed as, is relaxation time. Regarding the velocity component in the steady state is established.

$$\frac{mV_y}{\tau}=-e(E_y-v_xH)\text{................}(3.14)$$

Furthermore, under the condition that no current flows in the y direction,

$$-eE_y=ev_xH\text{......................}(3.15)$$

From this equation, it can be seen that the Lorentz force acting on the electrons and the force due to the Hall electric field are proportional to the magnetic field H and the current density I_xnev_x (*n*: electron density) in the steady state R_h often. It will be from the above formula,

$$R_H=\frac{E_y}{I_xH}=-\frac{1}{ne}\text{................}(3.16)$$

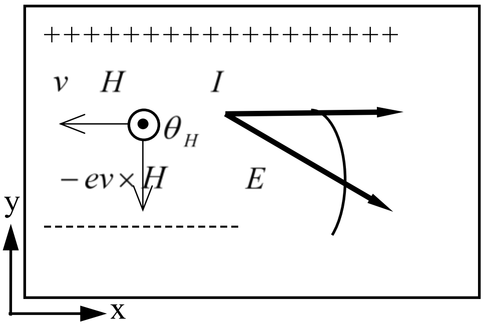

Figure 3.13 Hole angle θ_H ($\tan\theta_H$ = | E_y / E_x |)

This equation explains that the carrier density, which is one of the important physical quantities representing the physical properties of the conductor, can be estimated from R_h. The negative sign on the right side of the equation is due to the negative electron charge. That is mean, the type of carrier can be known from the sign of the Hall coefficient. Furthermore, the product of the Hall coefficient and the electrical conductivity gives the carrier mobility. The electric field vector and the current vector are not parallel in the magnetic field, but the angle θ_H between them is called the Hall angle and is given by $\tan\theta_H = |E_y / E_x|$ at (fig 3.13). It may be used as an index of how much the carrier's traveling direction is bent by the magnetic field. By the way, when the quantum Hall effect is occurring, the Hall angle is in the limit state of θ_H=90°. There are two types of carriers, electrons and holes, the current density is given by $I=I_e+I_h$ ($I_{e,h}=n_{e,h}e\,v_{e,h}$: current density of each electron and hole alone). In this case, the Hall coefficient is multiplied using the respective mobilities.

$$R_H = \frac{n_h\mu_h^2 - n_e\mu_e^2}{e(n_h\mu_h + n_e\mu_e)^2} \text{......................(3.17)}$$

When the electron density and the hole density are equal like a semimetal, ($n=n_e=n_h$) will be uncomplicated as the following equation.

$$R_H = \frac{1}{n_e}\frac{\mu_h - \mu_e}{\mu_h + \mu_e} \text{......................(3.18)}$$

Since the hole coefficient when two types of carriers exist depends not only on the carrier density but also on the magnitude of each mobility, the carrier density cannot be estimated directly from the hole coefficient. However, in the case of semiconductors, it is possible to know the upper limit of carrier density and the lower limit of mobility of either electron or hole. For example, if the Hall coefficient is positive, the above equation concludes that $\mu_h > \mu_e$ and that $n < 1/e R_h$ holds for carrier density. Also, $\mu_h > \sigma R_h$ is given for hole mobility (9).

3.5 UV-VIS absorption spectrophotometry (8)

3.5.1 Summary

There are many optical analysis methods depending on the wavelength of the electromagnetic wave. Here, the visible and ultraviolet light absorption analysis methods will be described. In the wide wavelength range of electromagnetic waves that shown in fig 3.1, the human naked eye perceives a very narrow range of 400 to 800 nm.

Analytical methods that utilize the absorption of light by a solution (or solid) are very widely used. Since the color intensities were compared with the naked eye for many years, it was generally called colorimetry, but spectrophotometry and absorption spectrophotometry became more common.

For example, the $KMnO_4$ aqueous solution exhibits a magenta color. This is because MnO4 absorbs green light with a maximum absorption and not absorbing reddish purple light at 525 nm (fig 3.1). While, when the green light is removed from the white light, it looks magenta. This relationship is called complementary color. Therefore, what we see is the complementary color of the light absorbed by the solution. In general, spectroscopy using solution coloring is sensitive and accurate.

3.5.2 Photo energy

There is a relationship of E = hν between the light energy E and the frequency ν, while ν = c / λ holds between the wavelength λ and the light velocity c, and ν. Therefore,

$$E = hc / \lambda \qquad \ldots\ldots\ldots\ldots (3.19)$$

That is, the shorter the wavelength of an electromagnetic wave, the greater the energy. Speaking of visible light, purple light has more energy per photon than red light. For example, with 500 nm light (turquoise),

$$v = \frac{c}{\lambda} = \frac{3\times10^{10}\,\text{cm/sec}}{5\times10^{-5}\,\text{cm}} = 6\times10^{14}\,\text{/sec}.................(3.20)$$

Since ν is such a large number, 1 / λ, which is proportional to ν, is used for light of 500 nm, 1 / λ = 1 / (5 × 10^{-5}) = 20000 cm^{-1}. The energy of one photoelectron of light with λ = 500 nm is,

$$E = \frac{hc}{\lambda} = \frac{6.62\times10^{-27}\,\text{erg}\cdot\text{sec}\times3\times10^{10}\,\text{cm}\cdot\text{sec}^{-1}}{5\times10^{-5}\,\text{cm}} = 3.97\times10^{-12}\,\text{erg} = 3.97\times10^{-19}\,\text{J}$$

Multiply the Avogadro number for 1 molar photon,

$$E=3.97\times10^{-19}\times6.02\times10^{23}=2.39\times10^{5}\text{J}=239\text{kJ}=57.1\text{kcal/mol}$$

Visible light is 315 kJ at 380 nm (purple) and 153 kJ at 780 nm (red).

3.5.3 Visible and violet absorption

Absorption of light means that its energy is absorbed by the numerator. If a molecule in the most energetically stable state (ground state) absorbs energy, it becomes a state with higher energy (excited state). The energy difference ⊿E between the two states is expressed by assuming that the frequency of the absorbed light is ν.

⊿E = hν (h is Planck's constant)

There are many energy states (units) of molecules, not one or two but all are unique to each molecular species, therefore, transitions between levels absorb light of a specific frequency. When visible / ultraviolet light is absorbed, the energy state of electrons in the molecule can be known. As shown in fig 3.14, the energy of electronic transition is relatively large, and the state of vibration and rotation of the molecule changes accordingly. There are vibrational levels and rotational levels that accompany each electronic transition level, and complex transitions occur between them, so the energy is no single. There are several types of electronic transitions in the case of metal complexes. a) Transition between d orbitals of transition elements (d-d transition), b) Transition within a ligand with a conjugated double bond, c) Metal-to-ligand (or ligand-to-metal) charge, for example, moving. Many of the ions of transition elements such as Cu^{2+}, Co^{2+}, and Ni^{2+} are colored by themselves, but the cause is the d-d transition.

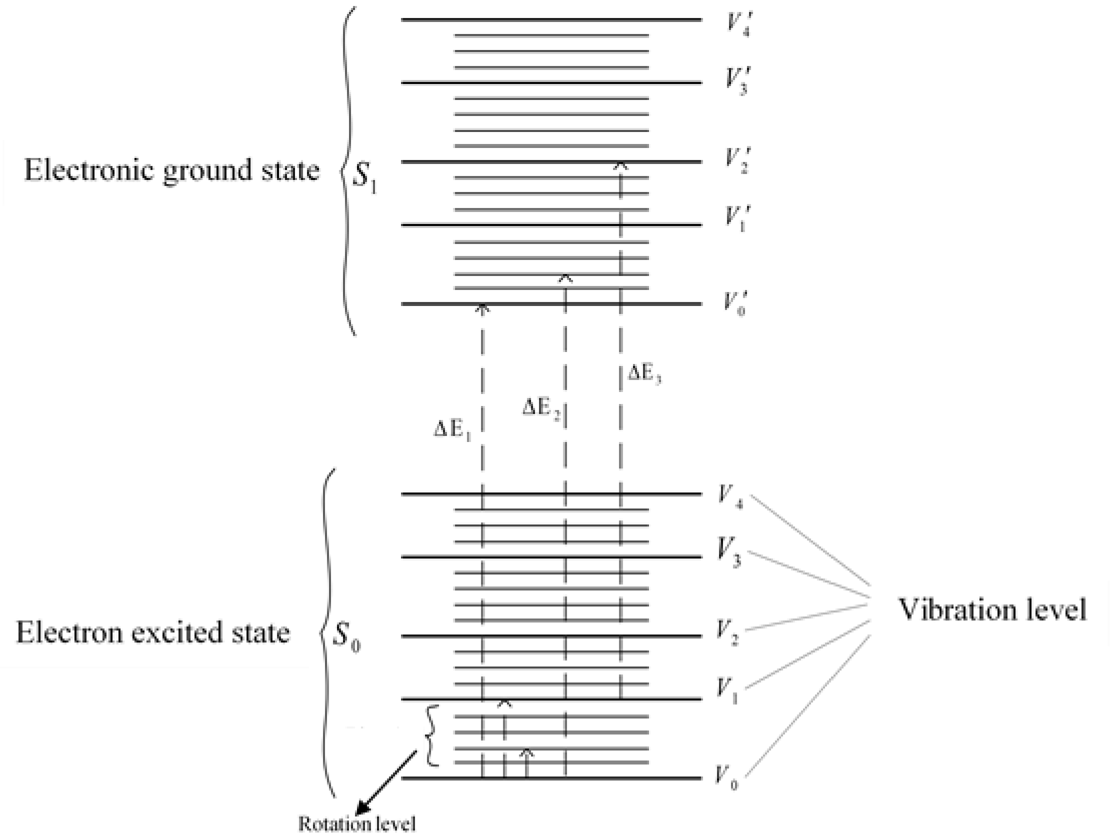

Figure 3.14 Molecular energy level

In the case of an octahedral complex, five d-orbitals that originally have the same energy are triple-coordinated t_{2g} orbitals (having low energy) under the influence of the electrostatic field, due to the ligand bound to the metal ion) and doubly degenerate E_g orbitals (with high energy). The electronic transition between the split d-orbitals is the d-d transition. However, the probability that this transition will occur is relatively small, and as a result, the coloring is weak for the density. Compared to this, the transitions of b) and c) have a high probability of transition, and there is a possibility that the color will be strongly colored even at low densities. In b), there is a high probability that the $\pi \rightarrow \pi^*$ transition, in which the π bond transitions to the bonding orbital, occurs. The charge transfer (CT) transition in c) is also a transition that occurs with high probability. In the 1,10-phenanthroline complex $[Fe(phen)_3]^{2+}$ of Fe (II) used for the absorptiometry of Fe, the d electron of the Fe atom moves to the π orbital of phenanthroline. In this way, it is widely practiced to select a reagent that develops a strong color by reacting with a low-concentration quantitative component and use it in the absorptiometry.

3.5.4 Calculation method of optical band gap

By irradiating a substance with light, electronic transitions peculiar to the substance can be induced, and the electronic state can be estimated from the obtained absorption spectrum. In this study, the transmittance of the sample was measured using an ultraviolet-visible spectrophotometer (UV-2550, Shimadzu Corporation), and the optical bandgap was estimated from the results. The absorption coefficient α calculated from the transmittance is the forbidden band width (bandgap energy) Eg, light frequency ν, Planck's constant h and light velocity, assuming that the bottom of the conduction band and the top of the valence band are parabolic, expressed as follows using c.

(a) In the case of direct transition type

$$\alpha \propto (h\nu - Eg)^{1/2} = (h\frac{c}{\lambda} - Eg)^{1/2} \text{...............(3.21)}$$

(b) Indirect transition type

$$\alpha \propto (h\nu - Eg)^{2} = (h\frac{c}{\lambda} - Eg)^{2} \text{...............(3.22)}$$

As copper oxides is an indirect transition type, Eq (3.21) was used as the equation for obtaining the bandgap energy. If α^2 is plotted against the photon energy hν and the extension of the obtained straight line and the point where $\alpha^2 = 0$ intersect are obtained, the energy value at that point becomes the optical bandgap energy Eg.

3.5.5 Calculation method of transmittance

The main measurement methods in the spectrophotometer are the transmission method and the reflection method, and there are applied measurement methods based on these measurement methods. Directly transmitted light, diffused transmitted light, and total transmitted light are measured, and a spectrum in an arbitrary wavelength range and a photometric value of a specific wavelength are acquired and from the obtained results, it is possible to evaluate the chemical properties, quantification and optical properties of the sample. The transmittance T (%) is defined as shown in fig 3.15 by the intensity I_0 of the incident light and the intensity I of the transmitted light of the sample. There are three types to measure the transmittance.

The first is direct transmission measurement, the incident light passes through the sample and the directly transmitted light that travels straight toward the back surface of the sample is metered. In the liquid samples, use a liquid cell and for solid samples, use a solid sample holder for measurement.

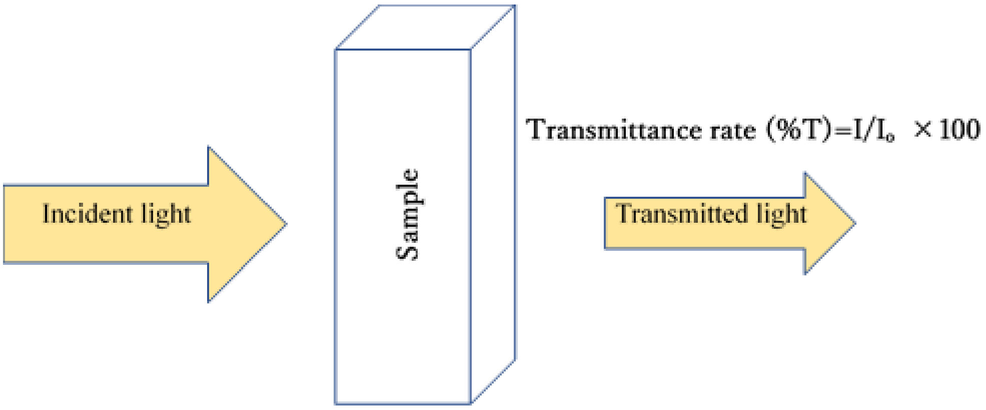

Figure 3.15 Definition of transmittance

The second method is diffusion transmission measurement. The incident light passes through the sample and the diffused transmitted light traveling in various directions is measured on the back surface of the sample. In this measurement, use the integrating sphere accessory and do not measure the transmitted light directly with the light trap, and measure only the diffuse reflected light. The third method is total transmission measurement. Total transmitted light, which is a combination of direct transmitted light and diffused transmitted light, is measured. For the measurement, an integrating sphere accessory is used to measure all transmitted light transmitted through the sample. In this study have used the first measurement method to calculate the transmittance rate.

In the result, absorbance can be calculated from percent transmittance (%T) using this formula:

Absorbance = 2 – log(%T)

Transmittance (T) is the fraction of incident light which is transmitted. In other words, it's the amount of light that "successfully" passes through the substance and comes out the other side. It is defined as T = I/Io, where I = transmitted light ("output") and Io = incident light ("input"). %T is merely (I/Io) x 100. For example, if T = 0.25, then %T = 25%. A %T of 25% would indicate that 25% of the light passed through the sample and emerged on the other side. Absorbance (A) is the flip-side of transmittance and states how much of the light the sample absorbed. It is also referred to as “optical density.” Absorbance is calculated as a logarithmic function of T: A = log10 (1/T) = log10 (Io/I).

3.6 Adhesion evaluation (9)

In this study, the adhesion of the thin film was evaluated using a scratch tester (3K-34B, SHINTO scientific Co., Ltd.). A schematic diagram of the scratch tester is shown in fig. 3.16, and a principal diagram of the scratch test is shown in fig 3.17. In the scratch test, the coating film deforms while being pushed by the moving spherical diamond tip. The indentation load applied increases stepwise or continuously until the coating film cannot follow the deformation of the substrate. As a result, the coating film causes "flaking" or "chipping". At that time, by observing scratch marks with a microscope and observing changes in the coefficient of friction caused by the exposure of the underlying substrate, it is possible to identify the peeled part of the film, estimate the indenter load at that time, and determine the adhesive force. Recent test machines are equipped with a load cell for measuring scratch resistance, and it is also possible to measure the coefficient of friction during a scratch test.

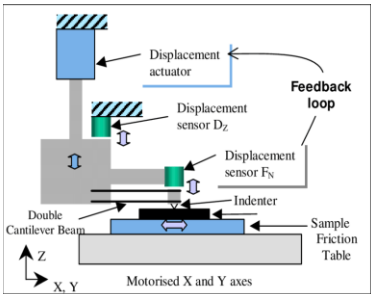

Figure 3.16 A schematic diagram of the scratch tester

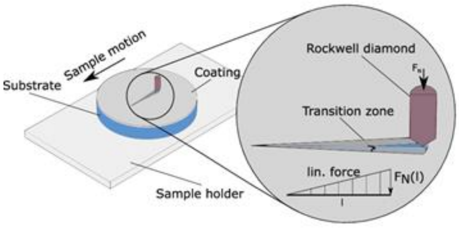

Figure 3.17 principal diagram of the scratch test

References

1) Katsumi Ohno, Akira Kawase, Toshihiro Nakamura: X-ray analysis method, NSPA **(1987).**
2) X. Tang, *DOCTOR OF PHILOSOPHY,* **(2017)**.
3) http://www.sugatsune.co.jp/technology/illumi-l.php.
4) Shogo Nakamura: Surface Physical Characteristics, NSPA **(1982)**.
5) D. Briggs, M.P. Sheer: Surface Analysis, Agne Shofusha **(2001)**.
6) Shimadzu co. catalog (SPM).
7) Y. Sugimoto, P. Pou, M. Abe, P. Jelinek, R. Perez, S. Morita & O. Custance. *Nature,* 446**(2007)**, pp.64-67.

8) C. Bosch Ojeda, F. Sanchez Rojas. *Microchemical Journal,* 106 **(2013)**, pp. 1–16.
9) A. Lassnig, B. Putz, S. Hirn, D.M. Többens, C. Mitterer, M.J. Cordill, *Materials and Design,* 200 **(2021)**, p.109451.
10) Japan Electron Microscopy Society Kanto Branch ed: "Basics and Applications of Scanning Electron Microscopy" Kyoritsu Shuppan **(1983)**.

Chapter 4 Electrical and photo-functional characteristics for copper oxide thin films fabricated by reactive dc magnetron sputtering

4.1 Introduction

Copper oxides (CuO, Cu_2O) are semiconductor materials presently used in many applications, such as oxygen and humidity sensors (1), electrochromic devices and the absorber layer in hetero-junction thin film solar cells (2). Their popularity is attributed to the favorable characteristics, and in particular, the high optical absorption grade is combined with no toxicity and low industrial cost (3). Many studies have shown that, owing to its band gap energy, copper oxide is suitable for use as an absorber in solar energy conversion applications (4). Copper oxides can be both a p-type and an n-type semiconductor, whereby the direct band gap of about 2.1 - 2.6 eV has been measured for Cu_2O (5) and 1.3 - 2.3 eV has been reported for CuO(6), respectively. Since the properties of deposited thin films depend on the fabrication method(7), in extant studies, copper oxide thin films have been prepared by many deposition methods, such as thermal evaporation(8), activated reactive evaporation (9), molecular beam epitaxial growth (10), solution growth(11), sol-gel process(12), electrodeposition(13), rf magnetron sputtering(14) and dc magnetron sputtering(15). However, among all mentioned works the fabrication of coper oxide thin films with a single Cu_2O or CuO phase is still one of the challenges facing of researchers (16).

The purpose of this study is to fabricate copper oxide thin films in both phases of p-type Cu_2O and n-type CuO by using reactive dc magnetron sputtering with helicon plasma. Since the helicon wave provides an electromagnetic power to the plasma in addition to the magnetron power, the discharge plasma can be maintained under a low gas pressure. Those effects give attractive features to fabricated thin films, such as a low power compared with rf magnetron sputtering, appropriate control of the crystalline structure and ability to avoid a substrate heating during a deposition process. On the other hand, in this method the physical characteristics of fabricated films are significantly affected by the fabrication parameters, such as an O_2 gas and Ar gas flow rate, a substrate temperature and a sputtering power (17).

In this study, the influence of a dc sputtering power for the deposited copper oxides thin films was investigated on the structure, electrical and optical properties.

4.2 Experimental and measurement methods

4.2.1 Experimental methods

In this work, copper oxide thin films were prepared by reactive dc magnetron sputtering using helicon plasma. The corning glass (#1737) with a size of 9 × 15 mm and the mirror finishing stainless steel (304ss) with a size of 15 × 15 mm were used as substrates to deposit the films. Before a fabrication process, the surface of substrates was cleaned by Ar plasma for 10 minutes. A turbo molecular pump and a rotary pump were used to achieve a pressure of about 1.2×10^{-5} Pa in the film fabrication chamber. Copper oxide thin films were fabricated under various sputtering powers (10 - 40 W) under an O_2 gas flow rate of 10 sccm and an Ar gas flow rate of 15 sccm. The Cu target with a size of Φ 2 inches and purity of 99.99 % was used. Because the distance between the substrate and the target was 500 mm by the effect of long throw sputtering using a helicon plasma cathode, the substrate temperature was independently kept at constant 300 ºC through a fabrication process. Since the deposition rate depends on the sputtering power, in order to achieve 200 nm film thickness, the sputtering power corresponding to the deposition rate was required as shown in fig 4.1. According to the graph depicted in fig 1, 250 minutes was required to achieve 200 nm thickness under 10 W in a sputtering power, while about 90 minutes was needed to obtain the same film thickness at 40 W. In this experiment, it was suggested that the ambient gas pressure affected the film characteristics and so the ambient gas pressure was kept at 0.045 Pa.

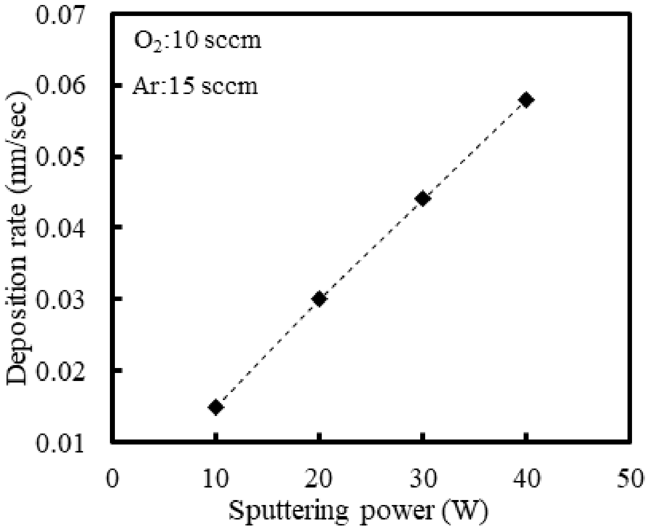

Figure 4.1 Deposition rate of copper oxide films fabricated under various sputtering

4.2.2 Measurement methods

4.2.2.1 Crystal structure measurement

The crystal structure of the thin film was measured by thin film X-ray diffraction (XRD: High quality XG M18XCE, MAC Science. Co., Ltd.) using CuKα rays (0.154056 nm) at an incident angle of 0.3 degrees.

4.2.2.2 Surface morphology and cross-sectional image

The surface morphology and roughness were observed by using an atomic force microscope (AFM: SPM-9500, Shimadzu Corporation). The tapping mode was used, and the measurement conditions were a scanning range of 1μm and a scanning speed of 2 Hz.

4.2.2.3 Composition and chemical bond state

The composition and chemical bond state were analyzed by X-ray photoelectron spectroscopy (XPS: ESCAK1-S, Shimadzu Corporation) using MgKα rays (1486.6 eV). The binding energy was calibrated with the Ag3d5 / 2 catalog value of 368.3eV. The prepared copper oxides thin film was once exposed to the atmosphere and then introduced into an X-ray photoelectron spectrometer, and the degree of vacuum at the time of measurement was set to 5×10^{-7} Pa or less. In the measurement, Ar + ion sputtering (2keV, $18\mu A / cm^2$, 30sec) was performed to remove carbon contamination on the surface, but it was confirmed that selective sputtering of O can be ignored under these conditions.

4.2.2.4 Calculation optical band gap

UV-Vis spectrophotometer (UV-2550, Shimadzu Corp.) device have used to determine the optical band gap in wavelength from 300 nm to 900 nm. Because of the crystallinity and higher transparency, the copper oxide films are suitable for optical analysis from which the absorption coefficient and energy band gap may be determined. The conversion of Cu_2O into CuO can also be shown by the determination of the optical band gap. The best linear relationship is obtained by plotting α^2 against hν, based on Eq (4.1) below.

$$\alpha h\nu = A\,(h\nu - E_g)^{n/2} \qquad \ldots\ldots\ldots (4.1)$$

where α is absorption coefficient, A a constant (independent from ν) and n the exponent that depends upon the quantum selection rules for the particular material. The photon energy (hν) for y-axis can be calculated using Eq (4.2).

$$E = h\nu = hc/\lambda \qquad \ldots\ldots\ldots\ldots (4.2)$$

where h is Plank's constant (6.626×10^{-34}), c is speed of light (3×10^{8}) and λ is the wavelength.

4.2.2.5 Calculation of electrical properties

A two-point resistance measurement is the simplest method to assess the conductivity of a sample. A test current is forced through the sample and the multimeter measures the voltage drop between the two terminals. The problem of this method is that the resistance of the wires and the contact resistance at the terminals are included in this measurement. Therefore, to assess the resistance and obtain accuracy values of a resistivity, mobility and carrier concentration of thin film, it is preferable to rely on a four-point resistance measurement as in a Hall Effect measurement system (Ecopia Co. Ltd) as explained below.

The resistivity of a thin film can be performed by means of four collinear contact points. At first, a known DC current I is applied between the two outer probes. Then, the voltage V between the two inner probes is measured. Finally, the resistivity is calculated from

$$\rho = F\,V/\,I \ldots\ldots\ldots\ldots (4.3)$$

where F [m] is a geometric correction factor depending on the geometric arrangement of the probes, the thickness of the sample, the finite size of the sample, and the position of the probes with respect to the sample edge (20). The main advantage of a four-point resistance measurement is the elimination of contact resistances at the positions of the probes, considering that voltage probes have a high electrical impedance.

4.3 Film characterization

4.3.1 X-ray diffraction analysis

Figure 4.2 showed the X-ray patterns of copper oxide thin films fabricated at sputtering powers of 10, 20, 30 and 40 W. The film deposited at 10 W showed a single-phase CuO, with strong peaks at $2\theta = 35.55°$ and $38.72°$ corresponding to (-111) and (111) orientation, respectively. As the sputtering power was increased to 20 W, the intensity of CuO peaks decreased, and Cu_2O peaks emerged at 2θ = 29.55°, 36.41°, 42.29° and 73.52°, corresponding to (110), (111), (200) and (311) orientation, respectively. The sputtering rate increased with increase in the sputtering power, as shown in fig 4.1. This indicated that the number of sputtered Cu atoms determined the structure of the fabricated film, i.e., the ratios of O_2 molecules to copper atoms determined the stability of the Cu_2O and CuO phase formation (21). The CuO type of the copper oxide was obtained at 10 W. The Cu_2O type with CuO peaks was observed at 20 W, because the amount of Cu atoms was insufficient to change the structure from CuO to Cu_2O (19). Therefore, by increasing the sputtering power to 30 W, the film structure transformed into a single phase of Cu_2O with the (111) orientation. As the sputtering power was increased to 40 W, the Cu peak corresponding to the (111) orientation appeared alongside the Cu_2O peaks. The results of this work showed that the single phase of CuO could be obtained under a sputtering power of 10 W, while a single phase of Cu_2O was obtained at 30 W. It is known that the control of film structures is difficult on a few formation methods by film deposition exposed in plasma. In this work, the deposition method using the helicon plasma had a main role to give tow single phases by only changing sputtering powers.

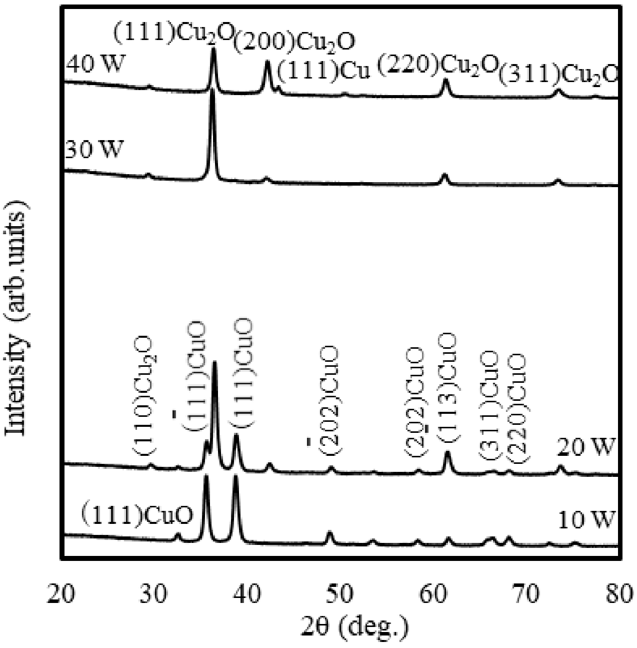

Figure 4.2 XRD patterns of copper oxide films fabricated under various sputtering powers

4.3.2 Surface morphology

Figure 4.3 showed the morphology of copper oxides thin films observed by AFM on a scale of 5 × 5 μm^2 under various sputtering powers. The images revealed a homogenous surface with significant change for XRD results. The XRD patterns with the fine structure of 10 W and 20 W in a sputtering power showed large roughness values of 16.6 nm and 14.7 nm, respectively. While, the roughness of 30 W shows noticeable decrease of 8.4 nm and the roughness has increased again at deposition power of 40 W, where it became 10.4 nm. That is mean, the surface morphologies corresponded with the change of copper oxide structures as shown XRD result in the fig 4.2, where the roughness increase at the films that have a high crystal structure and multiphases structure (16).

10W:16.6nm

20W:14.7nm

30W:8.4nm

40W:6.2nm

Figure 4.3 Surface morphology and surface roughness (Ra) for copper oxide films fabricated under various sputtering powers.

4.3.3 Chemical composition

Figure 4.4 showed the chemical state for an O1s orbit of copper oxide thin films under various sputtering powers. The binding energy was calibrated with C1s at 284.6 eV. Because the difference between the binding energy of CuO and Cu_2O was 0.9 eV in O1s, the XPS spectrum separation process was required to elucidate the chemical state. The O1s spectrum (a full line as the origin) was fitted by two curves attributed to CuO (a broken line of 529.6 eV) and Cu_2O (a dotted line of 530.5 eV). The spectrum of 10 W in a sputtering power consisted of almost CuO, while by increasing the sputtering power to 30 W and 40 W, the original peak was fully shifted to the binding energy of 530.5 eV, which refers to Cu_2O. The CuO peaks of 30 W and 40W appeared by O_2 absorption to the Cu_2O surface. These results were aligned with the XRD investigation including 20 W. It was confirmed that the sputtering power was the main factor controlling the copper oxide structure.

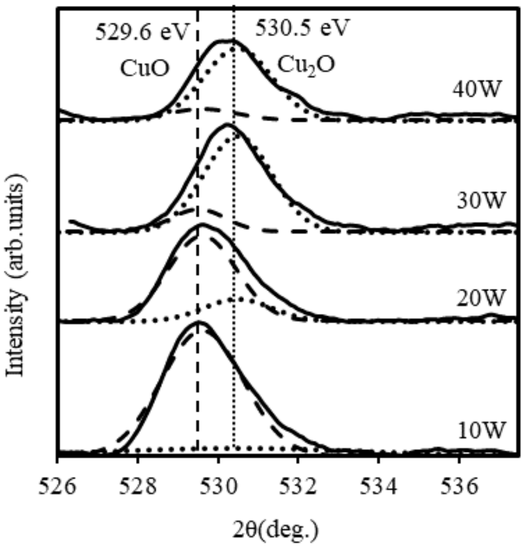

Figure 4.4 XPS O1s spectra of copper oxide films fabricated under various sputtering

4.3.4 Semiconductor property

Figure 4.5 showed the resistivity and mobility of the copper oxide films fabricated under various sputtering powers, which were measured by using the Hall Effect measurement system. The resistivity and mobility of fabricated films decreased as the sputtering power increased.

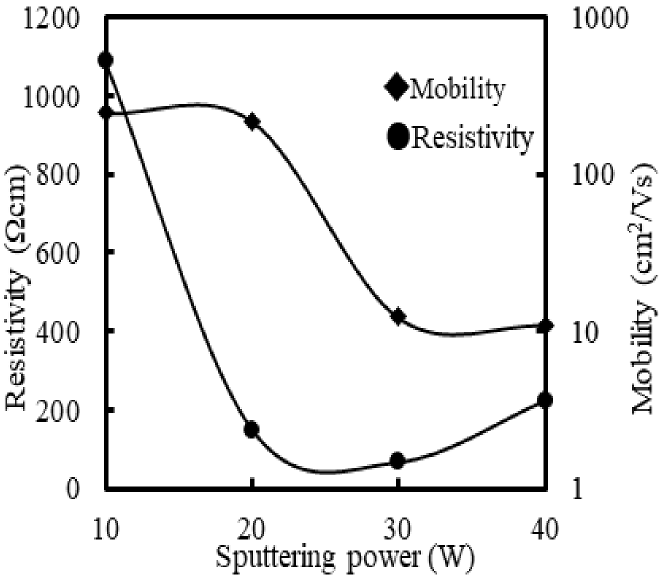

Figure 4.5 Resistivity and mobility for copper oxide films fabricated under various sputtering powers.

Specifically, the resistivity decreased from its maximum value of 1.09 k.Ω.cm at the sputtering power of 10 W to 0.149 k.Ω.cm, at 20 W due to the increase in the number of

Cu atoms. A slight increase in the resistivity was noted at the sputtering power of 40 W and was attributed to the increase in surface roughness, as shown in fig 4.3.

The mobility was decreased from its maximum value by increasing a sputtering power, due to the low carrier concentration in the CuO thin film comparing with the Cu_2O thin film as shown in fig 4.6. In fig 4.6 the films fabricated at the sputtering power of 10 W and 20 W showed an n-type at a CuO phase with the low carrier concentration, while the films turned to a p-type of Cu_2O at the sputtering power of 30 W and 40 W. These results were consistent with the CuO and Cu_2O characteristics[21)]. The high carrier concentration that was observed at 30 W was attributed to the stoichiometric Cu_2O structure comprising of a suitable number of Cu and O atoms.

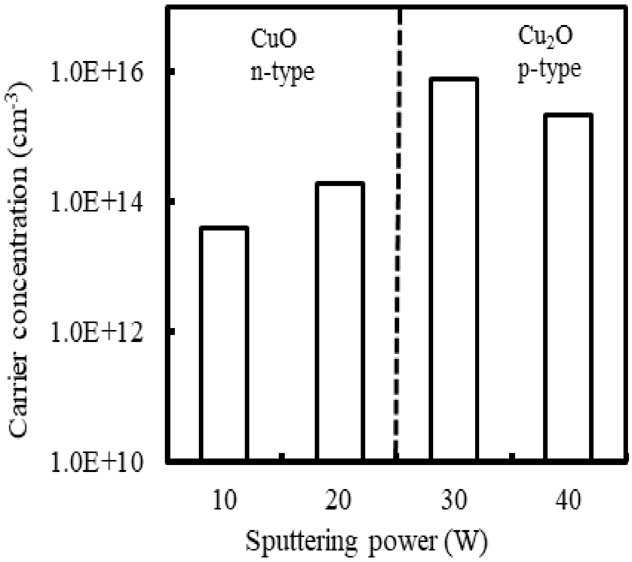

Figure 4.6 Carrier concentration for copper oxide films fabricated under various sputtering

4.3.5 Optical band gap

Figure 4.7 showed the optical band gap of copper oxides under various sputtering powers, which was determined by using the UV-VIS absorbance spectrum and applying Tauc equation Eq. 1(22), where *Eg* was the optical band gap, *v* was the photon velocity, and *h* was the Planck's constant.

$$(\alpha hv) = \exp\,(hv - Eg)^{1/2} \ldots\ldots\ldots\ldots\ldots\ldots\ldots\ldots (1)$$

Copper oxide band gaps were measured at 1.7 eV, 2.0 eV, 2.5 eV and 2.55 eV at 10 W, 20 W, 30 W and 40 W, respectively. As obviousness from these results, the fabricated copper oxides with a CuO phase showed lower band gaps at the sputtering power of 10 W and 20 W, while a Cu_2O phase showed higher band gaps at a sputtering power of 30 W and 40 W. Generally, it is known that the CuO phase corresponds to the n-type with the band gap of around 2.0 eV, whereas the Cu_2O phase corresponds to the p-type with around 2.5 eV band gap (6). The optical band gap results were also consistent with the results obtained by the XRD and Hall Effect measurements.

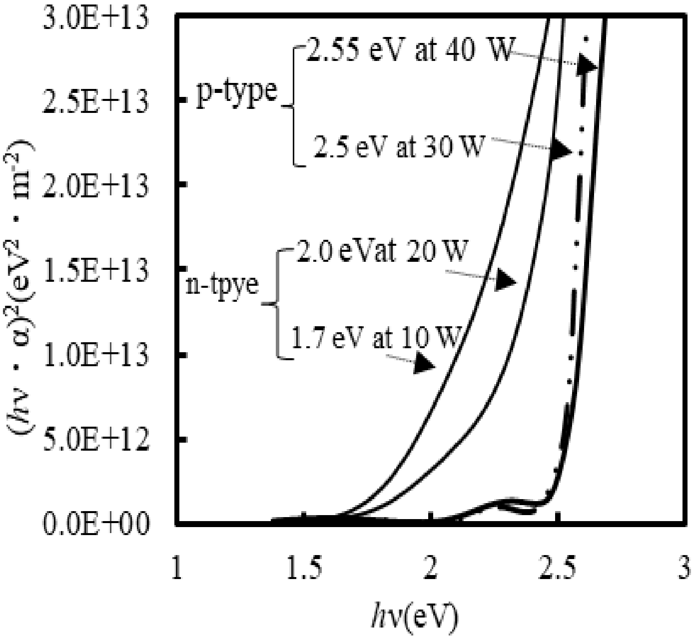

Figure 4.7 Optical band gap for copper oxide films fabricated under various sputtering

4.4 Conclusions

In this work, the copper oxide thin films prepared by reactive dc magnetron sputtering using helicon plasma were discussed under various sputtering powers. The XRD and XPS results showed that the sputtering power was the main factor determining the film structure of copper oxides. A single phase CuO under the sputtering power of 10 W and a single phase Cu_2O under 30 W were obtained, respectively. In prior works hardly reported such results. The Hall Effect measurements and the calculated optical band gap values indicated that this film formation method could be used to fabricate precisely copper oxides with different characteristics.

REFFRENCES

(1) S.P. Sharma, J. Vac. *Sci. Technol*, 16 **(1979)**, p. 1557.

(2) T. Minami, H. Tanaka, T. Shimakawa, J. Miyata and H. Sato. *Jpn. J. Appl. Phys*, 43 **(2004)**, p. 917.

(3) B. Balamurugan and B.R. Mehta. *Thin Solid Films,* 396 **(2001)**, p. 90.

(4) A.A. Ogwu, E. Bouerel, O. Ademosu, S. Moh, E. Crossan and F. Placido. *Journal of Physics*, 38 **(2005)** (2), pp. 266-271.

(5) F.K. Mugwang'a, P.K. Karimi, W.K. Njoroge, O. Omayio and S.M. Waita. *Int. J. Thin Film Sci*, 2 **(2013)** (1), pp. 15-24.

(6) J.F. Pierson, A. Thobor-Keck and A. Billard. *Appl. Surf. Sci*, 210 **(2003)**, pp. 359-367.

(7) S. Zhang and N. Ali, *Nanocomposite thin films and coating, Imperial College Press, London*, UK **(2007)**.

(8) L.S. Huang, S.G. Yang, T. Li, B.X. Gu, Y.W. Du, Y.N. Lu and S.Z. Shi. *J. Cryst. Growth,* 260 **(2004)**, p. 130.

(9) B. Balamurugan, B.R. Mehta, D.K. Avasthi, F. Singh, A.K. Arora, M. Rajalakshmi, G. Raghavan, A.K. Tyagi and S.M. Shivaprasad. *J. Appl. Phys,* 92 **(2002)**, p. 3304.

(10) I.L. Yubinetsky, S. Thevulhasan, D.E. Mc Cready and D.R. Baer. *J. Appl. Phys*, 94 **(2003)**, p. 7926.

(11) C.A.N. Fernando and S.K. Wetthasinghe, *Sol. Energy Mater. Sol. Cells,* 63 **(2000)**, p. 299.

(12) H. Nagai, T. Suzuki, H. Hara, C. Mochizuki, I. Takano, T. Honda and M. Sato. *Chemical Sol*, **(2012)**, p.137.

(13) J. Morales, L. Sanchez, S. Bijani, L. Martizez, M. Gabas and J.R. Ramos-Barrado, Electrochem. *Solid-State Lett*, 8 **(2005)** (3), p. 159.

(14) A. Parretta, M.K. Jayaraj, A.D. Nocera, S. Loreti, L. Quercia and A. Agati. *Phys. Status Solidi A*, 155 **(1996)**, p. 399.

(15) S. Ghosh, D.K. Avasthi, P. Shah, V. Ganesan, A. Gupta, D. Sarangi, R. Bhattacharya and W. *Assmann Vacuum,* 57 **(2000)**, p. 377.

(16) Reddy, M. & Sreedhar, A. & Uthanna, S. *Indian Journal of Physics,*4 **(2012),** p. 86.

(17) Haider A. Shukur, Mitsunobu Sato, Isao Nakamura, and Ichiro Takano, *Advances in Materials Science and Engineering*, 7 **(2012)**, p.2012

(18) C. R Sekhar. *Solar Energy Mater,* 68 **(2001)**, p. 307.

(19) A. Neamen, Donald, *semiconductor physics & devices, second edition* **(1997)**.

(20) I. Miccoli, F. Edler, H. Pfnür, and C. Tegenkamp. *Journal of Physics: Condensed Matter,* 27 **(2015)**, p. 22.

(21) A.S. Reddy, G.V. Rao, S. Uthanna and P.S. Reddy. *Physica B*, 370 **(2005)**, p. 29.

(22) Brian D. Viezbicke, Shane Patel, Benjamin E. Davis and Dunbar P. Birnie. *Physica Status Solidi B*, 252 **(2015)**, pp. 1700-1710.

Chapter 5 Crystal structure and semiconductors properties of copper oxides thin films at low temperature

5.1 Introduction

Cuprous oxide (Cu_2O) and cupric oxide (CuO) are a promising nontoxic material, found suitable for applications in electrochromic devices (1) and oxygen and humidity sensors (2). They are an attractive absorber layer for hetero junction solar cells because of a direct band gap of 2.0 eV and 1.5 eV respectively (3). In recent years much attention has been focused on the growth of polycrystalline heterojunctions of TiO2/Cu_2O, ZnO/Cu_2O, NiO/CuO and CuO/Cu_2O for solar cell application (4, 5). All these transparent conducting oxides have electronic structure similar to Cu_2O and CuO except the suitable band gaps that correspond with these materials. Furthermore, the increasing demand for foldable and wearable electronics has led to a need for flexible optoelectronic components. The nature of the p-type conduction of Cu_2O and n-type conduction of CuO is originated from the presence of copper vacancies, which form acceptor and doner level above the valance band. The physical properties of the films depend mainly on the deposition method and the parameters maintained during the preparation. Many researchers attempted in the preparation of Cu_2O and CuO films by various deposition techniques such as thermal oxidation (3), vacuum evaporation (2,6), activated reactive evaporation (7), molecular beam epitaxy (8), dc and rf sputtering (1,9–14), solution growth (15), sol–gel (16) and electrodeposition (17–21). Among these, helicon plasma dc reactive magnetron sputtering is one of the best practiced techniques, because of the advantages of sputtering from pure metallic target in the presence of different reactive gases with high deposition rates, uniformity on large area substrates and easy control over the chemical composition of the deposited films. Hence, an attempt was made in the deposition of p-type Cu_2O and n-type CuO films by helicon plasma dc reactive magnetron sputtering from pure metallic target of copper in the presence of argon and oxygen gases under different substrate temperatures and studied the effect of substrate temperature on the crystallographic structure, electrical and optical properties of the deposited films.

5.2 Experimental and measurement methods

5.2.1 Experimental methods

In this work, copper oxide thin films were prepared by reactive dc magnetron sputtering using helicon plasma. The corning glass (#1737) with a size of 9 × 15 mm and the mirror finishing stainless steel (304ss) with a size of 15 × 15 mm were used as substrates to deposit the films. Before a fabrication process, the surface of substrates was cleaned by

Ar plasma for 10 minutes. A turbo molecular pump and a rotary pump were used to achieve a pressure of about 1.2×10^{-6} Pa in the film fabrication chamber. Copper oxide thin films were fabricated under various substrates temperature from room temperature (RT) to 300 °C under an O_2 gas flow rate of 10 sccm and an Ar gas flow rate of 15 sccm. The Cu target with a size of Φ 2 inches and purity of 99.99 % was used. Science the deposition rate depended on the sputtering power was measured by using a quartz-type thickness tester in the film formation chamber, the formation time to obtain 200 nm in a film thickness was calculated about the dc sputtering power 10 W and 30 W. The required deposition time was 208 min and 73 min at 10 W and 30 W respectively. The reason of choosing the 10 W and 30 W in a dc sputtering power had been described in our previous study at chapter 4 that shows the formation of n-type CuO, p-type Cu_2O and both phases in different Cu sputtering rates (22).

5.2.2 Measurement methods

5.2.2.1 Crystal structure measurement

The crystal structure of the thin film was measured by thin film X-ray diffraction (XRD: High quality XG M18XCE, MAC Science. Co., Ltd.) using CuKα rays (0.154056 nm) at an incident angle of 0.3 degrees.

5.2.2.2 Evaluation optical properties

The crystallinity and higher transparency, the copper oxide films are suitable for optical analysis from which the absorption coefficient and energy band gap may be determined. UV-Vis spectrophotometer (UV-2550, Shimadzu Corp.) device have used to evaluate the optical absorbance, transmittance and optical band gap. The absorption and transmittance have evaluated under wave length from 400 nm to 800 nm. The absorption and the transmittance have calculated by using (Eq 5.1).

$$\alpha = 1/d \times \ln(1/T) \text{ ………… } (5.1)$$

Where α, T and d are the absorption coefficient, the transmittance and the thickness of films, respectively.

The optical band gap has determined in the wavelength from 300 nm to 900 nm. The conversion of Cu_2O into CuO can also be shown by the determination of the optical band gap. The best linear relationship is obtained by plotting α^2 against hν, based on Eq (5.2) below.

$$\alpha h\nu = A\,(h\nu - Eg)^{n/2} \qquad \text{......... (5.2)}$$

where α is absorption coefficient, A a constant (independent from ν) and n the exponent that depends upon the quantum selection rules for the particular material. The photon energy (hν) for y-axis can be calculated using Eq (5.3).

$$E = h\nu = hc/\lambda \qquad \text{.......... (5.3)}$$

where h is Plank's constant (6.626×10^{-34}), c is speed of light (3×10^{8}) and λ is the wavelength.

5.2.2.3 Calculation of electrical properties

A two-point resistance measurement is the simplest method to assess the conductivity of a sample. A test current is forced through the sample and the multimeter measures the voltage drop between the two terminals. The problem of this method is that the resistance of the wires and the contact resistance at the terminals are included in this measurement. Therefore, to assess the resistance and obtain accuracy values of a resistivity, mobility and carrier concentration of thin film, it is preferable to rely on a four-point resistance measurement as in a hall effect measurement system (Ecopia Co. Ltd) as explained below.

The resistivity of a thin film can be performed by means of four collinear contact points. At first, a known DC current I is applied between the two outer probes. Then, the voltage V between the two inner probes is measured. Finally, the resistivity (ρ) is calculated from the Eq (5.4)

$$\rho = F\,V/I \text{ .... (5.4)}$$

where F [m] is a geometric correction factor depending on the geometric arrangement of the probes, the thickness of the sample, the finite size of the sample, and the position of the probes with respect to the sample edge (18). The main advantage of a four-point resistance measurement is the elimination of contact resistances at the positions of the probes, considering that voltage probes have a high electrical impedance.

5.3 Film characterization

5.3.1 X-ray diffraction analysis

The thin films fabricated by helicon plasma sputtering were smooth, well adherent and optically transparent. Figure 5.1 shows the X-ray diffraction patterns of CuO thin films deposited at (RT), 45, 100, and 300 °C substrate temperatures. For temperatures 300°C, the peaks appearing in the main diffraction spectrum of 35.55 and 38.72 indexed to (11-1) and (111), and the others weak peaks indicating the polycrystalline nature of the CuO thin film. When the substrate temperature decreased under 300°C, the intensity of (11-1), (111) planes decreased and the others peaks had disappeared gradually evidently up to 45°C.

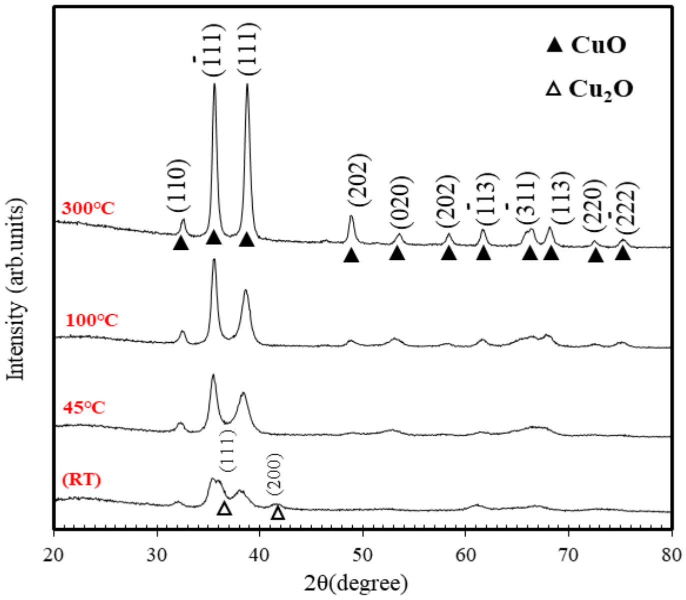

Figure 5.1 XRD characterization of CuO thin films fabricated at substrate temperature from (RT) to 300°C

The film fabricated at (RT) shows mixture phases of CuO/Cu_2O, where the peaks that related to Cu_2O thin film of (111), (200) at 36.42°, 42.92° have demonstrated respectively. Figure 5.2 shows the films structure of the Cu_2O that formed at 30W and substrate temperature between (RT) and 300°C. The film structure at 100°C and 300°C showed clear phase of Cu_2O with high peak of main plane (111) at 36.42°, and another weak peaks of (110), (200), (220) and (311) at 29.55°, 42.29°, 61.34° and 73.52° respectively. For the others temperatures no noticeable change in the main peak (111) have demonstrated, and others peaks have showed high peak compared with the film formed at 100°C and 300°C.

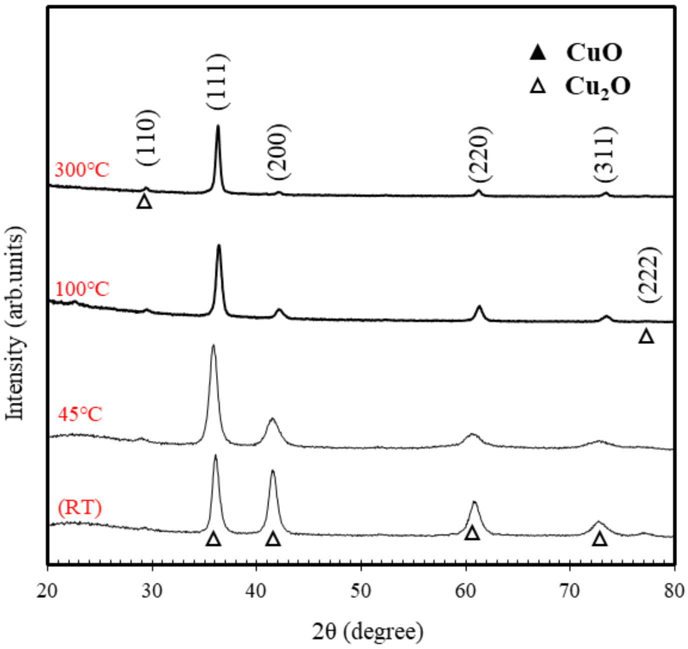

Figure 5.2 XRD characterization of Cu_2O thin films fabricated at substrate temperature from (RT) to 300°C

5.3.2 Optical properties

5.3.2.1 Optical Absorbance

Figure 5.3 shows the UV–Vis absorption spectra of CuO under various substrate temperature. The absorbance increases with increasing the substrate temperature respectively. The reason of the low absorbance at the low substrate temperature (RT), due to the transparent color for the film because the presence Cu_2O along with CuO in the film as shown in fig 5.1. When the film converted to single phase CuO at 45°C, the color convert from light black to dark black that is led to increase the absorbance with increase the substrate temperature. The higher absorbance showed at 300°C due to the crystal structure composition (23), where all the orientations peaks are presences in the film as shown in XRD result at figure 5.1.

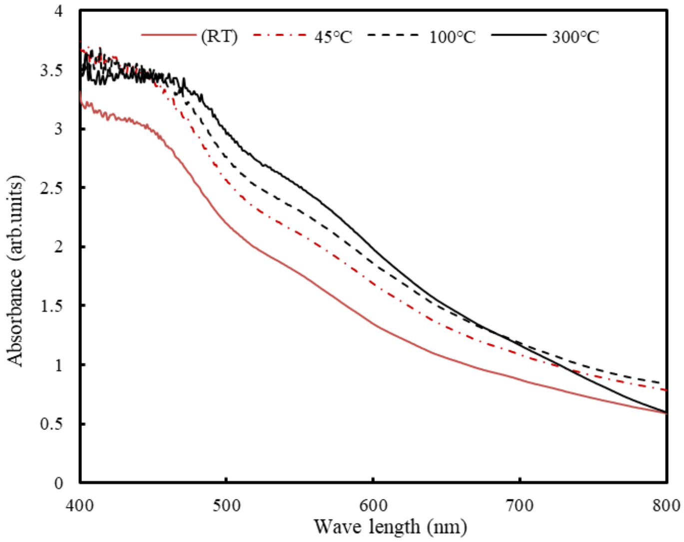

Figure 5.3 Optical absorbance of CuO thin films fabricated at substrate temperature from (RT) to 300°C

The absorbance spectra in the visible region of the deposited Cu_2O thin films synthetized at different deposition temperature are displayed in figure 5.4. High absorption had demonstrated at the films formed at low temperature of (RT) and 45°C, and low absorption at the high temperatures 100°C and 300°C. The high absorption at low temperature due to multi orientation at the film formed at low temperature (23), as shown in the XRD result fig 5.2.

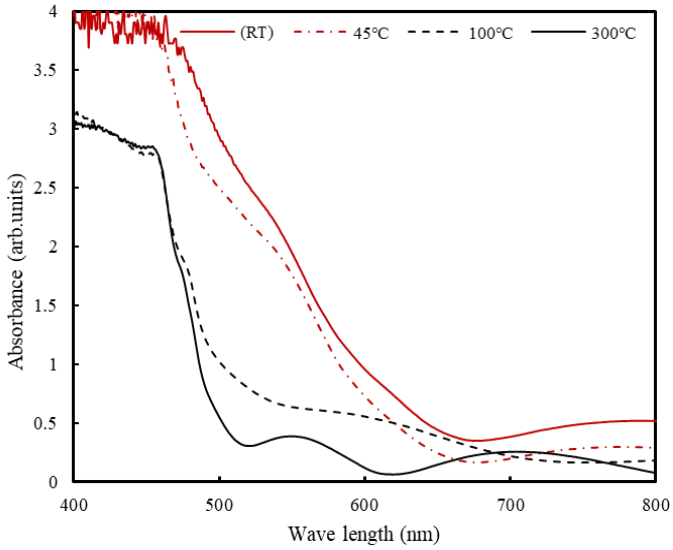

Figure 5.4 Optical absorbance of Cu_2O thin films fabricated at substrate temperature from (RT) to 300°C

5.3.2.2 Transmittance

Figure 5.5 shows the transmittance for the CuO thin film fabricated at various temperature. The film formed at substrate temperature of (RT) had demonstrated high transmittance due to the presence of Cu_2O along with CuO as explained previously at absorption results. Where, the color of the film was light black that led to make the film more transparent. In other hand, the transmittance decreased with increased the temperature. A relatively higher transmittance value for the thin film deposited at low temperatures maybe attributed to less scattering due to the decrease in the degree of irregularity in the grain size distribution (24). This is due to the light interference at the interface between the CuO thin film and the substrate, indicating that the surfaces of the CuO thin films deposited on substrates are smooth (25).

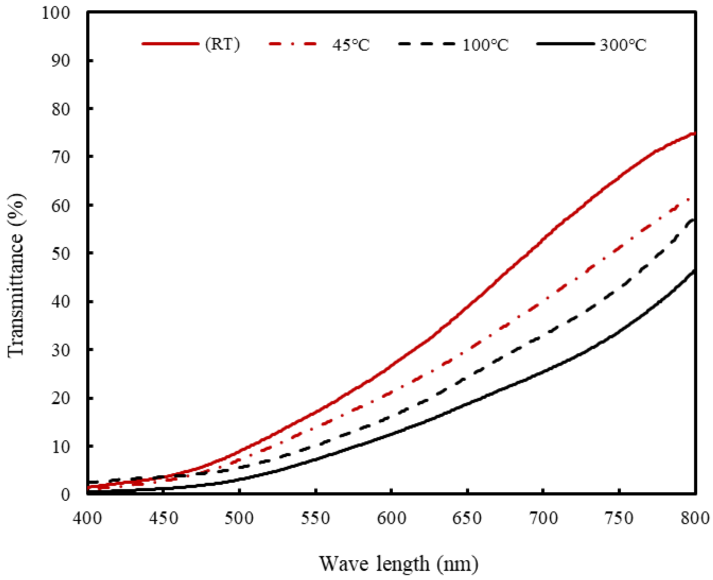

Figure 5.5 Transmittance of CuO thin films fabricated at substrate temperature from (RT) to 300°C

The transmittance of Cu_2O thin films at various substrate temperature from (RT) to 300°C have showed in figure 5.6. The homogeneous crystal structure for the films formed at 100 °C, 300 °C led to make these films have high transmittance (26), and the films fabricated at low substrate temperature showed low transmittance as shown in figure 5.6. These results showed that the transmittance results for the Cu_2O and CuO are compatible with the absorbance results.

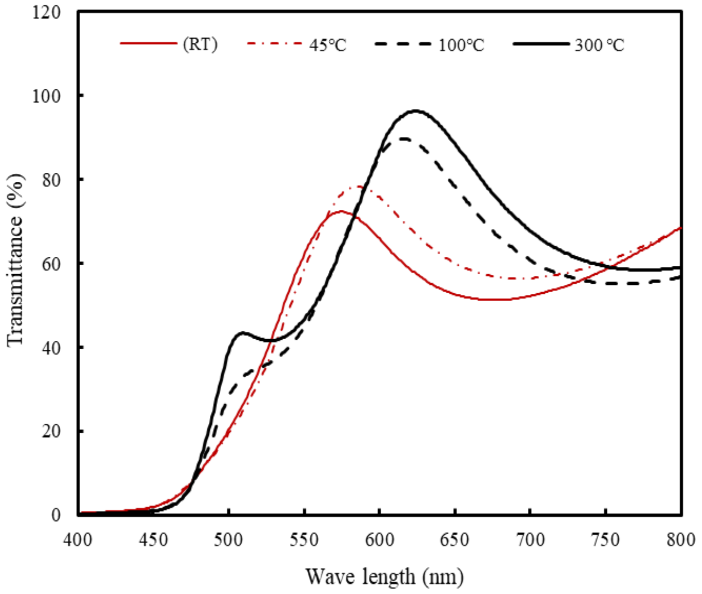

Figure 5.6 Transmittance of Cu_2O thin films fabricated at substrate temperature from (RT) to 300°C

5.3.2.3 Bandgap

Figure 5.7 shows the plots of $(\alpha h\nu)^{1/2}$ versus photon energy ($h\nu$) of the films fabricated at different substrate temperatures between (RT)-300°C for CuO thin films formed at 10W.

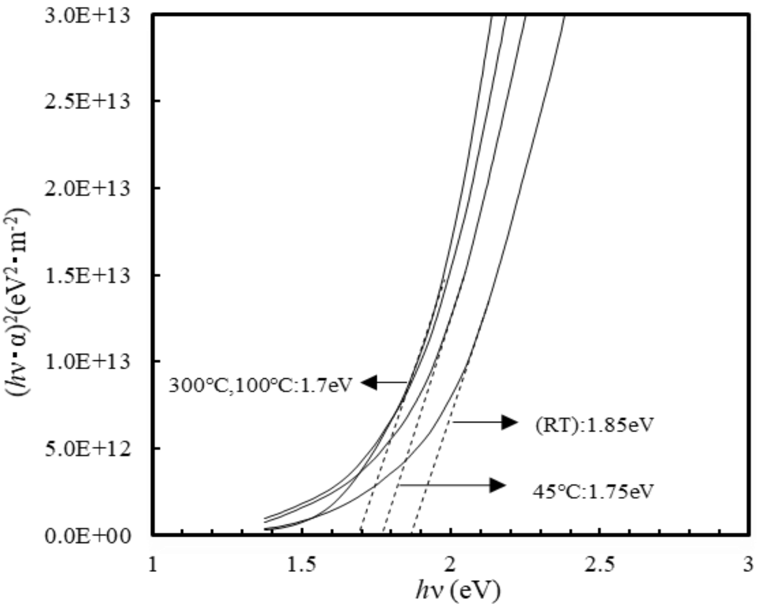

Figure 5.7 Optical bandgap of CuO thin films fabricated at substrate temperature from (RT) to 300°C

The optical band gap of the films was evaluated by extrapolating the linear portion of the above plots to $\alpha = 0$. The highest band gap value of 1.85eV was obtained at substrate temperature of (RT), due to the presence of Cu_2O along with CuO thin film as shown in the XRD result figure 5.1. Increasing the temperature to the 45°C led to decrease the band gap to the 1.75eV, because the films at this temperature became single phase of CuO thin film. The film formed at 300°C and 100°C shows a bit decreasing in the band gap, this decreasing may be attributed to an increase in the packing density and the crystallinity in the film (27).

Figure 5.8 also shows the plots of $(\alpha h\nu)^{1/2}$ versus photon energy ($h\nu$) of the films formed at different substrate temperatures from (RT) to 300°C for Cu_2O thin films formed at 30W. The optical band gap of the films was evaluated by extrapolating the linear portion of the above plots to $\alpha = 0$. The result of this section is also compatible with XRD results figure 5.2, where the band gab at the high substrate temperatures had showed high values between (2.45-2.5) eV due to the homogeneously in the crystal structure at the high substrate temperature. As for the low substrate temperature of (RT) and 45°C, the band gaps were about 2.1eV.

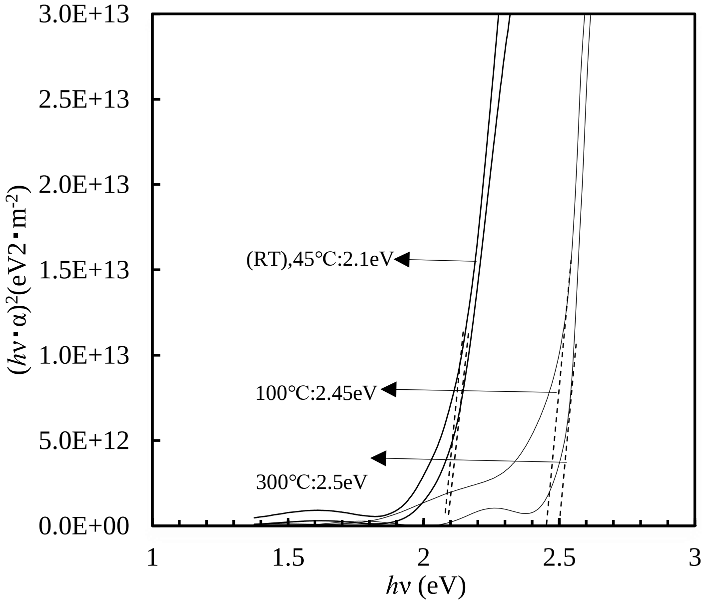

Figure 5.8 Optical bandgap of Cu_2O thin films fabricated at substrate temperature from (RT) to 300°C

5.3.3 Electrical properties

The resistivity and mobility of CuO thin films that formed at 10W and substrate temperature from (RT) to 300°C have showed at figure 5.9. The film fabricated at (RT) showed low electrical resistivity 30 Ω.cm, mobility 9.2×10^{2} cm^{2}/Vs and carrier concentration $9.3\times10^{-16}cm^{-3}$. The low electrical resistivity at this temperature maybe due to the presence of Cu_2O phase along with CuO phase as shown in figure 5.1 for the XRD results. In another meaning, there are excess copper content in the film compared with others films. Whereas, the substrate temperature of 45°C showed high electrical resistivity about 8.4×10^{2} Ω.cm due excess oxygen content in the films, that is led to change the film characterization to CuO characterization. Increasing the substrate temperature to 300°C led to, decrease the electrical resistivity from 8.4×10^{2} Ω.cm to 10.1 Ω.cm, increase the mobility from 10.3 cm^{2}/Vs to 2.2×10^{2} cm^{2}/Vs, and increase the carrier concentration from 2.6×10^{-14} cm^{-3} to 1.6×10^{-16} cm^{-3}. The reason for decrease the electrical resistivity

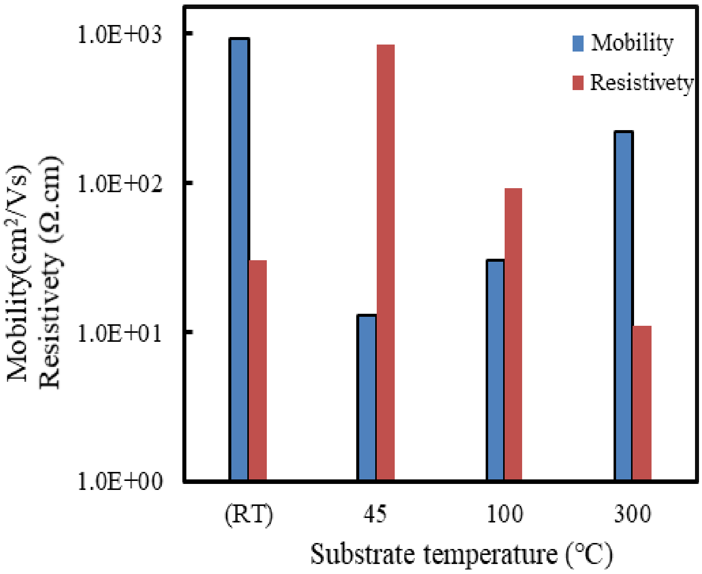

Figure 5.9 Resistivity and mobility of CuO thin films fabricated at substrate temperature from (RT) to 300°C

with increase the substrate temperature is improve the crystal structure (28). In this part, influence of the substrate temperature on the electrical properties of CuO films have investigated.

Evaluation of the resistivity and mobility for Cu_2O thin film at 30W and substrate temperature between (RT) and 300°C have demonstrated by fig 5.10. The electrical resistivity of the films decreased from 1.5×10^{3} Ω cm to 20.1 Ω cm with increase the substrate temperature from (RT) to 300°C, maybe due to the improvement in the crystallinity of the films (28) as in XRD results at figure 5.2. The lower electrical resistivity of 20.1 Ω cm have exhibited at the films formed at the higher substrate temperature of

300°C. Hall mobility of the films increased from 20.5 cm^2 /Vs to 9.1×10^2 cm^2 /Vs with increasing the substrate temperature from (RT) to 300°C. The similar behavior of increase the Hall mobility and decrease the electrical resistivity with increase the substrate temperature was also observed in rf sputtered Cu_2O films (29). The carrier concentration of the films increases from 9.4×10^{11} cm^{-3} to 6.3×10^{15} cm^{-3} with increase of substrate temperature from (RT) to 300°C. The increase of carrier concentration is over compensated by the larger increase of carrier mobility; therefore, the resistivity decreases with increasing substrate temperature. These results have verified that the substrate temperature has highly influence on the electrical properties for the Cu_2O films.

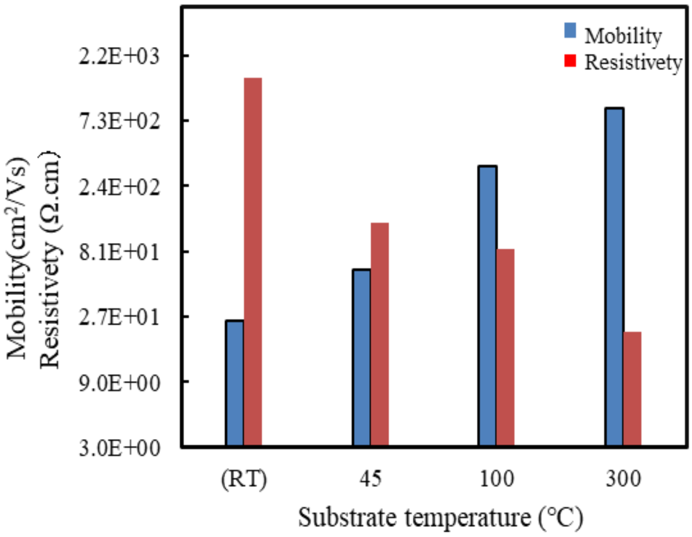

Figure 5.10 Resistivity and mobility of Cu_2O thin films fabricated at substrate temperature from (RT) to 300°C

5.4 CONCLUSIONS

Using helicon plasma dc reactive magnetron sputtering, the copper oxides Cu_2O, CuO thin films have fabricated at various substrates temperature from RT to 300°C. High crystal structure of Cu_2O have obtained for all substrate temperatures. Whereas, the crystal structure of CuO thin films have decreased with decrease the substrate temperature, where the crystal structure at RT showed mixture structure of CuO/Cu_2O.

Increasing the substrate temperature led to increase the absorbance and decrease the transmittance in the results of CuO thin film, and these results were confirmed with the XRD results. On the contrary in the Cu_2O results, the absorbance has decreased with increase the substrate temperature and the transmittance has increased. For all films, the electrical results at low substrate temperature have closely values compare with the results at high substrate temperature. In the summary of this study, fabricate copper oxides CuO, Cu_2O at low substrate temperature with electrical and optical properties close to the results fabricated at high substrate temperature.

REFFRENCESE

(1) T. J. Richardson, J. L. Slack, and M. D. Rubin. *Electrochim. Acta*, 46**(2001)**, p. 2281.
(2) S. P. Sharma, J. Vac. *Sci. Technol*, 16**(1979)**, p. 1557.
(3)Dhanya.S.Murali, Shailendra.Kumar, R.J.Choudhary, Avinash.D. Wadikar, Mahaveer K. Jain, and A. Subrahmanyam, *AIP ADVANCES*, 5**(2015)**, p. 047143.
(4) Sawicka-Chudy, M. Sibinski, R.Pawełek, G.Wisz, B. Cieniek, P. Potera, P. Szczepan, S. Adamiak, M. Cholewa, and Głowa. *AIP Advances,* 9**(2019)**, p. 055206.
(5) E.F. Abo Zeida, A.M. Nassar, M.A. Husseind, M.M. Alam, Abdullah M. Asiri, H.H. Hegazy, Mohammed M. Rahman. *J Mater Res Technol*, 9 **(2020)** (2), pp. 1457–1467.
(6) L. S. Huang, S. G. Yang, T. Li, B. X. Yu, Y. W. Du, Y. N. Lu, and S. Z. Shi. *J. Cryst. Growth*, 260**(2004)**, p. 130.
(7) B. Balamurugan, B. R. Mehta, D. K. Avasthi, F. Singh, A. K. Arora, M. Rajalakshmi, Y. Raghavan, A. K. Tyagi, and S. M. Shiva Prasad. *J. Appl. Phys*, 92**(2002)**, p. 3304.
(8) I. Lyubinetsky, S. Thevuhasan, D. E. Mc Cready, and D. R. Baer. *J. Appl. Phys*, 94**(2003)**, p. 7926.
(9) K. Kamimura, H. Sano, K. Abe, R. Hayashibe, T. Yamakami, M. Nakao, and Y. Onuma. *IEICE Trans. Electron,* E87-C **(2004)**, p. 193.
(10) A. A. Ogwu, E. Bouquerel, and F. Placido, *CERAC, Coat. Mater. News,* 13**(2003)**, p. 1.
(11) S. Ishizuka, T. Maruyama, and K. Akimoto. *Jpn. J. Appl. Phys,* 39**(2000)**, p. 786.
(12) Z. G. Yin, H. T. Zhang, D. M. Goodner, M. J. Bedzyk, R. P. H. Chang, Y. Sun, and J. B. Ketterson. *Appl. Phys. Lett,* 86**(2005)**, p. 61901.
(13) S. Ishizuka, S. Kato, Y. Okamoto, T. Sakurai, K. Akimoto, N. Fujiwara, and H. Kobayashi. *Appl. Surf. Sci.* 216 **(2003)**, p. 94.
(14) S. Ghosh, D. K. Avasthi, P. Shah, V. Ganesan, A. Gupta, D. Sarangi, R. Bhattacharya, and W. Assmann. *Vacuum*, 57**(2000)**, p. 377.
(15) M. Yang and J. J. Zhu. *J. Cryst. Growth*, 256**(2003)**, p. 134.
(16) S. C. Ray, *Sol. Energy Mater. Sol. Cells,* 68**(2001)**, p. 307.
(17) T. Mahalingam, J. S. P. Chitra, J. P. Chu, and P. J. Sebastian. *Mater. Lett*, *Sol. Cells* 58**(2004)**, p. 1802.
(18) V. Georgieva and M. Ristov. *Sol. Energy Mater,* 73**(2002)**, p. 67.
(19) Y. L. Liu, Y. C. Liu, R. Mu, H. Yang, C. L. Shao, J. Y. Zhang, Y. M. Lu, D. Z. Shen,

and X. W. Fan, Semiconductor. *Sci. Technol*, 20 **(2005)**, p. 44.

(20) R. Liu, E. W. Bohannan, J. A. Switzer, F. Oba, and F. Ernst. *Appl. Phys. Lett*, 83**(2003)**, p. 1944.

(21) L. N. Huang, H. T. Wang, Z. B. Wang, A. Mitra, D. Y. Zhoo, and Y. S. Yan. *Chem. Mater,* 14**(2002)**, p. 876.

(22) Anmar H. Shukor, Haider A. Alhattab, and Ichiro Takano, *Journal of Vacuum Science & Technology B,* 38**(2020)**, p. 012803.

(23) Jinyan Pan, Chengfu Yang and Yunlong Gao. *Sensors and Materials*, 28**(2016)**, pp. 7 817–824.

(24) M. F. Al-Kuhaili. *Vacuum*, 82**(2008)**, p. 623.

(25) A. V. Moholkar, S. M. Pawar, K. Y. Rajpure, C. H. Bhosale, and J. H. Kim. *Appl. Surf. Sci*, 255**(2009)**, p. 9358.

(26) Akhalakur Rahman Ansari, Ahmed H. Hammad, Mohamed Sh. Abdel-wahab Mohammad Shariq, Mohd. Imran. *Optical and Quantum Electronics*, 426**(2020)**, pp. 2-16.

(27) M. H. Suhail, G. Mohan Rao, and S. Mohan. *J. Appl. Phys*, 71**(1992)**, p. 1424.

(28) N.K.Das, J.Chakrabartty, S.F.U.Farhad A.K.Sen Gupta, E.M.K.Ikball Ahamed, K.S.Rahman, A.Wafi, A.Alkahtani, M.A.Matin, N.Amin. *Results in physics*, 17**(2020)**, p. 103132.

(29) S. Ishizuka, T. Maruyama, and K. Akimoto. *Jpn. J. Appl. Phys*, 39**(2000)**, p. 786.

Chapter 6 Structural and optical properties of copper oxides thin films fabricated on plastic substrates

6.1 Introduction

Copper oxides with CuO, Cu_2O or both phases are one of promising oxide semiconductors that are inspirited by many researchers due to its optimistic optical characteristics such as a narrow band gap (1.2-2.3eV) or high transparency, and additionally copper oxides are a non-toxicity and a low-cost material. These features make copper oxides a promising material which is used in numerous applications such as optical computers, optical memory, optical limiting devices, or optical switching elements(1,2). Moreover, copper oxides are using as sensors(3), electrochromic devices(4), and its distinctive features as absorber layer in hetero-junction thin-film solar cells(5). For the above purposes, various types of fabrication methods have been utilized to achieve high crystallinity on plastic substrates, such as plasma ion-assisted deposition (plasma-IAD)(6), thermal evaporation(7), activated reactive evaporation(8), molecular beam epitaxial growth(9), solution growth(10), the sol-gel process(11), electrodeposition(12) and RF magnetron sputtering. In this study the copper oxide thin films with various phases were fabricated at low temperatures by the reactive DC magnetron sputtering with the helicon plasma. Because the helicon wave provides electromagnetic power to the plasma in addition to the magnetron power, the helicon plasma can be maintained at a low gas pressure without contacting to the substrate as called long-throw sputtering. Therefore, this system can fabricate thin films with an independent substrate temperature without influence for a sputtering power. The fabrication process allowed an appropriate control for the crystalline structure by free substrate heating (i.e. low temperature) during film deposition. On the other hand, the characteristics of fabricated thin films are significantly affected by the fabrication parameters of an O_2 gas, an Ar gas flow rate or a sputtering power(13). In optical applications the transparency of a substrate plays a significant role in effectivity of optical devices(14), which can obtain a wider application field by using a high transparency substrate. In particular a glass of an inorganic material has high transparency and heat resistance, while organic materials with high transparency are limited and those materials show a low melting point. Despite this low melting point, significance to fabricate the thin film on an organic material is flexibility and lightness as its characteristics. In the thin film fabrication on organic materials there are some problems such as low crystallinity or poor adhesion between a thin film and an organic material due to limitation of a heating temperature(6). In this paper copper oxide thin films of Cu_2O, CuO or both phases have been fabricated on poly-methyl methacrylate (PMMA) and polycarbonate (PC) which are key materials with transparency in a transparent thermoplastic. PMMA, also known as acrylic, acrylic glass shows higher transparency than that of PC. PC in carbonate groups has higher shock-resistance, fire-resistance and heat-resistance than those of PMMA. They are used as parts for lighting fixtures in automobiles or home appliances because they are easy to be molded. Copper oxide thin films on PMMA and PC substrates were deposited by using the helicon plasma DC magnetron sputtering at temperatures ranging from an ambient room temperature to 100 °C without decomposing the structure of the PMMA and PC substrates.

6.2 EXPERIMENTAL AND MEASUREMENT METHODS

6.2.1 Experimental methods

Reactive DC magnetron sputtering with the helicon plasma was employed to prepare copper oxide thin films on PMMA and PC substrates. The substrate holder was located in 300 mm distance from the 99.9 % pure copper target of Φ 2 inches in a size. PMMA, PC and Glass (EAGLE XG: Corning Inc.) with a size of 9 × 15 mm of 1 mm in a thickness was set to the substrate holder. The substrate surface was cleaned by Ar plasma for 10 min before the film deposition. The film formation chamber of the multi-process coating apparatus (ULVAC Inc.) was exhausted to 6.0×10^{-6} Pa in a pressure by using a turbo molecular pump and a rotary pump. As shown in Table 6.1, copper oxide thin films were fabricated under an ambient room temperature without heating and under heating of 45 °C set in an infrared lamp controller. The deposition temperature (actual temperature) of each substrate was measured by non-reversible temperature labels attached to the substrate, because the ambient temperature of the substrate slightly elevated due to thermal radiation from the target depended on the DC sputtering power 10 W and 30 W, with the common RF helicon plasma power of 50 W. An O_2 and Ar gas flow rate were kept at 10 and 15 sccm respectively. Science the deposition rate depended on the sputtering power was measured by using a quartz-type thickness tester in the film formation chamber, the formation time to obtain 200 nm in a film thickness was calculated about the DC sputtering power 10 W and 30 W. The required deposition time was 208 min and 73 min at 10 W and 30 W respectively. The reason of choosing the 10 W and 30 W in a DC sputtering power had been described in our previous study that

Table 6.1 Details of formation conditions

Condition name	(A)	(B)	(C)	(D)
Substrate	PMMA, PC, Glass (EAGLE XG)			
Temperature set in an infrared lamp controller (ºC)	Non-controlled (Room temperature)	45	Non-controlled (Room temperature)	45
Deposition temperature (DT) measured by a non-reversible temperature label (ºC)	38	90	48	100
RF helicon plasm power (W)	50			
DC sputtering power (W)	10		30	
Cu sputtering rate (nm/sec)	0.015		0.046	
O_2 and Ar gas flow rate (sccm)	10 and 15			
Film thickness (nm)	200			

shows the formation of CuO, Cu_2O and both phases in different Cu sputtering rates(2). In this paper the sample of the condition (A) and (B) were 10 W in DC sputtering power and the samples of the condition (C) and (D) were 30 W in each formation condition.

6.2.2 Characterization methods

6.2.2.1 Crystal structure measurement

The crystal structure of the thin film was measured by thin film X-ray diffraction (XRD: High quality XG M18XCE, MAC Science. Co., Ltd.) using CuKα rays (0.154056 nm) at an incident angle of 0.3 degrees.

6.2.2.2 Surface laser micrographs measurement

Laser scanning microscope (OLS4500, Olympus Corp.) was employed to observe the surface morphology and surface scratch evaluation.

6.2.2.3 Adhesion evaluation

In this study, the adhesion of the thin film was evaluated using a scratch tester (3K-34B, SHINTO scientific Co., Ltd.). The scratch test was performed with a diamond indenter of 20 µm in a radius of curvature, the scratch speed of 1.0 mm/s and a vertical load of 0-4.9 N with increasing a load continuously, through the scratch length of 10 mm. The scratched surface was observed at a load of 2.45 N by the laser microscope. After scratch the surface have investigate by laser scanning microscope to determine the adhesion between the surface and the film.

6.2.2.4 Photoconductivity

As the sample for measuring the photoconductivity, a sample with a size (10 × 8) mm and a film thickness of 200 nm with electrodes formed with silver paste was used. A DC voltage of 1.0 V was applied in the longitudinal direction of this sample, an artificial solar illuminator containing ultraviolet rays from a wavelength of 290 nm was used, and the current change during irradiation was measured with a non-resistive ammeter to calculate the conductivity.

6.2.2.5 Optical properties calculation

UV-Vis spectrophotometer (UV-2550, Shimadzu Corp.) device have used to determine the optical band gap and optical transmittance. The bandgap have calculated in wavelength from 300 nm to 900 nm. Because of the crystallinity and higher transparency, the copper oxide films are suitable for optical analysis from which the absorption coefficient and energy band gap may be determined. The conversion of Cu_2O into CuO can also be shown by the determination of the optical band gap. The best linear relationship is obtained by plotting α^2 against hν, based on Eq (6.1) below.

$$\alpha h\nu = A\,(h\nu - E_g)^{n/2} \qquad \ldots\ldots\ldots\ (6.1)$$

where α is absorption coefficient, A a constant (independent from ν) and n the exponent that depends upon the quantum selection rules for the particular material. The photon energy (hν) for y-axis can be calculated using Eq (6.2).

$$E = h\nu = hc/\lambda \qquad \ldots\ldots\ldots\ (6.2)$$

where h is Plank’s constant ($6.626x10^{-34}$), c is speed of light ($3x10^{8}$) and λ is the wavelength. The transmittance has determined under wavelenght from 400 nm to 800 nm.

6.2.2.6 Electrical properties calculation

A two-point resistance measurement is the simplest method to assess the conductivity of a sample. A test current is forced through the sample and the multimeter measures the voltage drop between the two terminals. The problem of this method is that the resistance of the wires and the contact resistance at the terminals are included in this measurement. Therefore, to assess the resistance and obtain accuracy values of a resistivity, mobility and carrier concentration of thin film, it is preferable to rely on a four-point resistance measurement as in a Hall Effect measurement system (Ecopia Co. Ltd) as explained below. The resistivity of a thin film can be performed by means of four collinear contact points. At first, a known DC current I is applied between the two outer probes. Then, the voltage V between the two inner probes is measured. Finally, the resistivity is calculated from

$$\rho = F\ V/\ I \ \ldots\ldots\ldots\ldots\ (6.3)$$

where F [m] is a geometric correction factor depending on the geometric arrangement of the probes, the thickness of the sample, the finite size of the sample, and the position of the probes with respect to the sample edge(15). The main advantage of a four-point resistance measurement is the elimination of contact resistances at the positions of the probes, considering that voltage probes have a high electrical impedance.

6.3 FILM CHARACTERIZATION AND DISCUSION

6.3.1 Film structure

Figure 6.1 shows the XRD patterns of the copper oxide films formed by the DC sputtering power of 10W on the PMMA, PC and Glass substrate at two temperatures of the condition (A) and (B) of an infrared lamp controller, respectively. The crystal structure of copper oxide films on different substrates showed a mixed crystal consisting of weak CuO (110), (-111), (111) peaks and Cu_2O (111), (200), (220) peaks as shown fig 6.1 (A). The difference in crystallinity for each substrate was highest for PMMA, followed by Glass and PC. At this temperature, it is assumed that difference of the crystallinity was caused by the structure of the substrate itself without the relationship of the thermal resistance temperature of the substrate.

In the condition (B) of fig 6.1, the Cu_2O peaks disappeared and strong CuO (-111), (111) peaks were observed for all types of substrates, because on the both samples of the condition (A) and (B), according to deposition temperatures measured using a non-reversible temperature label, the temperature of the condition (B) was about 90 ^oC higher than that of the sample (A) due to raising the temperature by an infrared lamp to 45 ^oC. It was confirmed that the crystallinity of the copper oxide thin film was improved at moderate substrate temperatures, even on plastic substrates.

Figure 6.2 shows the XRD patterns of the copper oxide films formed by the DC sputtering power of 30W on the PMMA, PC and Glass substrate at two temperatures of room temperature (C) and 45 ^oC (D) of an infrared lamp controller, respectively. At room temperature (C), the single phase Cu_2O with the strong peak of (111) was shown on each substrate and as in fig 6.1 (A), the PMMA substrate had the highest crystallinity. Furthermore, as shown in fig 6.2 (D), the Cu_2O (200) peak on the plastic substrates increased by increasing the temperature of an infrared lamp controller to 45 ^oC, however, the oxide films on Glass substrate had no change.

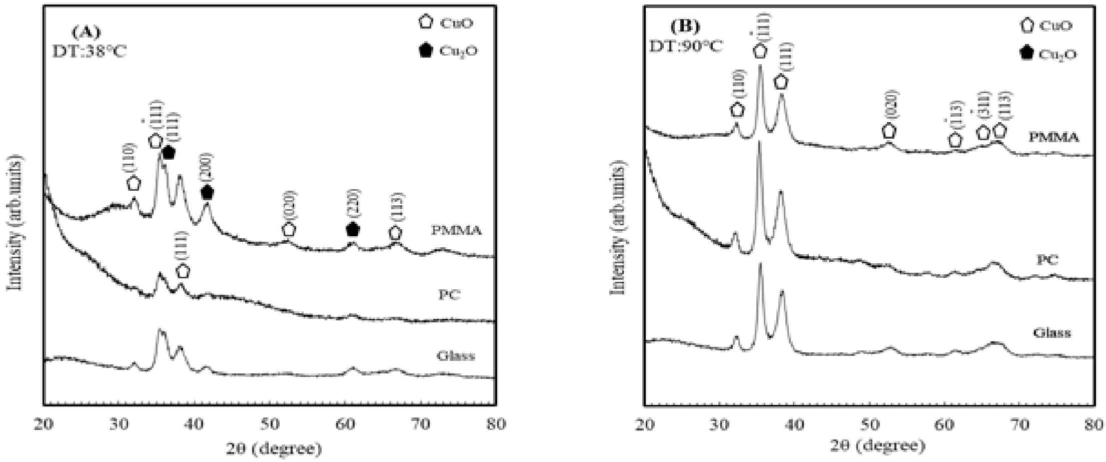

Figure 6.1 XRD characterization of samples (A) and (B) that formed at 10Won PMMA, PC and Glass substrates

The samples of the condition (A) and (B) in Table 6.1 obtained the CuO structure in the film crystallinity, because the samples of (A) and (B) were fabricated by the lower sputtering rate in a DC power of 10 W than that of the samples of (C) and (D). Generally, in the reactive sputtering method, the oxidation is enhanced by a low Cu sputtering rate due to easy to bond with oxygen molecules and the crystallinity is improved by increasing heating temperature(16).

From XRD measurements, it was confirmed that each fabrication of CuO or Cu_2O thin films on the plastic substrates could be performed by the helicon plasma DC magnetron sputtering with a low heating temperature.

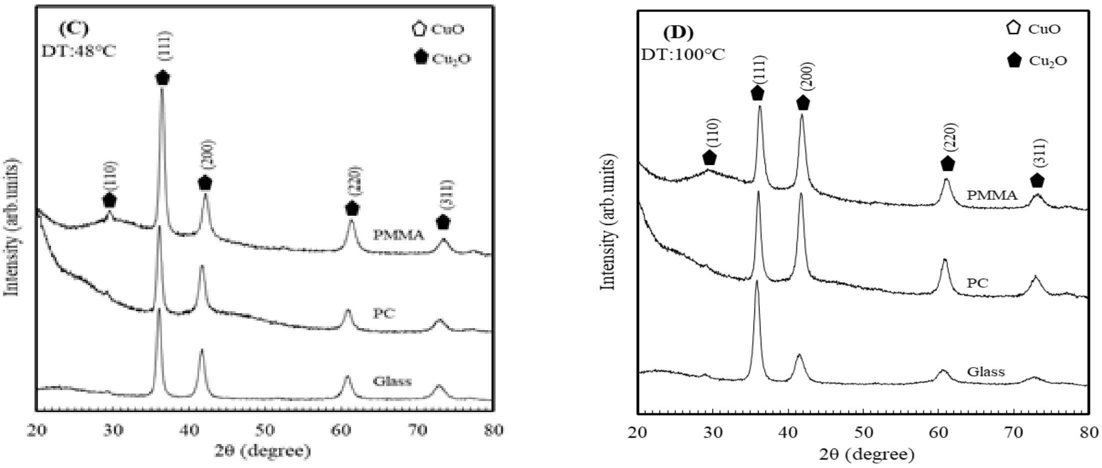

Figure 6.2 XRD characterization of samples (C) and (D) that formed at 30Won PMMA, PC and Glass substrates

6.3.2 Surface laser micrographs

Figure 6.3 (A), (B), (C) and (D) show surface laser micrographs of copper oxide films formed by the DC sputtering power of 10 W and 30 W at two temperatures of room temperature and 45 °C of an infrared lamp controller. The both thin films fabricated on PC and Glass substrates had smooth surfaces and no noticeable cracks, indicating that they were homogeneous films with good interfacial bonding between the substrate and the thin film, while for the thin films fabricated on PMMA substrates, cracks were observed on each surface from the condition (A) to (D). The different surfaces of PMMA and PC were suggested due to the difference in the heat distortion temperature, which was thought to be responsible for the cracking. Incidentally, the heat distortion temperatures of PMMA and PC are 68 - 99 °C and 121 - 132 °C, respectively, with PMMA being lower. The surface cracks on the PMMA substrate were hardly observed in the condition (A) 38 °C and (C) 48 °C measured by the non-reversible temperature label as shown in Table 6.1, because of the deposition temperatures under the heat distortion temperature of PMMA, while the surface cracks of the condition (B) 90 °C and (D) 100 °C increased with increasing the deposition temperature which was over the heat distortion temperature.

The smooth and homogeneous CuO or Cu_2O thin films could be fabricated on PC substrates by the helicon plasma DC magnetron sputtering method, however, in the case of the PMMA substrate, the lower temperature was required.

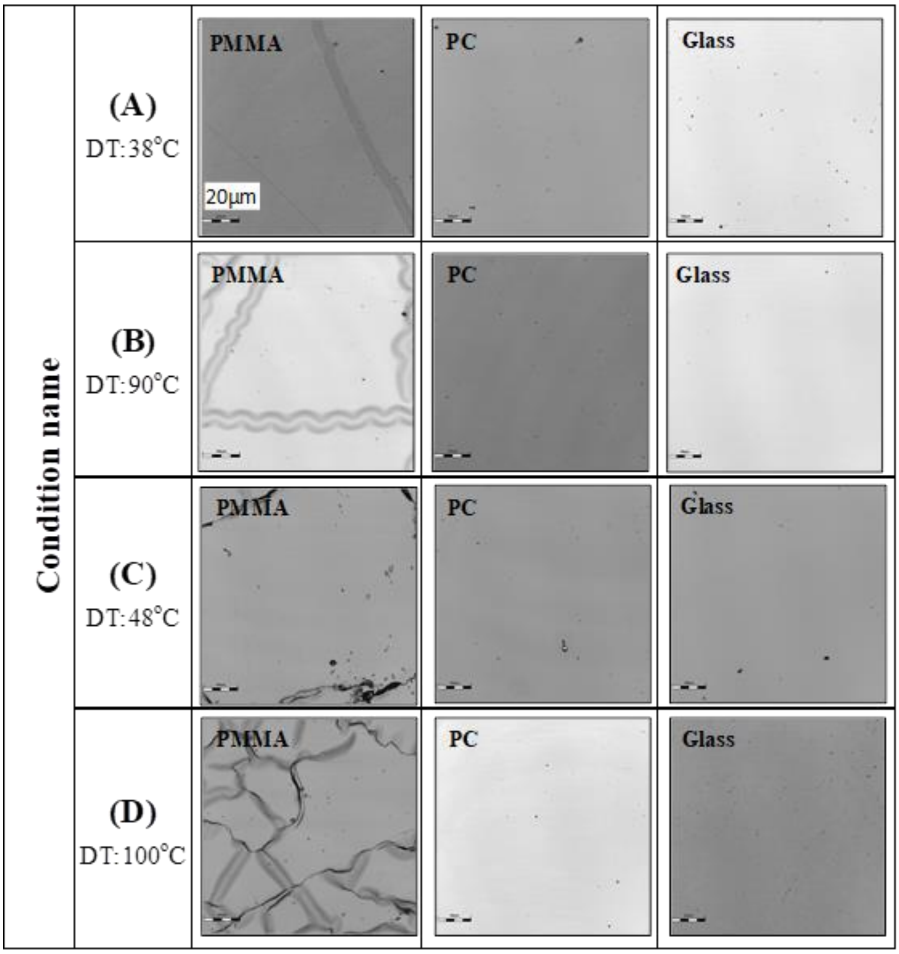

Figure 6.3 (A), (B), (C) and (D) show surface laser micrographs of copper oxide films that formed with 10W and 30W at two temperatures of room temperature and 45℃ of an infrared lamp controller.

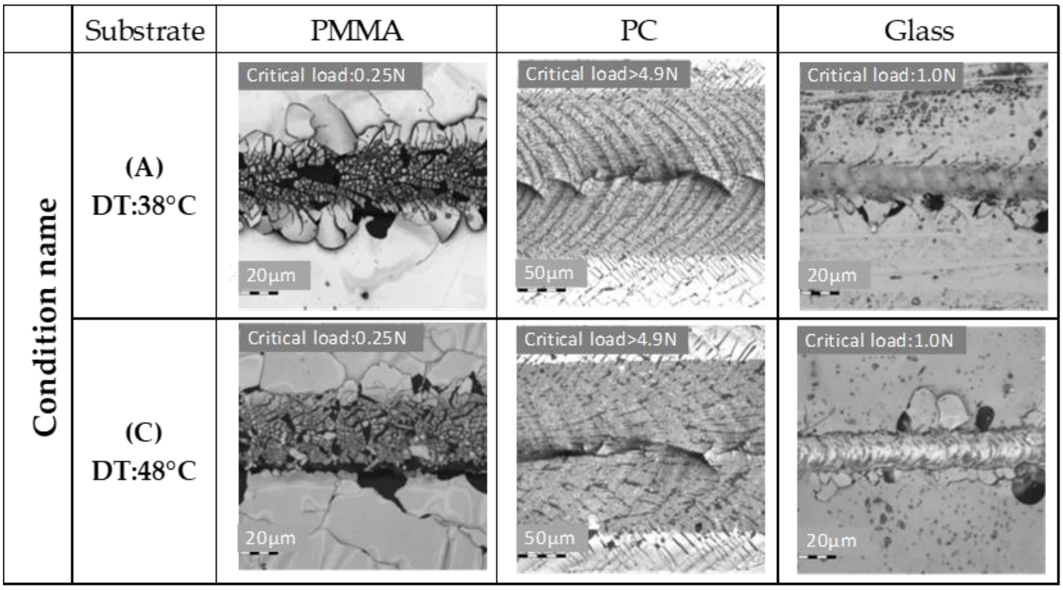

Figure 6.4 (A,C) Surfasce photographs of the scratched copper oxide films on the substraes fabricated at room temperatures, 45℃ with 10 W and 30 W

To confirm adhesiveness between the plastic substrates and copper oxide films fabricated at the room temperatures (Condition A and C), the scratch test was performed with a diamond indenter of 100 µm in a radius of curvature, the scratch speed of 1.0 mm/s and a vertical load of 0-4.9 N with increasing a load continuously, through the scratch length of 10 mm. Figure 4 shows the surface photographs of scratch scars on CuO (A) and Cu_2O (C) thin films. The indenter scratched the samples in a straight line from left to right in the photographs. The difference in the width of the scratch scars came from the difference in the original hardness of each substrate. The critical load observed from the scars via the scratch test was shown in the upper part of the photographs. No difference appeared due to the type of copper oxide thin films on each substrate. For the PMMA substrates, the delamination generated immediately after the start of scratching, and the critical load was around 0.25 N. On the other hand, the adhesion between the PC substrates and the copper oxide thin films was so strong that no clear peeling occurred even at the maximum load of 4.9 N, although small cracks were observed. The magnification of these PC photographs was reduced to observe the scratched scars. In the case of glass substrates, the critical load at which the delamination generated on the side of the scratch scars was 1.0 N. Above this value, the glass substrate was severely damaged by scratching. Via the scratch test, it was thought that the improvement of adhesion was necessary for PMMA substrates, however, for PC substrates, the sufficient adhesion was confirmed.

6.3.3 Optical transmittance

The optical transmittance of thin films fabricated on PMMA, PC and glass substrates at a room temperature and 45°C under 10 W sputtering power were shown in fig 6.5 (A) and (B) respectively. With the measurement wavelength increased from 450 nm to 800 nm, the optical transmittance of all the substrates increased as showing the typical behavior of CuO. These films were CuO with some Cu_2O in the condition (A) and the CuO thin film in the condition (B) from XRD measurements of fig 6.1. In the fabrication condition (A), the transmittance decreased in the order of PMMA, PC, and glass substrates, which was consistent with the crystallinity (fig 6.1 (A)) measured by the XRD. In the preparation condition (B), the transmittance of all the samples decreased due to the change of the crystal structure from a light black mixed phase (Cu_2O and CuO) in the condition (A) to a dark black single phase CuO in the condition (B). Figure 6.6 (C) and (D) showed the typically optical transmittance of Cu_2O thin films fabricated at a room temperature and 45 °C under 30 W input power. The both Cu_2O thin films of (C) and (D) with high crystallinity showed similar behavior, however the transmittance of PMMA with many cracks was slightly lower in the condition (D). From the optical transmittance measurements, it was found that CuO and Cu_2O thin films can be fabricated on PMMA and PC substrates with almost the same optical properties as those on glass substrates.

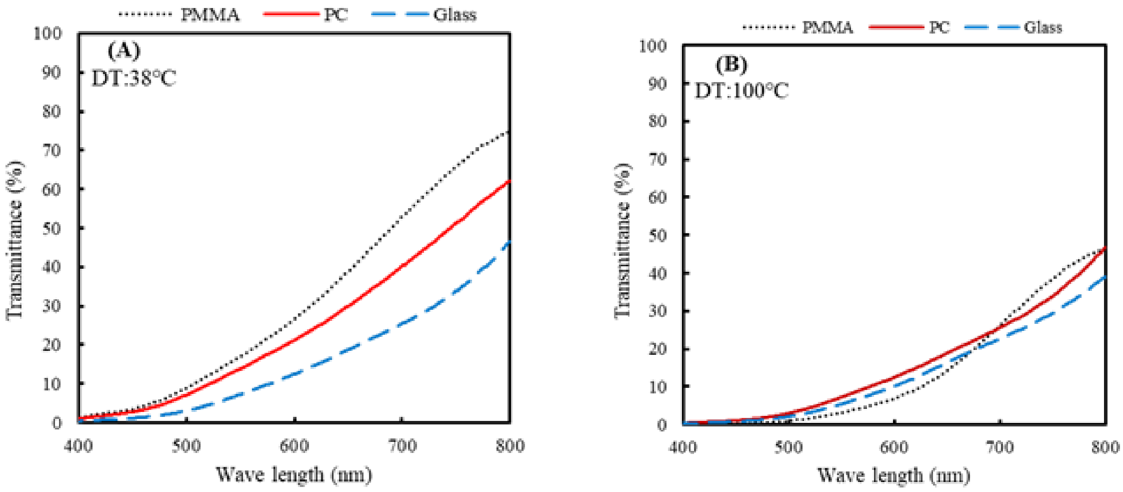

Figure 6.5 Transsmitance of (A) and (B) that formed at 10Won PMMA, PC and Glass substrates

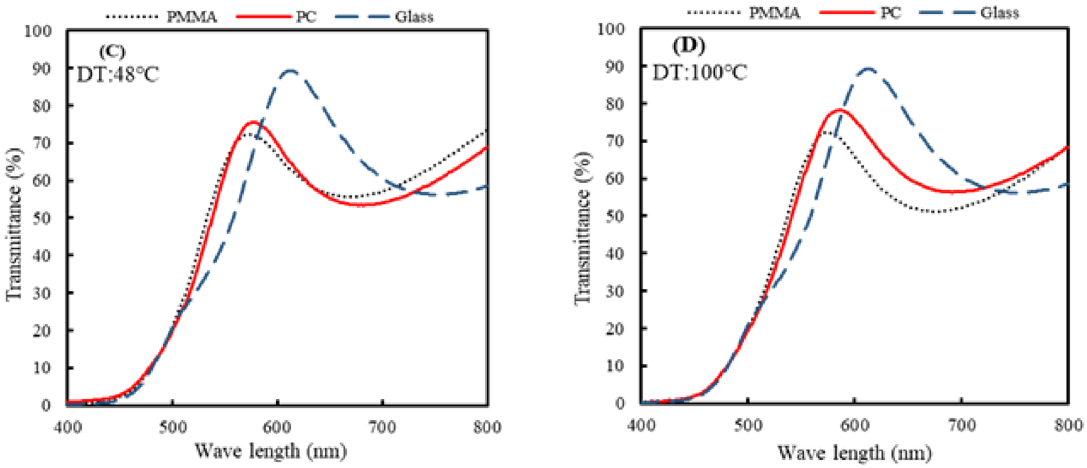

Figure 6.6 Transsmitance of (C) and (D) that formed at 30Won PMMA, PC and Glass substrates

6.3.4 Optical bandgap

To investigate semiconductor properties of copper oxide thin films, the optical band gap energy was determined using optical absorption spectra. The origin of indirect bandgap in CuO is the energy gap between the conduction and valence bands formed by 3d orbitals of copper, whereas, the direct transitions can occur in Cu_2O between oxygen 2p states, constituting valence band and the conduction band formed by copper 3d states$^{(17)}$.

The optical bandgap energy was leaded by the plotted curve using Tauc's equation $(\alpha h\nu)=A(h\nu-Eg)^n$. The indirect bandgap energy was estimated by plotting $(\alpha h\nu)^{1/2}$ versus the photon energy hν, while the direct bandgap energy was obtained by plotting $(\alpha h\nu)^2$ versus hν and extrapolating the straight-line part of the plot. CuO is generally reported as a copper oxide with an indirect bandgap energy. However, in this study CuO was calculated by plotting $(\alpha h\nu)^2$ as reported in almost papers, because it is difficult to separate the photon energy and the phonon energy of CuO from plotting $(\alpha h\nu)^{1/2}$.

Figure 6.7 shows the CuO bandgap energy of samples fabricated by the condition (A) and (B) on PMMA, PC and Glass substrates respectively. The single phase of CuO fabricated by the condition (B) of 45 °C showed a bandgap energy of 1.75 eV on a Glass substrate and 1.8 eV on a PC and a PMMA substrate, while the mixture phase fabricated at a room temperature showed increase in a bandgap energy to 1.8 - 1.95 eV as shown in fig 6.7 (A) due to containing of slight Cu_2O in CuO. In the case of Cu_2O in fig 6.8 (C) and (D), the Cu_2O thin films on all substrates obtained a bandgap energy of 2.1 eV because of high crystallinity as showen in fig 6.2 (C) and (D). These results were in good agreement with XRD measurements of figure 6.1 and 6.2. Copper oxide films with the semiconducting property could be controllably fabricated on the plastic substrates.

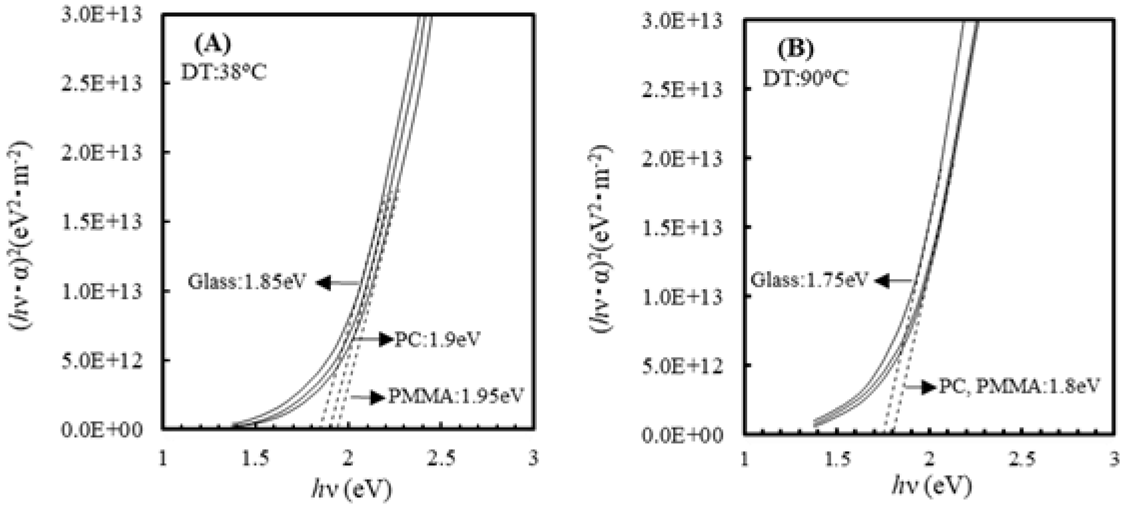

Figure 6.7 Band gap of samples (A) and (B) that formed at 10W on PMMA, PC and Glass substrate

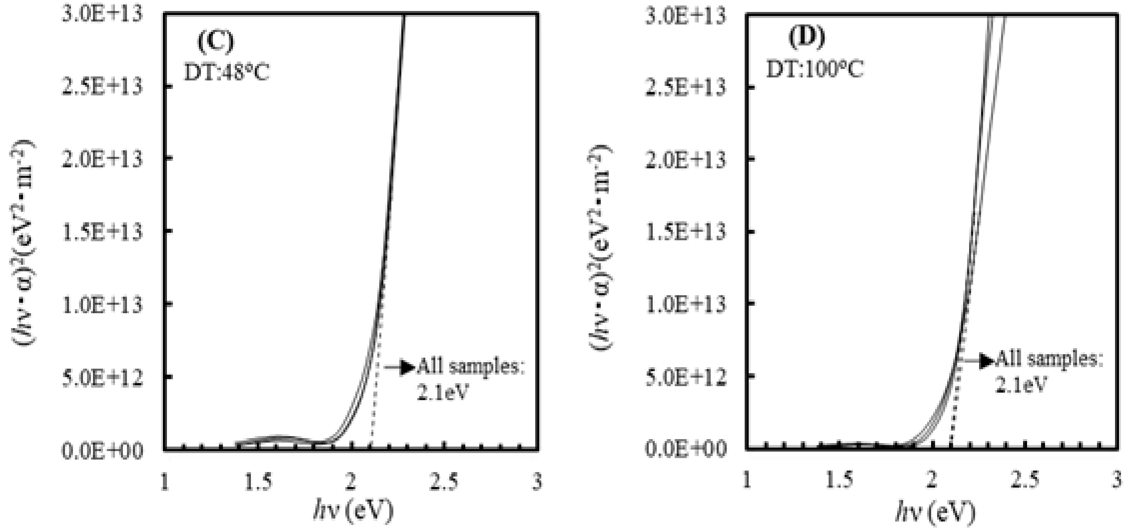

Figure 6.8 Band gap of samples (C) and (D) that formed at 10W on PMMA, PC and Glass substrate

6.3.5 Electrical properties

Figure 6.9 shows the the resistivity and mobility for CuO films of samples fabricated by the condition (A) and (B) on PMMA, PC and Glass substrates respectively. The resistivity for the film fabricated at room temperature shows low resistivity on PMMA and glass substrats, and high resistivity on PC substrate. The reason for the low resistivity at PMMA and Glass is attributed to the high crystal structure, and the weak crystal structure at PC led to obtain a high resistevity, this results was confirmd by figure 6.1(A). At high temperature 45℃, the resistivity of all substrats showen slightly increasing due to the transition the film from mixture phase to single phase of CuO(18) , this result also cofirmed by XRD results of fig 6.1(B). The low resistevity at PC substrste due to the high crystal structure. The higher carriers concentration were 4.0×10^{-14} cm^{-3} at 45℃ on PMMA substrate, and the lower value of 9.3×10^{-16} cm^{-3} at 45℃ on PC substrate.

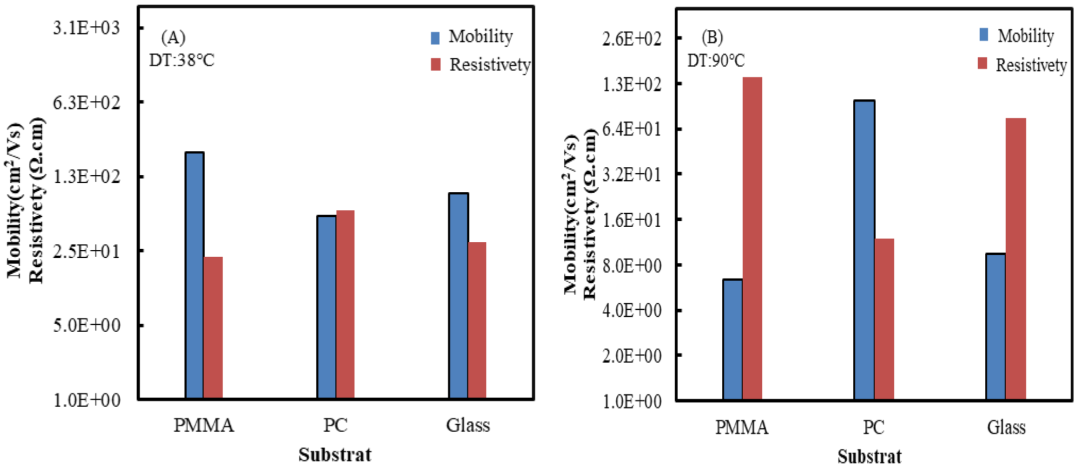

Figure 6.9 Electrical properties of samples (A) and (B) that formed at10Won PMMA, PC and Glass substrates

Figure 6.10 shows the the resistivity and mobility for Cu_2O of samples fabricated by the condition (C) and (D) on PMMA, PC and Glass substrates respectively. The lower resistivity was at room temperatur on PMMA substrate due to the high crystalline at this temperature. The higher resistivity was on PMMA at high temperature substrate due to excess cracks in the fabricated films(19) as shown in figure 6.3 (D). The valus of mobility and carriers concentration were from 9.5 cm^2/Vs to $9.6 \times 10^2 cm^2/Vs$, and from 1.3×10^{14} cm^{-3} to 6.2×10^{16} cm^{-3} respectivily.

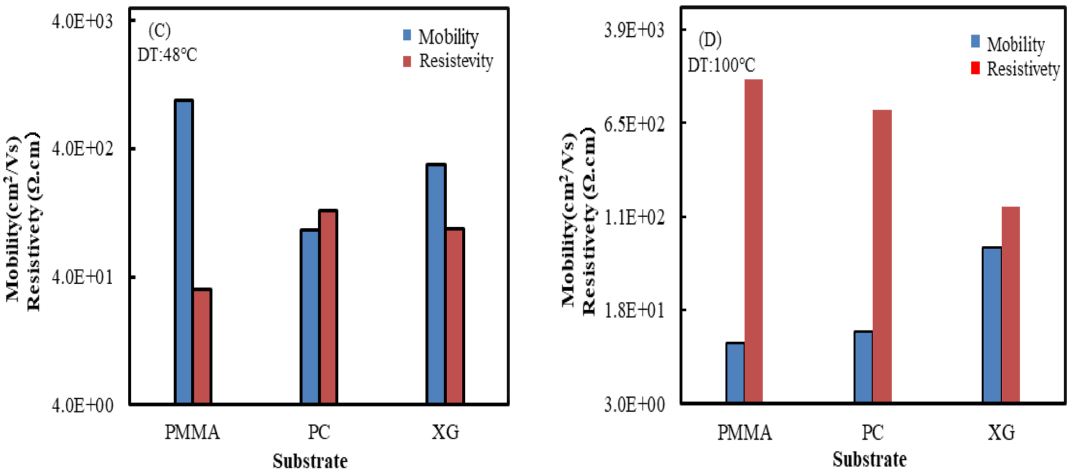

Figure 6.10 Electrical properties of samples (C) and (D) that formed at 30Won PMMA, PC and Glass substrates

6.4 CONCLUSIONS

Copper oxides of CuO and Cu_2O phases have been fabricated on the plastic substrates by using the helicon plasma DC magnetron sputtering method under various conditions. In the film fabrication the important parameters were DC input powers and the deposition temperatures including radiation temperature due to those DC input powers. In particular the deposition temperature of substrates was able to keep low by the long-throw sputtering using the helicon plasma without affecting the plastic substrates. The PMMA, PC and Glass substrates with high transparency were used to investigate the structural, surface and optical properties. As the results, the CuO and Cu_2O thin films could be successfully formed with high crystallinity under low temperatures on plastics substrates as well as on Glass substrates. The thin films on a PC and a Glass substrate had the homogenous and smooth surface without any cracks as observed from laser micrographs, while cracks of the thin films on a PMMA substrate increased with increase of a deposition temperature because of a low heat distortion temperature. The optical transmittance of the CuO and Cu_2O thin films showed obvious difference. The optical transmittance of the thin films fabricated at the lowest deposition temperature depended on the crystallinity of the CuO and Cu_2O mixture, while the thin films with high crystallinity was independent from the substrate types. Also the optical bandgap energies were influenced by the crystallinity of CuO and Cu_2O and the bandgap energy value was nearly equal with other reference papers. The electrical properties results showed low resistivity at the films fabricated on the plastic substrates at low temperature, and it is approach to the resistivity that obtained on glass substrate.This study showed novel results to form CuO and Cu_2O thin films on transparent plastic substrates under a low deposition temperature. These thin films can be used in various optical applications to need high transparency or flexibility of a substrate.

REFFRENCES

(1) Chih-hao Yang, Shih-chin Lee, Tien-chai Lin, Suz-cheng Chen. *Thin Solid Films*, 516 **(2008)**, pp. 1984–1991.

(2) Anmar H. Shukor, Haider A. Alhattab, and Ichiro Takano. *Journal of Vacuum Science & Technology B*, 38 **(2020)**, p. 012803.

(3) S. Anandan, X. Wen, Mater. *Chem. Phys,* 93 **(2005)**, pp. 35-40.

(4) Ran Li, Xiaoyuan Ma, Jianmin Li, Jun Cao, Hongze Gao, Tianshu Li, Xiaoyu Zhang, Lichao Wang, Qinghong Zhang, Gang Wang, Chengyi Hou, Yaogang Li, Tomás Palacios, Yuxuan. *Natural Communication*, 12**(2021)**, p. 1587

(5) López R., Gómez R., Llanos M.E. Catal. *Today*, 148 (2009), pp. 103–108.

(6) Ulrike Schulz, Norbert Kaiser. *Progress in Surface Science,* 81 **(2006)**, pp. 387–401.

(7) M. Kaur, K.P. Muthe, S.K. Despande, S. Choudhury, J.B. Singh, N. Verma, S.K. Gupta, J.V. Yakhmi. *Ryst. Growth*, 289 **(2006)**, pp. 670-675.

(8) M.F. Al-Kuhaili. *Cuum*, 82 **(2008)**, pp. 623-629.

(9) I. L. Yubinetsky, S. Thevulhasan, D. E. Mc Cready, and D. R. Baer. *J. Appl. Phys*, 94 **(2003)**, p. 7926.

(10) C. A. N. Fernando and S. K. Wetthasinghe. *Sol. Energy Mater. Sol. Cells*, 63**(2000)**, p. 299.

(11) J. Livage; C. Sanchez; M. Henry; S. Doeuff, *The chemistry of the sol-gel process. Solid State Ionics,* 13**(1989)**, pp. 32-33, pp. 633-638.

(12) S.W. Choi, J.Y. Park, S.S. Kim, Chem. *Eng. J.*, 172 **(2011)**, pp. 550-556.

(13) H. A. Shukur, M. Sato, I. Nakamura, and I. Takano. *Advances in Materials Science and Engineering,* 24**(2012)**, p. (2012).

(14) Pallabi Paul, Kristin Pfeiffer, and Adriana Szeghalmi, *Coatings*, 10 **(2020)**, p. 64.

(15) I. Miccoli, F. Edler, H. Pfnür, and C. Tegenkamp. *Journal of Physics: Condensed Matter*, 27 **(2015)**, p. 22.

(16) Kasim Uthman Isah, Muhammad Bakeko M., Umar Ahmadu, Uno Essang Uno, Mohammed Isah Kimpa, Jibrin Alhaji Yabagi. *(IOSR-JAP)*, 26**(2013)**, pp. 61-66.

(17) Y. Wang, S. Lany,2 J. Ghanbaja, Y. Fagot-Revurat, Y. P. Chen, F. Soldera,4 D. Horwat, F. Mucklich and J. F. Pierson1. *PHYSICAL REVIEW B*, 94**(2016)**, p. 245418.

(18) V.F.Drobny, L.Pulfrey. *Thin Solid Film*, 61**(1979),** pp. 89-98.

(19) Cheng-Wei Kang, Han Huang. *Adv. Manuf*, 5 **(2017)**, pp. 1–19.

Chapter7 Summary

The purpose of this study was to control the structure of copper oxide thin films by reactive DC magnetron sputtering using helicon plasma. It is known that this method using helicon plasma enables low temperature deposition, and considered as a most efficiently used to fabricate multilayers because of its high stability in deposition rate. On the other hand, the copper oxide thin film has been studied for a long time, however recently it has been recognized as a new material due to its application in the solar cells. By this method, CuO and Cu_2O of the copper oxide thin films were arbitrarily fabricated by controlling the DC input power of sputtering and the substrate temperature. The fabricated copper oxide thin films showed high crystallinity and stable electrical properties.

Where, in the chapter 4, copper oxide thin films prepared by reactive DC magnetron sputtering with helicon plasma were investigated under various sputtering powers. Single-phase n-type CuO and single-phase p-type Cu_2O were obtained at 10 W and 30 W in a sputtering power, respectively. High crystallinity could be obtained for these films by changing only one fabrication condition of the sputtering power. XRD and XPS results confirmed that sputtering power is the main factor determining the structure of the copper oxide films. From the Hall effect measurements and the calculated optical band gap, copper oxide thin films with precise semiconducting properties could be fabricated.

In chapter 5, Cu_2O and CuO thin films were fabricated on glass substrate at various substrate temperatures ranging from room temperature to 300°C. At an input power of 10 W, the crystalline structure of the CuO thin film decreased with decreasing a substrate temperature and showed a mixed structure of CuO/Cu_2O at room temperature. The transmittance increases with decreasing the temperature, because the Cu_2O has higher permeability. In the case of the input power of 30 W, all the samples were Cu_2O, while the transmittance decreased with decreasing the temperature. At the optical band gap of 30 W input power, their values were dichotomized by the temperature. When the temperature was lower than 45°C, the band gap was 2.1 eV, and the XRD measurement suggested the influence of the Cu_2O (200) surface. It was found that the present method can be used to fabricate CuO and Cu_2O thin films at low substrate temperature with high crystalline copper oxide thin films with satisfactory optical and electrical properties.

In chapter 6, after confirming the thin film formation at low temperature on glass substrate, the copper oxide thin films were deposited on PMMA and PC, which are transparent substrates with low melting point, and the copper oxide thin films with high crystallinity and optical properties as well as sufficient adhesion to the substrate were fabricated. This work demonstrates a new technique for the deposition of CuO and Cu_2O thin films on transparent plastic substrates at low deposition temperatures. These thin films can be used for a variety of optical applications requiring high transparency and flexibility.

Acknowledgements

First and foremost, I am extremely grateful to my supervisor, Prof. Ichiro Takano, for his invaluable advice, continuous support, and patience throughout my doctoral studies. I would also like to thank Prof. Norio Baba of the Faculty of Informatics, Kogakuin University, Prof. Eisaku Oho of the Faculty of Engineering, Kogakuin University, and Prof. Atsushi Yumoto of the Faculty of Engineering, Shibaura Institute of Technology, for their useful comments.

I would like to thank Dr. Haider Ali, department of electrical and electronic, Kofa university for providing me with supporting and advice throughout my study period. I would like to thank all the students in my laboratory. Their kind help and support has made my study and life in Japan wonderful.

I would also like to express my gratitude to my wife, her standing beside me gave me more power to complete my study.

Finally, I am deeply grateful to Ministry of Education, Culture, Sports, Science and Technology (JAPAN) and Ministry of Higher Education and Scientific Research, Wasit university (IRAQ) to the financial support during my study period.